

Master Thesis

Optical pulse shaping for trapped-ion quantum computing with integrated photonics

Stefanie Miller

Supervisors: Dr. Karan K. Mehta
Chi Zhang

Principal Investigator: Prof. Dr. Jonathan Home

Trapped Ion Quantum Information Group
Institute for Quantum Electronics
Swiss Federal Institute of Technology Zurich

Zurich, May 2019

Abstract

Segregated ion traps, that allow for independent computations in different regions, are a promising platform for scalable quantum computation. Integrating optics into the chip design improves scalability in a complimentary way, as it allows stable beam delivery to the ions as well as single-ion addressing. Any quantum algorithm requires a set of universal gates, including an entangling gate. This thesis investigates the individual steps towards the implementation of an entangling gate with integrated optics in a segregated trap. Based on the theory of a Mølmer-Sørenson entangling gate, the optimal pulse shape to entangle any pair of ions in a linear five ion chain is computed. Gate times between 40 μ s and 100 μ s are considered. A theoretical infidelity of $\leq 10^{-4}$ is achieved for gate times $\geq 60 \mu$ s. The necessary pulse shaping can be obtained with an acousto-optic modulator (AOM) that adjusts phase, amplitude and frequency of the laser beam. As a potential candidate, a fiber-coupled AOM is examined. The SiN photonics integrated on the chips, which direct the shaped laser beam towards the trapped ions, are characterized. The waveguide losses are found to be ~ 2 dB/cm. After polishing the edges of the chip, we have reduced the fiber-coupling loss to 2.8 dB.

Acknowledgements

First of all, I would like to thank Prof. Dr. Jonathan Home for the opportunity to conduct my master thesis within his group, allowing me to explore the scenes behind quantum computing with trapped ions.

I want to thank Dr. Karan K. Mehta for allowing me to be part of the integrated optics project. Thank you for your valuable input in various discussions and your guidance especially throughout the waveguide chip characterization.

Equally, I want to thank Chi Zhang for his guidance and help throughout the whole project. He always had time to spare whenever I was stuck and shared his useful knowledge during the many discussions we had. Thank you for being so patient with me.

All group members have been helpful by showing and/or lending me their tools. I am grateful for the many fruitful discussions and for the friendly atmosphere within the group. In particular, I would like to thank Christoph Fischer for his contributions to interface with the powermeter, Christa Flühmann for her calculation tricks and sharing her knowledge of phasespace diagrams, Maciej Malinowski for his help in the lab and Tobias Sägesser for proof-reading my thesis and providing helpful comments.

I kindly thank the QSIT Network for granting me the QSIT Master Internship Award.

Contents

1. Introduction	1
2. Quantum computation with trapped ions	3
2.1. An trapped-ion qubit in a harmonic potential	3
2.2. Interaction of an ion with light	4
3. Entanglement of two ions in a linear ion chain	6
3.1. Normal modes of coupled trapped-ion oscillators	6
3.1.1. Axial normal modes	6
3.1.2. Radial normal modes	7
3.2. Derivation of propagation operator	8
3.2.1. One ion and one bichromatic laser	8
3.2.2. Linear chain of N ions and two bichromatic lasers	11
3.3. Gate fidelity	15
3.3.1. Expected theoretical fidelity	15
3.3.2. Effect of the phase difference of the laser beams	17
3.3.3. Fidelity loss due to off-resonant carrier excitation	19
4. Simulation of two-ion entanglement in a linear five-ion chain	22
4.1. The underlying optimization problem	22
4.2. Numerical considerations	24
4.3. Results	25
4.3.1. Individual optimal pulse shapes for a gate time of $\tau_g = 100 \mu\text{s}$	26
4.3.2. Individual optimal pulse shapes for faster gates	30
5. Fiber-coupled AOM characterization	35
5.1. Working principle of an AOM	35
5.2. Fiber-coupled AOM	36
5.3. Measurement setup	36
5.4. AOM-device efficiency	38
5.4.1. Efficiency characterization	38
5.4.2. Approaches and considerations to improve efficiency	41
5.5. Pulse shaping effects	42
5.5.1. Delay of optical signal with respect to TTL signal	42
5.5.2. Rise and fall time	43
5.5.3. Optical power fluctuations and drifts	44
5.5.4. Influence of power fluctuations and pulse length on gate fidelity	46
6. Characterization of SiN photonics within an ion trap	47
6.1. Theory on waveguides	47
6.2. Measurement setup and investigated samples	48

6.3. Characterization of waveguide losses	49
6.3.1. Measurement of optical power transmission for different waveguide lengths	51
6.3.2. Waveguide losses determined by resonator resonances	51
6.3.3. Methods to improve fiber to waveguide coupling	57
7. Conclusion and outlook	60
A. Optimal pulse shape and phasespace diagrams	61
A.1. Solutions for a gate time of $\tau_g = 100 \mu\text{s}$	61
A.2. Solutions for a gate time of $\tau_g = 80 \mu\text{s}$	67
A.3. Solutions for a gate time of $\tau_g = 60 \mu\text{s}$	73
A.4. Solutions for a gate time of $\tau_g = 40 \mu\text{s}$	79

1. Introduction

A quantum computer aims to implement and manipulate the quantum mechanical realization of a classical bit. Contrary to a classical bit, that assumes either state 0 or 1, the qubit (quantum bit) can, in principle, occupy any complex superposition state between the quantum mechanical states $|0\rangle$ and $|1\rangle$. Another key property of quantum states is that they can be entangled such that they cannot be described independently from each other anymore. A quantum computer is able to solve certain problems more efficiently than its classical counterpart. For example, Shor's algorithm finds the prime factors of a given integer and Grover's algorithm looks in an unstructured search on a set of elements for a unique element [1].

There are many platforms that have demonstrated successful implementation of a qubit system including superconducting qubits [2], trapped ions [3], quantum dots [4] and nitrogen-vacancy (NV) centers [5].

One of the major challenges in the field is scalability which is necessary to implement more complicated algorithms. A quantum charge-coupled device (QCCD) architecture was proposed as a potential solution [6, 7]. In this architecture, the trap is separated into different regions to which ions can be transported by changing the applied voltages. The regions serve either for storing ions (quantum memory) or for ion manipulation (quantum processor).

To perform any quantum algorithm a set of universal gates is required. These include single-qubit gates as well as two-qubit operations that entangle two qubits. For the platform of trapped ions, these gates are typically implemented by a laser-induced interaction. Moving from a free space implementation of the optics to integrated optics into the trap design is complementary to move towards better scalability. The design also incorporates better stability, addressing precision and power efficiency [8]. Low noise such as vibrations is reduced because the optics is fixed in the chip. Integrated optics allows to focus the laser beam onto an individual ion which is necessary to suppress crosstalk between neighbouring ions. The design allows for simple extensibility towards a larger number of trapped ions.

Figure 1 schematically depicts the experimental setup with the chip containing electrodes to generate the trapping potential. The on-chip trap is a surface electrode trap that was designed by Dr. Karan K. Mehta [8, 9]. The design includes a number of DC and RF electrodes which are intended to form the trapping potential such that ions can be trapped above the chip at a height of 50 μm on the x -direction. Each trapped ion is individually addressed by a waveguide which directs laser light towards the trapping region. The light is then scattered through grating couplers at the trapping region and focused onto the desired ion.

Entangling gates require specific laser pulses which need to be determined for any desired ion pair. These requirements are typically achieved with acousto-optic modulators (AOMs) that shape the laser beam accordingly.

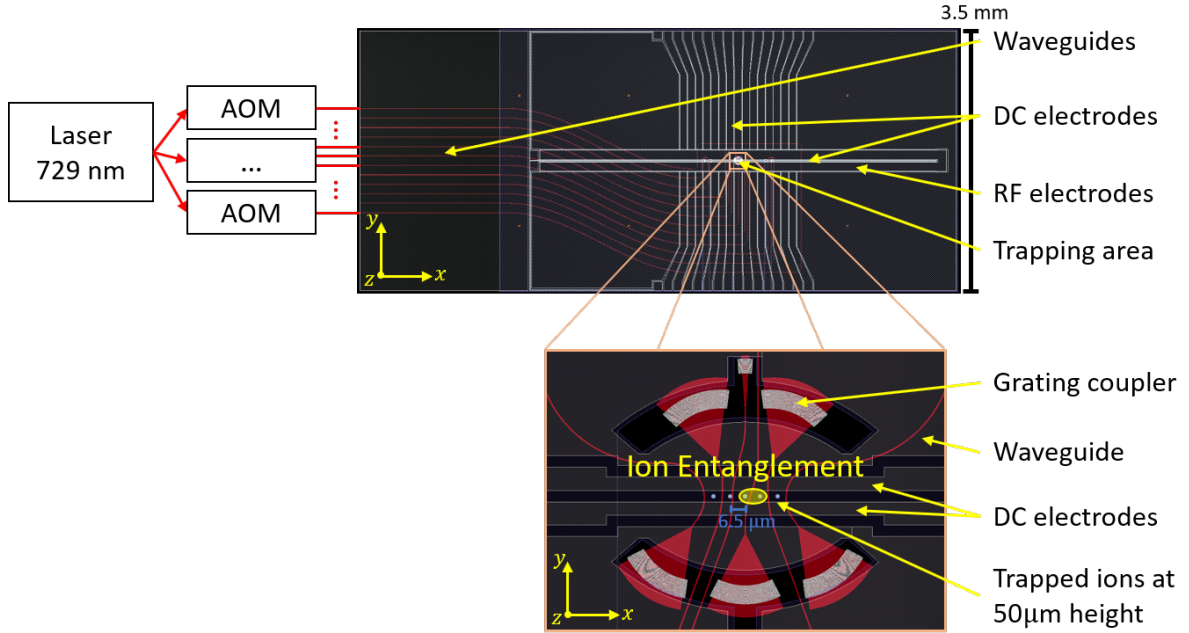


Figure 1: Schematic overview of the optical implementation of entangling ions. Laser light propagates through free space and/or fibers. Its amplitude, frequency and phase is adjusted through AOMs to implement a quantum gate. The laser light is then directed through waveguides towards the trapped ions, scattered at the grating couplers and finally focused onto the desired ions.

For the overall goal to implement an entangling gate for any ion pair, I have computed the requirements on the laser pulse profile for the specific chip design in figure 1. The implementation requires thorough knowledge of the parts involved in this experiment. This includes the investigation of the optical properties of the integrated waveguides in the chip where the waveguide and coupling losses are determined. The characterization of the used AOM is essential to understand experimental effects that influence the result of the entangling gate.

Section 2 recites basic theory of trapped ions. Before looking into the laser beam path, the theory of entangling two ions in a linear ion chain is presented in **section 3**. **Section 4** uses this theory to determine the necessary conditions on the laser to entangle an ion pair. These conditions are realized by shaping the incident laser beam with AOMs. They can be implemented in free space or through a fiber-coupled AOM. The latter is examined in **section 5**. After passing through the AOM, the light is directed through waveguides to the desired ion. In **section 6**, the waveguide chips are characterized and the coupling from fiber to waveguides is examined.

2. Quantum computation with trapped ions

Any platform used for quantum computation needs, on one hand, to be well isolated in order to reduce noise and on the other hand, accessible for the implementation of quantum operations. The isolation for trapped ions is well obtained when the ions are trapped in vacuum. The laser beams directed to the ions and the trapping potential allow for quantum operations.

The basic theory for trapped ions is described in this section. It covers the combined system of an ion and a trapping potential, the laser-ion interaction, and first approximations that will be used later.

2.1. An trapped-ion qubit in a harmonic potential

The two-level nature of a qubit is implemented by choosing two distinct electronic states of an ion. Simplifying the ion as a two-level system, the Hamiltonian is given by

$$H_{\text{ion}} = \frac{\hbar}{2}\omega_0\sigma_z, \quad (1)$$

with the energy difference $\hbar\omega_0$ and the Pauli matrix $\sigma_z = |e\rangle\langle e| - |g\rangle\langle g|$. The work in this thesis is based on $^{40}\text{Ca}^+$ -qubits. Figure 2 shows the relevant energy levels of the $^{40}\text{Ca}^+$ ion. A $^2\text{S}_{1/2}$ energy level is used as the ground state $|g\rangle$ and a $^2\text{D}_{5/2}$ energy level for the excited state $|e\rangle$. The transition frequency ω_0 in equation 1 corresponds to a wavelength of about 729 nm.

As a consequence of the Laplace equation, it is not possible to trap an ion in a static electric field. However, when combined with other fields, it is possible to confine ions in

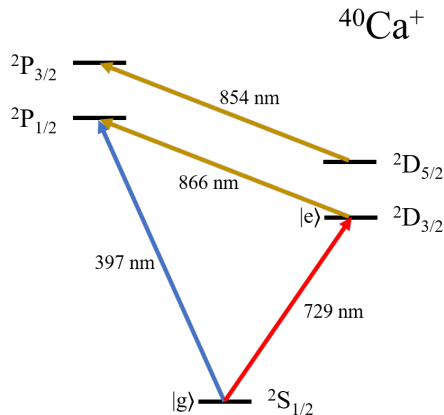


Figure 2: Schematic of relevant Calcium ion energy levels. The qubit is defined by the ground $|g\rangle$ and excited state $|e\rangle$. Transitions between these two states can be driven with 729 nm laser light. The blue laser light (397 nm) is used for state detection. The other two shown transitions are used for optical repumping.

all three spatial dimensions. There are different ways to trap an ion. The *Penning trap* uses a combination of static homogeneous magnetic and inhomogeneous electric fields; the *Paul trap* uses a combination of a static electric field (DC field) and an oscillating electric field (RF field) [10]. The trap we are working with is an implementation of the latter. For a linear Paul trap, the static electric field confines the ion typically in the x -direction, the axial direction. The oscillating field confines the ion in the other two, the radial directions. The RF field can be understood as a rotating potential. The oscillating field confines the ion in the other two, the radial directions.

The RF potential can be understood as a rotating saddle for horseback riding where the rotation axis points towards the sky. If a ball is placed in the middle of the saddle, the constant rotation would make the ball stay inside the saddle corresponding to a confinement in the directions perpendicular to the rotation axis. A charged particle placed inside this potential will be attracted towards the local minimum due to the constant oscillation and thus be confined all dimensions. The solution to the equations of motion reveals oscillations of the ion in all directions with distinct frequencies ω_x , ω_y and ω_z . The interested reader could refer to [10] for further details.

The Paul trap was first fabricated with electrodes shaped like hyperbolic sheets consisting of a shaped cylinder with two end caps [10]. The design then moved to a four-rod ion trap where two opposite rods work either as RF or control electrodes (which define the axial confinement) and ions are trapped between these electrodes. This four-rod design is standard and is used for example in reference [11]. To move towards better scalable traps, the four-rod-design was transformed into a planar surface electrode trap. Possible designs and their implementation are first discussed in [12].

Typically the trapping potential is designed to be harmonic as described by

$$H_{\text{trap}} = \hbar\omega \left(a^\dagger a + \frac{1}{2} \right), \quad (2)$$

where ω denotes the angular frequency of the harmonic oscillator and a^\dagger (a) the creation (annihilation) operator associated with this harmonic oscillator. Equation 2 describes the harmonic potential in one spatial dimension, while there are harmonic potentials in all three dimensions. Also, increasing the number of ions in the trap will naturally increase the number of modes.

2.2. Interaction of an ion with light

So far, the combined system $H_0 = H_{\text{ion}} + H_{\text{trap}}$ consists of individual decoupled parts. Next, we take into account the interaction between these systems induced by a laser, that is described by the Hamiltonian [3]

$$H_{\text{int}} = \frac{\hbar\Omega}{2} \left(e^{i(\vec{k}_L \cdot \vec{x} - \omega_L t + \phi)} \sigma_+ + h.c. \right), \quad (3)$$

where Ω is the Rabi frequency, \vec{k}_L is the wavevector of the laser beam and $\vec{x} = x_0 (a + a^\dagger)$ is the position operator. The size of the motional wavefunction is given by $x_0 = \sqrt{\frac{\hbar}{2M\omega}}$.

The operator $\sigma_+ = |e\rangle\langle g|$ is the raising operator of the two-level system.

We can write the exponential part of the equation by the Lamb-Dicke parameter which is given by

$$\eta = \vec{k}_L \cdot \vec{x}_0 = \frac{2\pi}{\lambda} \sqrt{\frac{\hbar}{2M\omega}} \cos \theta. \quad (4)$$

Here, λ is the wavelength of the laser and M is the ion mass. The angle between the laser beam and the ion's motion is described by θ . The Lamb-Dicke parameter can be interpreted as the relation between the size of the laser wavelength λ relative to the size of the motional wavefunction x_0 . Since the Lamb-Dicke parameter is typically very small, we go to the Lamb-Dicke regime by expanding the exponential in equation 3 to $e^{ik_L \vec{x}} = 1 + i\eta(a + a^\dagger) + \mathcal{O}(\eta^2)$. The use of this expansion up to the first order is valid for $\eta^2(\langle n \rangle + 1/2) \ll 1$ [13].

To further simplify equation 3, we go into the interaction picture with respect to H_0 and get

$$\begin{aligned} H_I &= e^{\frac{i}{\hbar}H_0 t} H_{\text{int}} e^{-\frac{i}{\hbar}H_0 t} \\ H_I &= \frac{\hbar\Omega}{2} e^{i[(\omega_0 - \omega_L)t + \phi]} \sigma_+ \\ &\quad + i\eta \frac{\hbar\Omega}{2} (e^{i[(\omega_0 - \omega - \omega_L)t + \phi]} a\sigma_+ + e^{i[(\omega_0 + \omega - \omega_L)t + \phi]} a^\dagger\sigma_+) + h.c. \end{aligned} \quad (5)$$

Next, we can use the rotating wave approximation (RWA) by going into a reference frame rotating at ω_L . Typically ω_L is selected to be near-resonant to ω_0 or $\omega_0 \pm \omega$, so it is a valid approximation to keep only one term in equation 5 and neglect the other fast-oscillating terms. If $\omega_L = \omega_0 \pm \omega$, the so-called blue (red) sideband transitions are driven which couples the internal state of the ion and its motional state. This means for the red (blue) sideband that we have to lower (raise) the internal state in order to create one quantum of motion and vice versa. In principle, it is possible to apply a time-dependent Rabi frequency $\Omega(t)$. We will exploit this later.

This laser-induced interaction is the basis to entangle qubits within the platform of trapped ions. We will use this Hamiltonian and elaborate its effect in section 3.

3. Entanglement of two ions in a linear ion chain

Apart from essential properties that qubits need to fulfil to implement a quantum algorithm, a universal set of quantum gates is necessary. These gates consist of single qubit rotations that change the state of a single ion and a gate that entangles two qubits. A possible way to entangle ions is the Mølmer-Sørensen gate (MS gate) [14].

This section covers theoretic considerations needed to entangle any two ions within a linear ion chain. First, the axial and radial normal modes are computed, then the Hamiltonian and the propagation operator of the gate is derived and finally, the expected fidelity of the gate operation determined. The results are used in section 4 to compute the optimal pulse shape for the entanglement of an ion pair within a linear ion chain.

3.1. Normal modes of coupled trapped-ion oscillators

As described in the previous section, the trapping potential makes the ion oscillate in all dimensions. This oscillation is described by the normal mode frequencies. We distinguish here between the axial normal modes which are along the trap axis (x -direction in our case) and the radial normal modes in y - and z -direction. The normal modes are driven to entangle ions. Therefore, we need to know their frequencies.

This section will give a summary of the calculations in order to obtain the normal mode frequencies. The approach mainly follows [15].

3.1.1. Axial normal modes

First the equilibrium positions for a linear chain of N ions in a trap considering the axial normal modes are determined. We assume that the trapped ions are strongly bound in the y - and z -direction. In the x -direction, which is the direction of the trap axis, the ions are assumed to be weakly bound in a harmonic potential. The position of ion s is denoted by $x_s(t)$. The motion along the other axes is neglected under the assumption that the binding potential is sufficiently strong. The potential energy of the ion chain is then given by

$$V = \sum_{n=1}^N \frac{1}{2} M \omega_x^2 x_n(t)^2 + \sum_{\substack{n,m=1 \\ n \neq m}}^N \frac{Z^2 e^2}{8\pi\epsilon_0} \frac{1}{|x_n(t) - x_m(t)|}, \quad (6)$$

where M is the mass of the ion, ω_x is the trap frequency which characterizes the strength of the trapping potential in the axial direction, e is the electron charge and ϵ_0 is the vacuum permittivity. The degree of ionization of the ions is given by Z , which is 1 for $^{40}\text{Ca}^+$.

After the ions are laser cooled, it is valid to approximate the position of the s -th ion as $x_s(t) \approx x_s^{(0)} + q_s(t)$, where $x_s^{(0)}$ denotes the equilibrium position and $q_s(t)$ a small displacement from the latter. With this, the equilibrium position of ion s can be found

using $\frac{\partial V}{\partial x_s} \Big|_{x_s=x_s^{(0)}} = 0$. Defining the length scale l as $l^3 = \frac{Z^2 e^2}{4\pi\epsilon_0 M \omega_x^2}$, the equilibrium positions are made dimensionless by $u_s = x_s^{(0)}/l$. To find the equilibrium positions, the following equation needs to be solved

$$u_s - \sum_{m=1}^{s-1} \frac{1}{|u_s - u_m|^2} + \sum_{m=s+1}^N \frac{1}{|u_s - u_m|^2} = 0, \quad \text{for } s = 1, \dots, N. \quad (7)$$

This equation can only be analytically solved for $N \leq 3$ and else needs to be solved numerically.

Given the correct equilibrium positions of the ions in the linear ion chain, the next step is to look at the displacements of the ions from their equilibrium positions. These motions are described by the Lagrangian

$$L = \frac{M}{2} \sum_{n=1}^N (\dot{q}_n)^2 - \frac{1}{2} \sum_{n,m=1}^N q_n q_m \frac{\partial^2 V}{\partial x_n \partial x_m} \Big|_0 = \frac{M}{2} \left[\sum_{n=1}^N (\dot{q}_n)^2 - \omega_x^2 \sum_{n,m=1}^N A_{nm} q_n q_m \right], \quad (8)$$

where terms $O(q_s^3)$ are neglected. The subscript 0 at the derivative indicates that the expression is evaluated at the equilibrium positions of x_n and x_m . The matrix A_{nm} is given by

$$A_{nm} = \begin{cases} 1 + 2 \sum_{\substack{p=1 \\ p \neq m}}^N \frac{1}{|u_m - u_p|^3}, & \text{if } n = m \\ \frac{-2}{|u_m - u_n|^3}, & \text{if } n \neq m. \end{cases} \quad (9)$$

This matrix is the underlying basis for the description of the axial normal modes. Its eigenvectors v_p with eigenvalue ψ_p correspond to the axial normal mode p with a relative displacement of the k -th ion as given by the k -th component of the p -th eigenvector. The angular frequency of the p -th mode is $\omega_{x,p} = \sqrt{\psi_p} \omega_x$.

3.1.2. Radial normal modes

Similar to the axial modes, the equilibrium positions for a linear chain of N ions in a trap are determined first. Looking for the radial modes in y -direction, the motion in z -direction is neglected and vice versa. The approach for both directions is the same, therefore, the label r for radial is used as a substitute for y, z . The next approximation assumes that the ions are in the equilibrium position in the x -direction. The potential energy looks similar to equation 6 and is within this approximation given by

$$V = \sum_{n=1}^N \frac{1}{2} M \omega_r^2 r_n(t)^2 + \sum_{\substack{n,m=1 \\ n \neq m}}^N \frac{Z^2 e^2}{8\pi\epsilon_0} \frac{1}{\sqrt{\left(x_n^{(0)} - x_m^{(0)}\right)^2 + (r_n(t) - r_m(t))^2}}, \quad (10)$$

where ω_r is the confining frequency in r -direction.

In the case of any radial displacement the equilibrium positions are $r_s^{(0)} = 0$, however, if desired, this can be checked by computing $\frac{\partial V}{\partial r_s} \Big|_{r_s=r_s^{(0)}} = 0$.

The motions are described by almost the same Lagrangian as in the axial case in equation 8, namely

$$L = \frac{M}{2} \sum_{n=1}^N (\dot{q}_n)^2 - \frac{1}{2} \sum_{n,m=1}^N q_n q_m \frac{\partial^2 V}{\partial r_n \partial r_m} \Big|_0 = \frac{M}{2} \left[\sum_{n=1}^N (\dot{q}_n)^2 - \omega_r^2 \sum_{n,m=1}^N B_{nm} q_n q_m \right], \quad (11)$$

where the subscript 0 at the derivative indicates that the expression is evaluated at the equilibrium positions of r_n and r_m . For a simpler presentation, another length scale l_r is defined by $l_r^3 = \frac{Z^2 e^2}{4\pi\epsilon_0 M \omega_r^2}$. Then the matrix B_{nm} is given by

$$B_{nm} = \begin{cases} 1 - \frac{l_r^3}{l^3} \sum_{s=1, s \neq m}^N \frac{1}{|u_m - u_p|^3}, & \text{if } n = m \\ \frac{l_r^3}{l^3} \frac{1}{|u_m - u_n|^3}, & \text{if } n \neq m. \end{cases} \quad (12)$$

This matrix is the underlying basis for the description of the radial normal modes. Its eigenvectors b_p with eigenvalue ζ_p correspond to the radial normal mode p with a relative displacement of the k -th ion given by the k -th component p -th eigenvector. The first mode is called center of mass mode where all ions are oscillating in phase. The angular frequency of the p -th mode are $\omega_{r,p} = \sqrt{\zeta_p} \omega_r$.

The radial modes in z -direction within this thesis, its frequencies and displacements are depicted in figure 3. The confining frequency in z -direction is $\omega_z = 2\pi \times 3.5$ MHz. These are the most important modes for our experiment, because the laser-induced interaction that was discussed in section 2.2 will be driven in the vicinity of these modes.

3.2. Derivation of propagation operator

The normal modes of the previous section have prepared us to derive the effect of the interaction Hamiltonian that I have briefly introduced in section 2.2. The action of any Hamiltonian is typically described by the propagation operator. Since the propagation operator is a time-dependent operator, the application of the interaction on an initial state will lead to a time-dependent final state. If we set the parameters and the duration of the laser-induced interaction appropriately, we obtain the desired entangling gate.

In this section the Hamiltonian of the desired entangling gate is derived. Starting from a simple Hamiltonian with one ion and a laser beam, the theory is built up to a linear ion chain with N ions where two laser beams are applied to two selected ions. The effect of these gates is discussed.

3.2.1. One ion and one bichromatic laser

The propagation operator for the simplest case with one ion, one motional mode and a bichromatic laser is derived. The derivation mainly follows the approaches in [16, 17].

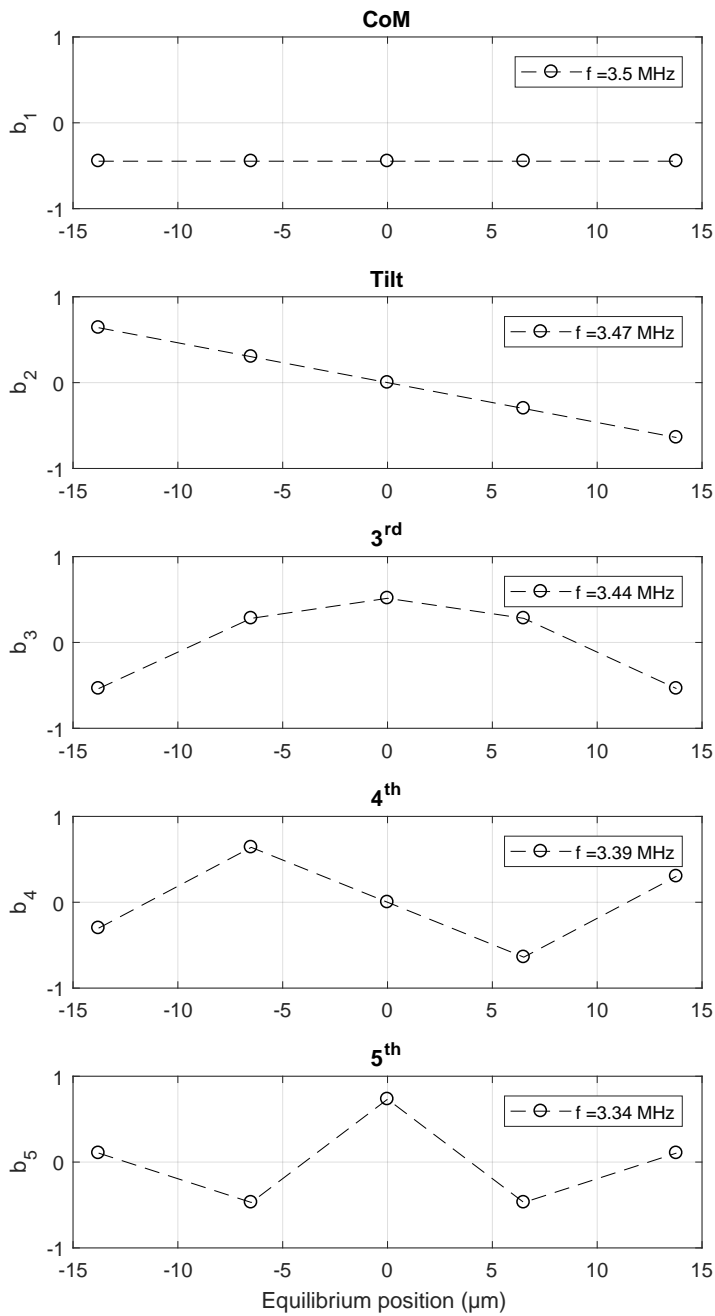


Figure 3: Radial normal modes in z -direction. The equilibrium position is with respect to the trap axis. The y -axis shows the normalized eigenvector elements of the matrix B in equation 12 indexed by the position of each ion. The mode with the highest frequency is the common mode, the second one is the tilt mode. The following modes are typically labelled numerically by third, fourth and fifth mode.

The Hamiltonian that describes one trapped ion that interacts with a laser field is given by

$$\boxed{\begin{aligned} H_{\text{tot}} &= H_0 + H_{\text{int}} \\ H_0 &= \hbar\omega \left(a^\dagger a + \frac{1}{2} \right) + \frac{\hbar\omega_0}{2} \sigma_z \\ H_{\text{int}} &= \frac{\hbar\Omega}{2} \left(e^{i(\vec{k}_L \cdot \vec{x} - \omega_L t + \phi)} \sigma_+ + h.c. \right) \end{aligned}} \quad (13)$$

In the Hamiltonian H_0 the quantity ω represents the mode frequency of the only mode we are considering, while we keep in mind that in reality we have three modes. The energy difference between the ground and excited state of the qubit is given by $\hbar\omega_0$.

In the interaction Hamiltonian H_{int} the Rabi frequency is given by Ω , \vec{k}_L denotes the wavevector of the laser with frequency $\omega_L = \omega_0 + \mu$ and phase ϕ and σ_\pm is the raising (lowering) operator for the spin state of the ion.

As described in section 2.2, the next step is to go to the interaction picture with respect to H_0 and to the Lamb-Dicke regime to simplify the interaction Hamiltonian to

$$H_I = \frac{\hbar\Omega}{2} \sigma_+ e^{i\mu t + i\phi} (1 + i\eta(a^\dagger e^{i\omega t} + ae^{-i\omega t})) + h.c., \quad (14)$$

where $\eta = \frac{2\pi}{\lambda} \cos\theta \sqrt{\frac{\hbar}{2M\omega}}$. The angle θ describes the angle between the wavevector of the laser and the direction of the ion's motion \vec{x} .

Next we consider a bichromatic laser field with Rabi frequencies $\Omega_r = \Omega_b = \Omega/2$ and frequencies $\omega_L = \omega_0 \pm \mu$ where r stands for a red-shifted ($-\mu$) and b for a blue-shifted field ($+\mu$) with phases ϕ_r, ϕ_b , and therefore, we substitute $e^{-i(\mu t - \phi)} \mapsto e^{-i(\mu t - \phi_b)} + e^{i(\mu t + \phi_r)}$. Using the definitions $\phi_s = \frac{1}{2}(\phi_b + \phi_r)$ and $\phi_d = \frac{1}{2}(\phi_r - \phi_b)$, we can find that [17]

$$\begin{aligned} e^{-i(\mu t - \phi)} &\mapsto e^{-i(\mu t - \phi_b)} + e^{i(\mu t + \phi_r)} = e^{i\phi_s} 2 \cos(\mu t + \phi_d) \\ \Rightarrow H_I &= \hbar \frac{\Omega}{2} \sigma_+ e^{i\phi_s} \cos(\mu t + \phi_d) (1 + i\eta(a^\dagger e^{i\omega t} + ae^{-i\omega t})) + h.c. \\ &= \hbar\Omega \cos(\mu t + \phi_d) (\sigma_{-\phi_s} - [\eta(a^\dagger e^{i\omega t} + ae^{-i\omega t}) \sigma_{\pi/2 - \phi_s}]) \end{aligned} \quad (15)$$

$$H_{I,\Omega \ll \mu} \approx -\hbar\Omega \cos(\mu t + \phi_d) \eta (a^\dagger e^{i\omega t} + ae^{-i\omega t}) \sigma_{\pi/2 - \phi_s}, \quad (16)$$

where $\sigma_\phi = \cos\phi \sigma_x + \sin\phi \sigma_y$. The regime $\Omega \ll \mu$ describes the situation where the laser intensities are not too strong. In this regime, we may neglect the off-resonant carrier drive [18]. The effect of the first term that is neglected within the last approximation is dealt with in section 3.3.3. The MS gate is performed in the basis $\sigma_\phi \otimes \sigma_\phi$. Without loss of generality we can pick $\phi_s = -\pi/2$ for our calculations which leads to $-\sigma_{\pi/2 - \phi_s} = \sigma_x$. We will use this approach in the following.

In principle, we can simplify the Hamiltonian further to [16]

$$\begin{aligned} H_I &= \hbar\Omega \cos(\mu t + \phi_d) \sigma_{-\phi_s} - \frac{\hbar\Omega}{2} \eta \sigma_{\pi/2-\phi_s} (a^\dagger e^{i[(\omega-\mu)t+\phi_d]} + a e^{-i[(\omega-\mu)t+\phi_d]}) \\ &\quad - \frac{\hbar\Omega}{2} \eta \sigma_{\pi/2-\phi_s} (a^\dagger e^{i[(\omega+\mu)t-\phi_d]} + a e^{-i[(\omega+\mu)t-\phi_d]}) \\ H_{I,\text{RWA}} &\approx - \frac{\hbar\Omega}{2} \eta \sigma_{\pi/2-\phi_s} (a^\dagger e^{i[(\omega-\mu)t+\phi_d]} + a e^{-i[(\omega-\mu)t+\phi_d]}). \end{aligned} \quad (17)$$

In the last step, the rotating wave approximation (RWA) was applied. 

The propagator based on equation 16 is then calculated using **Magnus formula** [19] 

$$U(t) = \exp \left(-\frac{i}{\hbar} \int_0^t H_I(t') dt' + \frac{1}{2\hbar^2} \int_0^t \int_0^{t'} [H_I(t'), H_I(t'')] dt'' dt' + \dots \right). \quad (18)$$

In this approximation, all terms that are of higher order vanish due to the commutation relations of the creation and annihilation operator a, a^\dagger . If we consider the more general case where the **Rabi frequency is time-dependent**, we get

$$\begin{aligned} U_{\Omega \ll \mu}(t) &= \mathcal{D}(\alpha(t)) \sigma_x e^{i\chi(t)\sigma_x^2} \quad \text{with} \quad (19) \\ \alpha(t) &= i\eta \int_0^t \Omega(t') \cos(\mu t' + \phi_d) e^{i\omega_p t'} dt' \\ \chi(t) &= \eta^2 \int_0^t \int_0^{t'} \Omega(t') \Omega(t'') \cos(\mu t' + \phi_d) \cos(\mu t'' + \phi_d) \sin((\omega_p - \mu)(t' - t'')) dt'' dt'. \end{aligned}$$

In this equation, $\mathcal{D}(\alpha) = e^{[\alpha(t)a^\dagger - \alpha^*(t)a]}$ is the displacement operator. The displacement in phasespace of the mode is described by $\alpha(t)$.

This Hamiltonian implements a **single ion gate**. The exponential term in the operator induces a phase. If the displacement is closed at the end of the gate $\alpha(\tau_g) = 0$, the induced phase $\chi(\tau_g)$ corresponds to the area of the path through phase-space. The displacement operator entangles the internal state of the ion with its motional state. Since we are interested in entangling gates of two ions, we will repeat the same steps with the more complex setting of N trapped ions.

3.2.2. Linear chain of N ions and two bichromatic lasers

The Hamiltonian for N trapped ions addressed by two monochromatic laser beams is given by

$$\begin{aligned} H_{\text{tot}} &= H_0 + H_{\text{int}} \quad (20) \\ H_0 &= \sum_{p=1}^{3N} \hbar\omega_p \left(a_p^\dagger a_p + \frac{1}{2} \right) + \sum_{r=1}^N \frac{\hbar\omega_0}{2} \sigma_{z,r} \\ H_{\text{int}} &= \sum_{s=1}^2 \frac{\hbar\Omega_s(t)}{2} \left(e^{i(\vec{k}_s \cdot \vec{x}_s - \omega_s t + \phi_s)} \sigma_{+,s} + h.c. \right) \end{aligned}$$

Note that here $\vec{k}_s \cdot \vec{x}_s = \frac{2\pi}{\lambda} \cos(\theta) \sum_p \sqrt{\frac{\hbar}{2M\omega_p}} \cdot b_p^{(s)} (a_p + a_p^\dagger) = \sum_p \eta_{p,s} (a_p + a_p^\dagger)$. The quantity $b_p^{(s)}$ is given by the computation of the equilibrium positions of the normal modes in the potential as computed in section 3.1 [15]. Index p labels the different modes, index r labels the trapped ions and index s labels the two ions, that are addressed by a laser beam.

We repeat the steps in section 3.2.1 and go to the interaction picture with respect to H_0 , followed by the Lamb-Dicke approximation and finally making each laser bichromatic, we find

$$H_{I,\Omega_s \ll \mu} = \sum_s \hbar \Omega_s(t) \cos(\mu t + \phi_{d,s}) \sigma_{x,s} \sum_p \eta_{p,s} (a_p^\dagger e^{i\omega_p t} + a_p e^{-i\omega_p t}) \quad (21)$$

In order to compute the propagation operator, we again use the Magnus expansion and find assuming $\phi_{d,s} = \phi_d$

$$\begin{aligned} U(t) &= \exp \left(\sum_s \xi_s(t) \sigma_{x,s} + i \sum_{k,l} \chi_{k,l} \sigma_{x,k} \sigma_{x,l} \right) \quad (22) \\ \xi_s(t) &= \sum_p [\alpha_{s,p}(t) a_p^\dagger - \alpha_{s,p}^*(t) a_p], \text{ where } \alpha_{s,p}(t) = i \eta_{s,p} \int_0^t \Omega_s(t') \cos(\mu t' + \phi_d) e^{i\omega_p t'} dt' \\ \chi_{k,l}(t) &= \sum_p \eta_{k,p} \eta_{l,p} \int_0^t \int_0^{t'} \Omega_k(t') \Omega_l(t'') \cos(\mu t' + \phi_d) \cos(\mu t'' + \phi_d) \\ &\quad \sin[(\omega_p - \mu)(t' - t'')] dt' dt'' \end{aligned}$$

The displacement in phasespace of the p -th mode is described by $\alpha_{s,p}(t)$ and the spin-spin interaction of ions k and l is given by $\chi_{k,l}(t)$.

Note that compared to [20], there is an additional factor of 2 in the definition of $\chi_{i,j}$ which takes into account that we have also $\chi_{j,i}$ which depends on the definition of the double sum. Additionally, we would need to pick $\phi_d = -\pi/2$ to have a sine rather than a cosine to be consistent. This phase also has an effect on the fidelity which will be discussed in the next section.

The goal of the MS-gate is to entangle the electronic state of two trapped ions while keeping the motional states disentangled. This disentanglement is achieved by $\xi_s(\tau_g) = 0$ at the gate time τ_g for all s . We reach maximal entanglement of ion a and b for $\chi_{a,b}(\tau_g) = \pm\pi/4$.

We can show that these conditions satisfy the goal of the entangling gate by application

of the propagator operator for the initial state $|00\rangle$

$$\begin{aligned}
U(\tau_g)|00\rangle &= e^{\pm i\pi/4} \frac{|++\rangle + |--\rangle}{2} + e^{\mp i\pi/4} \frac{|+-\rangle + |-+\rangle}{2} \\
&= \frac{e^{\pm i\pi/4}}{2} (|++\rangle + |--\rangle \mp i[|+-\rangle + |-+\rangle]) \\
&= \frac{e^{\pm i\pi/4}}{\sqrt{2}} (e^{\mp i\pi/4}|00\rangle + e^{\pm i\pi/4}|11\rangle) \\
&= \frac{|00\rangle \pm i|11\rangle}{\sqrt{2}},
\end{aligned} \tag{23}$$

where we defined $|0\rangle = \begin{pmatrix} 0 \\ 1 \end{pmatrix}$ and $|1\rangle = \begin{pmatrix} 1 \\ 0 \end{pmatrix}$ and used the relations $|\pm\rangle = \frac{|0\rangle \pm |1\rangle}{\sqrt{2}}$.

To get an intuition of the time evolution of the gate, we consider a constant Rabi frequency. Without loss of generality we consider the entanglement of ion 1 and 2. The first part of the propagation operator can be brought back to the form of the displacement operator:

$$\begin{aligned}
\exp\left(\sum_{s=1}^2 \xi_s(t) \sigma_{x,s}\right) &= \exp\left(\sum_{s=1}^2 \sum_p [\alpha_{s,p}(t) a_p^\dagger - \alpha_{s,p}^*(t) a_p] \sigma_{x,s}\right) \\
&= \exp\left(\sum_{s=1}^2 \sum_p [\alpha_p(t) a_p^\dagger - \alpha_p^*(t) a_p] \eta_{s,p} \sigma_{x,s}\right) \\
&= \sum_{n=0}^{\infty} \frac{1}{n!} \left(\sum_p \alpha_p(t) a_p^\dagger - \alpha_p^*(t) a_p \right)^n (\eta_{1,p} \sigma_{x,1} + \eta_{2,p} \sigma_{x,2})^n,
\end{aligned}$$

where we defined $\alpha_{s,p} = \eta_{s,p} \alpha_p$. Now, we can apply the second part to the internal state of the ion, where we receive a real number that depends on the Lamb-Dicke parameter $\eta_{s,p}$ and on the internal ion. Since the number is real, we will absorb it into α_p and call write $\tilde{\alpha}_p$ instead.

$$\begin{aligned}
&\exp\left(\sum_{s=1}^2 \xi_s(t) \sigma_{x,s}\right) |\Psi_{\text{spin}}\rangle \\
&\Rightarrow \sum_{n=0}^{\infty} \frac{1}{n!} \left(\sum_p \tilde{\alpha}_p(t) a_p^\dagger - \tilde{\alpha}_p^*(t) a_p \right)^n = \exp\left(\sum_p \tilde{\alpha}_p(t) a_p^\dagger - \tilde{\alpha}_p^*(t) a_p\right) = \prod_p \mathcal{D}(\tilde{\alpha}_p(t))
\end{aligned}$$

Then the form of the propagation operator is $\prod_p \mathcal{D}(\tilde{\alpha}_p(t)) e^{i\chi_{1,2}}$. The propagation operator is now of a similar form as for the case of the interaction of one ion with one laser. Therefore, we conclude that all modes contribute to the phase $\chi_{1,2}$.

The actual time-dependent action of the gate for a constant Rabi frequency is displayed in figure 4. For simplicity, we assume $\eta_{s,p} = \eta$. At the beginning of the gate the qubits

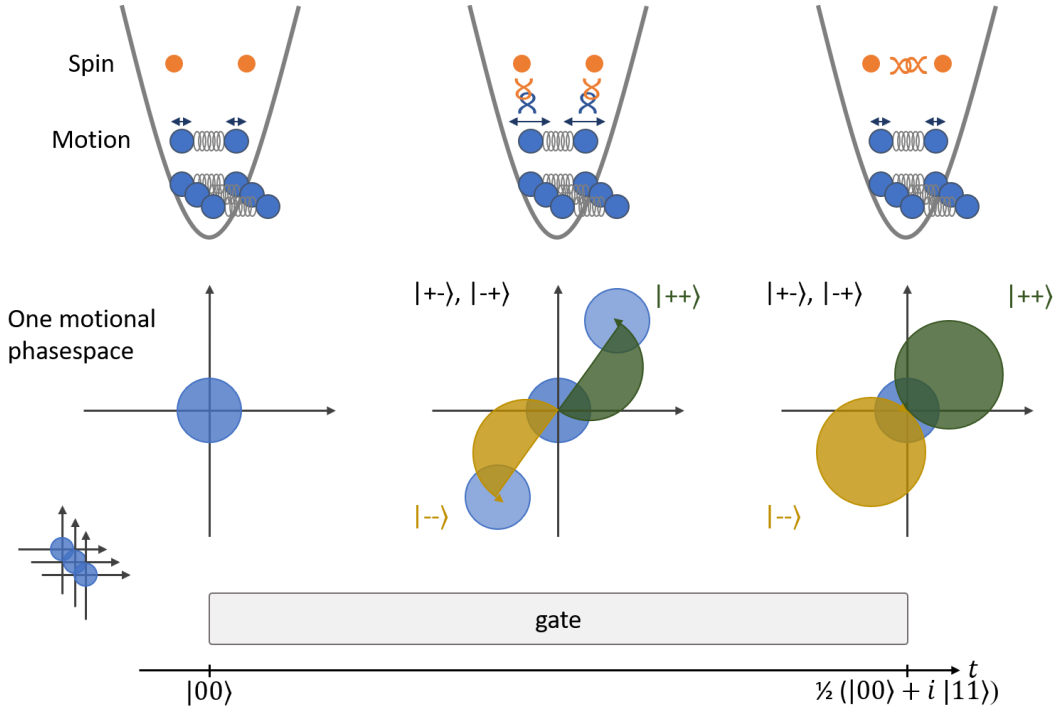


Figure 4: Time evolution of the MS-gate as calculated in equation 23. The top shows the ions and the motional states. The arrows above the motional states indicate their excitation. The entanglement of an ion with another ion or its motional state is indicated by \propto . The schematic below shows the phasespace trajectory of one motional mode as a function of time in green and yellow dependent on the state. The blue indicates the spread of the motional wavepacket. If it is centered at the origin, the motional state is in the groundstate. The accumulated phase is given by the area that is enclosed through the phasespace trajectory of all modes. Adapted after [21].

are disentangled from their motional state. The phasespace trajectory $\alpha(t)$ evolves as a function of time. The motional states are excited and get entangled with the electronic state of the ion. We observe that the motional states for ion states $|+-\rangle$ and $|--\rangle$ are not displaced in phasespace. At the end of the gate, the phasespace trajectories close which disentangles the ions from their motional state.

We have not yet discussed how these conditions are actually achieved in the experiment. The idea is to implement different Rabi frequency levels over time which satisfy the mentioned conditions above. For the case of two trapped ions a simple square pulse satisfies the constraints. The exact details will be discussed in section 4. Before, we will determine a measure of how well the gate can be theoretically implemented, which is the gate fidelity.



3.3. Gate fidelity

We have prepared the theory for the MS-gate in order to determine the optimal pulse sequence to entangle two ions. As a measure of how well the pulse sequences are, we need to estimate the fidelity. In this analysis, we take several imperfections into account: The displacement of all modes at the end of the gate is a source of infidelity, since the ion is entangled with its motion if $\alpha(\tau_g) \neq 0$. If the laser pulses have a slightly higher or lower power than desired, the spin-spin interaction $\chi(\tau_g)$ is slightly different. So far, we also have assumed that all motional modes are in their ground states, however, in reality cooling techniques allow only for an approximate ground state. Additionally to these experimental parameters, we also exploit the effect of the phase difference ϕ_d of the bichromatic laser beam and take into account the off-resonant carrier excitation that we have neglected in the theory above.

3.3.1. Expected theoretical fidelity

For the fidelity calculation, we follow the approach in reference [22]. Without loss of generality the propagation operator, where ion 1 and 2 are entangled, is used for computation. The internal state of the other ions that are not part of the gate will be unaffected. For simplicity and better readability only the two ions that are entangled are kept in this calculation. The calculations are performed in the σ_z basis, which is easier to calculate with, because the eigenstates for the necessary matrices are the same. The result for the σ_x basis is, however, the same since the fidelity is independent of the used basis [23].

Using the above definitions the propagation operator is given by

$$\begin{aligned} U_{1,2}(\tau) &= e^{\xi_1(\tau)\sigma_{z,1} + \xi_2(\tau)\sigma_{z,2} + i\chi_{1,2}(\tau)\sigma_{z,1}\sigma_{z,2}} \\ &= e^{\xi_1(\tau)\sigma_{z,1}} e^{\xi_2(\tau)\sigma_{z,2}} e^{i\chi_{1,2}(\tau)\sigma_{z,1}\sigma_{z,2}}. \end{aligned} \quad (24)$$

Here we used in the last step that the terms in the exponential commute. This is obvious for the Pauli matrices, but not so clear for the creation and annihilation operators of the same modes in ξ_s . To check whether $e^{\xi_1(\tau)\sigma_{z,1} + \xi_2(\tau)\sigma_{z,2}} = e^{\xi_1(\tau)\sigma_{z,1}} e^{\xi_2(\tau)\sigma_{z,2}}$ holds, we need to check the commutation relation for a single mode which is

$$\begin{aligned} &[\alpha_1(\tau)a^\dagger - \alpha_1^*(\tau)a, \alpha_2(\tau)a^\dagger - \alpha_2^*(\tau)a] \\ &= -\alpha_1(\tau)\alpha_2^*(\tau)[a^\dagger, a] - \alpha_1^*(\tau)\alpha_2(\tau)[a, a^\dagger] \\ &= \alpha_1(\tau)\alpha_2^*(\tau) - \alpha_1^*(\tau)\alpha_2(\tau). \end{aligned}$$

To understand that this relation is zero, we recall the definition of α in equation 22. The only complex parts in the definition are exactly the same for both α 's which makes the commutation relation above vanish. Different modes commute by definition.

To increase readability, we will suppress of τ in each of the variables, while we keep in mind that these variables are time dependent.

We expand the propagation operator in the eigenbasis. The eigenvalues (λ, μ, γ) and eigenstates for three different operators are given by

$$\sigma_{z,1} \cdot \sigma_{z,2} = \begin{pmatrix} 1 & 0 & 0 & 0 \\ 0 & -1 & 0 & 0 \\ 0 & 0 & -1 & 0 \\ 0 & 0 & 0 & 1 \end{pmatrix} \Rightarrow \lambda = 1 \text{ for } |00\rangle, |11\rangle \text{ and } \lambda = -1 \text{ for } |01\rangle, |10\rangle \quad (25)$$

$$\sigma_{z,1} = \begin{pmatrix} 1 & 0 & 0 & 0 \\ 0 & 1 & 0 & 0 \\ 0 & 0 & -1 & 0 \\ 0 & 0 & 0 & -1 \end{pmatrix} \Rightarrow \mu = 1 \text{ for } |11\rangle, |10\rangle \text{ and } \mu = -1 \text{ for } |01\rangle, |00\rangle \quad (26)$$

$$\sigma_{z,2} = \begin{pmatrix} 1 & 0 & 0 & 0 \\ 0 & -1 & 0 & 0 \\ 0 & 0 & 1 & 0 \\ 0 & 0 & 0 & -1 \end{pmatrix} \Rightarrow \gamma = 1 \text{ for } |11\rangle, |01\rangle \text{ and } \gamma = -1 \text{ for } |10\rangle, |00\rangle. \quad (27)$$

Without loss of generality we pick $|\Psi_0\rangle = |++\rangle$ as the initial state, set $\chi_{1,2} = \pi/4$ and find the expansion

$$U(\tau_g) |\Psi_0\rangle = \sum_{\lambda, \mu, \gamma} e^{i\frac{\pi}{4}\lambda} |\lambda\rangle \langle \lambda| \prod_p \mathcal{D}(\alpha_{1,p}\mu) |\mu\rangle \langle \mu| \mathcal{D}(\alpha_{2,p}\gamma) |\gamma\rangle \langle \gamma| |\Psi_0\rangle. \quad (28)$$

The sum over λ, μ, γ is a sum over all possible eigenstates $\{|00\rangle, |01\rangle, |10\rangle, |11\rangle\}$ and the corresponding eigenvalue as indexed by the matrices. Since all eigenstates for each of the expansions are orthogonal, we can simplify the expression very much. Note that the eigenstates for each matrix above are the same, however, they have different eigenvalues. For example, $|00\rangle$ is an eigenstate of $\sigma_z \otimes \sigma_z$ with eigenvalue 1, but the eigenvalue for $\sigma_z \otimes \mathbb{1}$ and $\mathbb{1} \otimes \sigma_z$ is -1 for this eigenstate. Therefore, we need an additional index in the eigenvalues corresponding to the state that the sum refers to. Also, we have to consider the thermal state of the ion's motion $\rho_{\text{th}} = \otimes_p \rho_{\text{th},p}$, $\rho_{\text{th},p} = \sum_{n_p=0}^{\infty} \frac{\bar{n}_p^{n_p}}{(1+\bar{n}_p)^{n_p+1}} |n_p\rangle \langle n_p|$, where $|n_p\rangle$ are Fock states. Since the final state will not be pure, we have to work with density matrices at this stage. For the spin state after the gate, we find

$$\rho_{\text{spin}}(\tau_g) = \frac{1}{4} \sum_{\lambda, \tilde{\lambda}} e^{i\frac{\pi}{4}(\lambda - \lambda_{\tilde{\lambda}})} |\lambda\rangle \langle \tilde{\lambda}| \prod_p \text{tr}_{\text{th},p} [\mathcal{D}(\alpha_{1,p}\mu_{\lambda} + \alpha_{2,p}\gamma_{\lambda}) \rho_{\text{th}} \mathcal{D}^{\dagger}(\alpha_{1,p}\mu_{\tilde{\lambda}} + \alpha_{2,p}\gamma_{\tilde{\lambda}})],$$

where we used that $\mathcal{D}(\beta)\mathcal{D}(\alpha) = e^{i\text{Im}(\beta\alpha^*)}\mathcal{D}(\alpha + \beta)$. In order to compute the trace of

this expression, we need to use the following definitions and tricks [24]

$$\begin{aligned} \text{tr}_p (\mathcal{D}(\beta_i) \rho_{\text{th},p} \mathcal{D}^\dagger(\mu_j)) &= e^{-i\text{Im}(\mu_j \beta_i^*)} \sum_{n=0}^{\infty} \langle n | \mathcal{D}(\beta_i - \mu_j) \rho_{\text{th},p} | n \rangle \\ \langle n | \mathcal{D}(\alpha) | n \rangle &= e^{-\frac{1}{2}|\alpha|^2} L_n^0(|\alpha|^2) \\ \sum_{n=0}^{\infty} L_n^\vartheta(z) \omega^n &= (1 - \omega)^{-\vartheta-1} e^{\frac{\omega z}{\omega-1}}. \end{aligned}$$

Here, L denotes the Laguerre polynomials.

Applying this set of calculations to our case, the spin state is given by

$$\rho_{\text{spin}}(\tau_g) = \frac{1}{4} \sum_{\lambda, \tilde{\lambda}} e^{i\frac{\pi}{4}(\lambda_\lambda - \lambda_{\tilde{\lambda}})} |\lambda\rangle \langle \tilde{\lambda}| \prod_p \exp \left[-|\alpha_{1,p}(\mu_\lambda - \mu_{\tilde{\lambda}}) + \alpha_{2,p}(\gamma_\lambda - \gamma_{\tilde{\lambda}})|^2 \left(\bar{n}_p + \frac{1}{2} \right) \right]$$

In order to compute the fidelity, we need to define a state to which we want to compare our gate. For this we apply the perfect gate, where all $\alpha_{n,p} = 0$ and $\chi_{1,2} = \pi/4$, to the initial state. Then we get $|\Psi_f\rangle = \frac{1}{2}e^{i\frac{\pi}{4}} [|00\rangle - i|01\rangle - i|10\rangle + |11\rangle]$. The fidelity is then given by

$$\begin{aligned} \mathcal{F} &= \langle \Psi_f | \rho_{\text{spin}}(\tau_g) | \Psi_f \rangle \\ &= \frac{1}{8} [2 + 2(\Gamma_1 + \Gamma_2) + \Gamma_+ + \Gamma_-] \end{aligned} \quad (29)$$

where $\Gamma_s = \exp \left[-4 \left(\bar{n} + \frac{1}{2} \right) \sum_p |\alpha_{s,p}|^2 \right]$ and $\Gamma_\pm = \exp \left[-4 \left(\bar{n} + \frac{1}{2} \right) \sum_p |\alpha_{1,p} \pm \alpha_{2,p}|^2 \right]$. Here we assumed $\bar{n}_p = \bar{n}$ for all p . For the general case where we don't know if $\chi_{1,2} = \pi/4$ is in fact implemented, the fidelity is changed where $\Gamma_s(\chi_{1,2}) \mapsto \sin(2\chi_{1,2})\Gamma_s(\frac{\pi}{4})$.

Comparing Γ_s, Γ_\pm to the result in [22], we note that there is an additional factor of 4 in the exponential. However, a detailed calculation of the fidelity in [25] indicates that this factor is indeed there. I have also been in touch with Dr. Caroline Figgatt [23] who agrees with me.

Based on the formula for the fidelity, we can now check the effect of experimental imperfections. We observe that the higher the mean phonon number \bar{n}_p of motional state p , the lower the fidelity. If the constraint $\alpha(\tau_g) = 0$ is badly satisfied, the fidelity decreases. The same effect can be observed, if the spin-spin interaction is not exactly $\pi/4$ but slightly different.

3.3.2. Effect of the phase difference of the laser beams

In the Hamiltonian shown in equation 16 we have neglected the off-resonant drive of carrier transition and not used the phase $\phi_d = \frac{1}{2}(\phi_r - \phi_b)$. The effect of this phase is presented and discussed in detail in [26] which is summarized in the following.

To understand the effect of the phase on the implemented gate, the Hamiltonian in equation 15 is investigated from a different perspective by interpreting it as a single laser beam resonant with the carrier transition but amplitude-modulated at frequency μ

$$E_{\pm} = E_0 \cos((\omega_0 \pm \mu)t \pm \phi_d) \Rightarrow E_+ + E_- = 2E_0 \cos(\omega_0 t) \cos(\mu t + \phi_d). \quad (30)$$

In this case, the phase ϕ_d determines the initial amplitude of the field. Figure 5 depicts the gate operation for $\phi_d = 0$ and $\pi/2$ and shows the effect on the qubit state in Bloch sphere representation. The schematic shows that the state oscillates around its initial state when the gate operation starts with the maximal amplitude. However, when the gate operation starts with its minimal amplitude, the state oscillates around a slightly tilted state.

In [27], there is a detailed analysis on the off-resonant carrier term for any ϕ_d . Unfortunately, the analysis only deals with a single constant Rabi frequency which cannot be extended easily to our case. Therefore, we will consider the estimation of the infidelity in the next section by following [18] which only discusses the case $\phi_d = 0$.

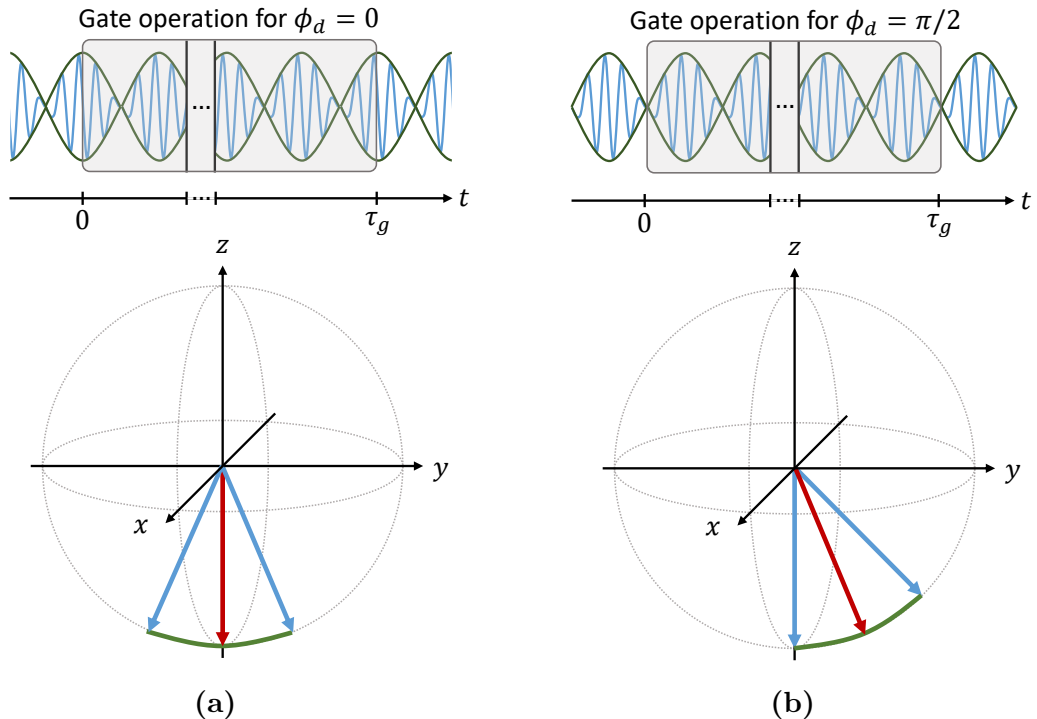


Figure 5: Gate operation as a function of the phase (a) $\phi_d = 0$ and (b) $\phi_d = \frac{\pi}{2}$ together with the state represented in the Bloch sphere. The grey box indicates the duration of the gate. Equation 30 is plotted qualitatively where the green envelope indicates $\cos(\mu t + \phi_d)$ and the blue fast oscillating term is $\cos(\omega_0 t)$. Note that the oscillation is not to scale, in reality, it would be much faster. The initial state (in red) oscillates between the two blue states as indicated by the green line. Adapted from [26].

In general, it is not easy to achieve $\phi_d \equiv \frac{1}{2}(\phi_r - \phi_b) = 0$. In the case of [20] which we broadly follow, the entangling gates are obtained by global and tightly focused beams, that have different beam paths. Therefore, it is not straightforward to achieve $\phi_d = 0$. Using the waveguide setup or other setups, where the laser beams propagate through exactly the same optical paths, it is, in principle, possible to set $\phi_d = 0$.

3.3.3. Fidelity loss due to off-resonant carrier excitation

We recall the full Hamiltonian without the limit of $\Omega \ll \mu$ from equation 16 and expand it to the situation of two ions being addressed by a laser beam

$$\begin{aligned} H_I &= \hbar\Omega \cos(\mu t) \sum_{s=1}^2 \left(\sigma_{y,s} + \sum_p [\eta(a^\dagger e^{i\omega_p t} + a e^{-i\omega_p t}) \sigma_{x,s}] \right) \\ &= H_C + H_{MS}. \end{aligned}$$

So far we have neglected the off-resonant carrier term (H_C) in the limit when $\Omega \ll \mu$. The influence of H_C in the fidelity needs to be estimated. We first reproduce the approach used in [18] and apply it then to our case. The idea is to change to the interaction picture of the Hamiltonian H_{MS} and treat the small deviations by perturbation theory.

For simplicity, we will start by considering a constant Rabi frequency $\Omega(t) \equiv \Omega$. The neglected term H_C corresponds to the coupling between the ground and excited state of the ion, but leaves the motion unaffected. The first step is to move to the interaction picture with respect to H_{MS} using the Dyson series

$$U_I(t) = 1 - \frac{i}{\hbar} \int_0^t dt' H_{C,I}(t') - \frac{1}{\hbar^2} \int_0^t \int_0^{t'} dt'' dt' H_{C,I}(t') H_{C,I}(t'') + \dots, \quad (31)$$

where $H_{C,I} = U(t)^\dagger H_C U(t)$ with $U(t)$ being the propagation operator for the Hamiltonian in the limit $\Omega \ll \mu$, i.e. for $H_I = H_{MS}$. As done in the paper, we consider the propagation operator to be constant in the integration because $H_C(t)$ is oscillating at a much higher frequency. Considering a detuning of around 3 MHz and a mode frequency of similar magnitude, the carrier term rotates with 3 MHz ($\Rightarrow \sim 300$ ns) in the interaction frame. Therefore, we conclude that this approximation is valid for gate times $\tau_g \gg 300$ ns.

The propagation operator in the interaction frame is then given by

$$\begin{aligned}
U_I(t) &= 1 - i\Omega \sum_{l=1}^2 U^\dagger \sigma_{y,l} U \int_0^t \cos(\mu t') dt' \\
&\quad - \Omega^2 \left(\sum_{l=1}^2 U^\dagger \sigma_{y,l} U \right)^2 \int_0^t \int_0^{t'} \cos(\mu t') \cos(\mu t'') dt'' dt' \\
&= 1 - i \frac{\Omega}{\mu} \sin(\mu t) U^\dagger \sum_{l=1}^2 \sigma_{y,l} U \\
&\quad - \frac{1}{2} \left(\frac{\Omega}{\mu} \right)^2 \sin(\mu t)^2 U^\dagger \left(\sum_{l=1}^2 \sigma_{y,l} \right)^2 U,
\end{aligned} \tag{32}$$

where we note that the expansion is up to second order of Ω/μ .

The goal is now to compute the fidelity $\mathcal{F} = |\langle \Psi_{\text{init}} | U_I(\tau_g) | \Psi_{\text{init}} \rangle|^2$ where $|\Psi_{\text{init}}\rangle$ denotes the initial state of the system in the interaction picture of the MS-Hamiltonian. In the ideal case, the off-resonant drive of the carrier is zero and therefore, the initial state in the MS interaction picture will not evolve. However, since the off-resonant carrier drive is not zero, the initial state does evolve and the fidelity is reduced.

We will prepare some calculations to simplify the fidelity calculation.

$$\begin{aligned}
|\Psi_{\text{init}}\rangle &= |00\rangle = \frac{|++\rangle + |+-\rangle + |-+\rangle + |--\rangle}{2} \\
|\Psi'\rangle &:= U(\tau_g) |\Psi_{\text{init}}\rangle = \frac{1}{2} [e^{i\frac{\pi}{4}} \{ |++\rangle + |--\rangle \} + e^{-i\frac{\pi}{4}} \{ |+-\rangle + |-+\rangle \}] \\
&= \frac{1}{2} e^{i\frac{\pi}{4}} [\{ |++\rangle + |--\rangle \} - i \{ |+-\rangle + |-+\rangle \}]
\end{aligned} \tag{33}$$

Next we take into account the σ_y 's to find

$$\begin{aligned}
\sigma_y |+\rangle &= \frac{1}{\sqrt{2}} \begin{pmatrix} 0 & -i \\ i & 0 \end{pmatrix} \begin{pmatrix} 1 \\ 1 \end{pmatrix} = \frac{i}{\sqrt{2}} \begin{pmatrix} -1 \\ 1 \end{pmatrix} = i |-\rangle, \quad \sigma_y |-\rangle = -i |+\rangle \\
\sigma_{y,1} |\Psi'\rangle &= \frac{1}{2} e^{i\frac{\pi}{4}} \{ |--\rangle - |++\rangle - |-+\rangle + |+-\rangle \}, \\
\sigma_{y,2} |\Psi'\rangle &= \frac{1}{2} e^{i\frac{\pi}{4}} \{ |--\rangle - |++\rangle + |-+\rangle - |+-\rangle \}
\end{aligned}$$

This we can apply to the two cases that we have in the Dyson expansion and get

$$\begin{aligned}
|Y\Psi'\rangle &:= \sum_{l=0}^2 \sigma_{y,l} |\Psi'\rangle = e^{i\frac{\pi}{4}} (|--\rangle - |++\rangle) \\
|Y^2\Psi'\rangle &:= \left(\sum_{l=0}^2 \sigma_{y,l} \right)^2 |\Psi'\rangle = -2ie^{i\frac{\pi}{4}} (|+-\rangle + |-+\rangle)
\end{aligned}$$

Now we have all the terms needed for the fidelity computation. Near the point of the optimal gate $U(\tau_g) \approx e^{i\frac{\pi}{4}\sigma_{x,a}\sigma_{x,b}}$ we find

$$\begin{aligned} \langle \Psi_{\text{init}} | U_I(\tau_g) | \Psi_{\text{init}} \rangle &= \underbrace{\langle \Psi_{\text{init}} | \Psi_{\text{init}} \rangle}_{=1} - i \frac{\Omega}{\mu} \sin(\mu\tau) \underbrace{\langle \Psi' | Y \Psi' \rangle}_{=0} \\ &\quad - \frac{1}{4} \left(\frac{\Omega}{\mu} \right)^2 (1 - \cos(2\mu\tau_g)) \underbrace{\langle \Psi' | Y^2 \Psi' \rangle}_{=ie^{-i\frac{\pi}{4}}(-2i)e^{i\frac{\pi}{4}}=2} \\ &= 1 - \frac{1}{2} \left(\frac{\Omega}{\mu} \right)^2 (1 - \cos(2\mu\tau_g)) \end{aligned} \quad (34)$$

which leads to a fidelity up to $\mathcal{O}\left(\left[\frac{\Omega}{\mu}\right]^2\right)$

$$\begin{aligned} \mathcal{F}_{\text{off-resonant}} &= |\langle \Psi_{\text{init}} | U_I(\tau_g) | \Psi_{\text{init}} \rangle|^2 = \left[1 - \frac{1}{2} \left(\frac{\Omega}{\mu} \right)^2 (1 - \cos(2\delta\tau_g)) \right]^2 \\ &\approx 1 - \left(\frac{\Omega}{\mu} \right)^2 (1 - \cos(2\mu\tau_g)). \end{aligned} \quad (35)$$

This result indicates that the detuning μ and gate time τ_g should not be considered as individual parameters. If one parameter is fixed, then we can optimize the other such that we minimize the infidelity caused by the off-resonant carrier excitation.

We will implement the gate with different levels of Rabi frequencies in section 4. We need to adapt the fidelity calculation according to the time-dependent Rabi frequency. The procedure is the same with the exception that in the Dyson series we actually also integrate over the Rabi frequency $\Omega(t)$. The computations considering the initial and other states as well as any follow-up computations, however, stay the same. Therefore, we end up with an approximate fidelity of

$$\mathcal{F}_{\text{off-resonant}} \approx 1 - 4 \int_0^{\tau_g} \int_0^{t'} \Omega(t') \Omega(t'') \cos(\mu t') \cos(\mu t'') dt'' dt'. \quad (36)$$

It is not straightforward to interpret this formula in the same way as for a constant Rabi frequency. However, since the essential physics has not changed, we expect that the detuning μ can be optimized as a function of the gate time τ_g or vice versa.

4. Simulation of two-ion entanglement in a linear five-ion chain

The planned experimental setup is schematically shown in figure 6. It indicates the tools that we have to implement for performing the entangling gate in the experiment. We use a 729 nm laser to drive the qubit transition. The laser's frequency, phase and amplitude is adjusted with an AOM. The specifications of the AOM are discussed in section 5. Afterwards the shaped light is directed towards the trapped ions. The interaction of the electric field of the laser light and the ion implements the entangling gate as shown in the previous section. The requirements of the laser beam to entangle the ions are determined in the following sections.

Based on the theory of the previous section, the next step is to calculate the optimal pulse sequence in order to entangle any pair within a linear ion chain of five ions. The goal is to implement an MS gate by an amplitude-modulated laser, similar to [20]. Other possibilities include frequency modulation [28] and phase modulaton [29] or both [30]. There is also recent work implementing two simultaneous [31] or a global MS gate [29].

The amplitude-modulated laser leads to a time-dependent Rabi frequency. In this approach, we will send the same laser pulse to both ions. The Rabi frequency $\Omega_s = \Omega = \Omega(t)$ is described by

$$\Omega(t) = \begin{cases} \Omega_0, & 0 < t \leq \frac{\tau_g}{P} \\ \Omega_1, & \frac{\tau_g}{P} < t \leq \frac{2\tau_g}{P} \\ \dots \\ \Omega_{P-1}, & \frac{(P-1)\tau_g}{P} < t \leq \tau_g, \end{cases} \quad (37)$$

where P denotes the number of segments. How to choose the number of segments is discussed in the following. Any considerations made along with the implementation of the simulation are outlined. The results are presented for different gate times.

4.1. The underlying optimization problem

In the simulation the optimal pulses for the entanglement of any pair of ions in the linear ion chain is computed. The effect of these pulses is precisely described by the propagation operator (equation 22), where we now pick $\phi_d = 0$ based on the considerations in

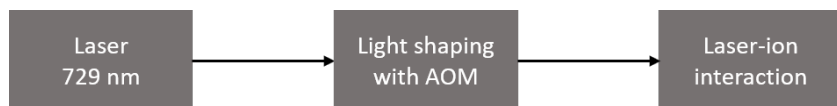


Figure 6: Schematic drawing of the planned experimental setup.

section 3.3.2 and get

$$\begin{aligned}
U(t) &= \exp \left(\sum_k \xi_k(t) \sigma_{x,k} + i \sum_{\substack{k,l \\ k < l}} \chi_{k,l} \sigma_{x,k} \sigma_{x,l} \right), \text{ where} \\
\xi_k(t) &= \sum_p [\alpha_{k,p}(t) a_p^\dagger - \alpha_{k,p}^*(t) a_p], \\
\alpha_{k,p} &= i \eta_{k,p} \int_0^t \Omega_k(t') \cos(\mu t') e^{i\omega_p t'} dt' \\
\chi_{k,l} &= 2 \sum_p \eta_{k,p} \eta_{l,p} \int_0^t \int_0^{t'} \Omega_k(t') \Omega_l(t'') \cos(\mu t') \cos(\mu t'') \sin[(\omega_p - \mu)(t' - t'')] dt'' dt'.
\end{aligned} \tag{38}$$

The displacement in phasespace of the p -th mode is described by $\alpha_{s,p}(t)$ and the spin-spin interaction of ions k and l is given by $\chi_{k,l}(t)$.

As discussed in section 3.2.2, the optimal gate is given by $U(\tau_g) = e^{i\frac{\pi}{4}\sigma_{x,k}\sigma_{x,l}}$. Therefore, the requirements on the Rabi frequencies Ω_k are given by

$$\begin{aligned}
\alpha_{k,p}(\tau_g) &= 0 \quad \forall k, p, \\
\chi_{k,l}(\tau_g) &= \frac{\pi}{4} \text{ for entangling ion } k \text{ and } l.
\end{aligned} \tag{39}$$

A naive estimation of the number of required degrees of freedom to satisfy these constraints is given by the following analysis. If N is the number of ions, there are $2N$ constraints for $\alpha_{k,p}$ considering the real and imaginary parts with respect to the N closest normal modes. For a slow gate, it is sufficient to consider only the N normal modes close to the laser detuning. Due to larger detuning from the laser as well as the relatively low laser intensity used in slow gates, the other $2N$ modes are not highly excited and thus will not contribute much to the overall gate infidelity. In addition to these constraints, we need to satisfy the condition for $\chi_{k,l}$. This indicates that these constraints can be satisfied by $2N + 1$ different evenly partitioned levels for the entangling pulse [20]. In the case of $N = 5$, we expect that the constraints are satisfied by 11 different levels. Taking a closer look, we notice that the last constraint can be automatically satisfied by appropriate normalization of the Rabi frequency Ω . Equally, the $\alpha_{k,p}$ parameters have less conditions because the real and imaginary parts are not independent, leaving us with a total amount of conditions to be 5 [17].

That number of Rabi frequency levels is used as a first approach, where we use a symmetric pulse by repeating the first four levels in a mirrored way. This number takes only the closest five normal modes into account which are the radial normal modes in z -direction in this specific case. Therefore, the amount of levels may not be sufficient to close all loops in phasespace for all normal modes. Five levels, in fact, reduce the fidelity significantly for faster gates. The number of levels are picked to be higher than five to reach a better fidelity in some cases. In principle, the laser detuning can also be varied in different segments of the pulse sequence. Within this optimization, the laser

frequency and therefore, μ , is fixed. As discussed in section 3.3.3, the gate time τ_g and the detuning μ of the laser can be considered as two interdependent parameters. Including both leads to unsatisfying results, likely because too many parameters are given for the optimization. Therefore, we fix a gate time and include the detuning in the optimization process. We first set the gate time to be $\tau_g = 100 \text{ }\mu\text{s}$. This time is further reduced as discussed in section 4.3.2.

If we use enough Rabi frequency levels, an analytical solution satisfying the constraints in equation 39 is possible. However, the fidelity for different solutions may be different, especially when the Rabi frequency levels are normalized [17]. Taking the off-resonant carrier drive into account, analytical solutions become more difficult. Based on these considerations, I implemented a numerical optimization. Before the optimization, the Rabi frequency levels are normalized with respect to $\chi_{k,l}(\tau_g)$. Then the code minimizes the function

$$f = \sum_{k,p} |\alpha_{k,p}(\tau_g)|^2 + (1 - \mathcal{F}_{\text{off-resonant}}), \quad (40)$$

which is consistent with the conditions given in equation 39 and includes the off-resonant carrier term infidelity as given in equation 36.

For the optimization process as well as fidelity calculations the Lamb Dicke parameter has to be known, although the pulse sequence will mainly drive the radial modes along the z-direction, i.e. perpendicular to the trap surface. The projections of the laser beam are considered in our design along all dimensions.

The optimization is implemented using *MATLAB*. A bounded version of the function *fminsearch* is used which allows setting upper and lower limits of the optimization parameters. This helps us to reduce the overall power by bounding the detuning μ in the vicinity of the motional modes in z-direction. This reduces the total laser power needed to implement the gate. The function uses the Nelder-Mead algorithm to find an optimal solution.

4.2. Numerical considerations

The integrals in equation 38 were initially computed numerically. The numerical integration method *integral* of *MATLAB* produces unreliable results, and in the case of *trapz* is highly dependent on the number of sampling points. The highly oscillating character of the functions is likely to lead to that issue. Therefore, the integrals were transformed into expressions that are integrated analytically by following the approaches in [17, 23].

We recall the time dependency of the Rabi frequency $\Omega_s = \Omega = \Omega(t)$ as given in equation 37, where the Rabi frequency consists of P evenly divided segments. The

easiest case is the analytical expression of $\alpha_{k,p}$ in the propagation operator

$$\begin{aligned}
\alpha_{k,p} &= i\eta_{k,p} \int_0^t \Omega(t') \cos(\mu t') e^{i\omega_p t'} dt' \\
&= i\eta_{k,p} \sum_{s=0}^{P-1} \Omega_s \int_{t_s}^{t_{s+1}} \cos(\mu t') e^{i\omega_p t'} dt' \\
&= i\eta_{k,p} \sum_{s=0}^{P-1} \frac{\Omega_s}{\mu^2 - \omega_p^2} \left[e^{i\omega_p t_{s+1}} (\mu \sin(\mu t_{s+1}) + i\omega_p \cos(\mu t_{s+1})) \right. \\
&\quad \left. - e^{i\omega_p t_s} (\mu \sin(\mu t_s) + i\omega_p \cos(\mu t_s)) \right],
\end{aligned} \tag{41}$$

where $t_s = \frac{s \cdot \tau_g}{P}$ segments the gate time into P equally distributed segments for $s = 0, \dots, P-1$.

It gets more complicated when the Rabi frequency appears twice in the integration and depends on a different variable. A similar approach solves this problem, for example, the analytical expression of $\chi_{k,l}$ is given by

$$\begin{aligned}
\chi_{k,l} &= \sum_p \eta_{k,p} \eta_{l,p} \int_0^{\tau_g} \int_0^t \Omega(t) \Omega(t') \cos(\mu t) \cos(\mu t') \sin[(\omega_p - \mu)(t - t')] dt' dt \\
&\propto \int_0^{\tau_g} \int_0^t \Omega(t) \Omega(t') \cos(\mu t) \cos(\mu t') \sin[(\omega_p - \mu)(t - t')] dt' dt \\
&= \sum_{s=0}^{P-1} \sum_{\substack{s'=0 \\ s' \leq s}}^{P-1} \Omega_s \Omega_{s'} \int_{t_s}^{t_{s+1}} \int_{t_{s'}}^{t_{s'+1}} \cos(\mu t) \cos(\mu t') \sin[(\omega_p - \mu)(t - t')] dt' dt \\
&= \sum_{s=0}^{P-1} \sum_{\substack{s'=0 \\ s' \leq s}}^{P-1} \Omega_s \Omega_{s'} D_{s,s'}.
\end{aligned} \tag{42}$$

The integral $D_{s,s'}$ is computed analytically similar to the previous case. Summing over the condition $s' \leq s$ ensures that for any time we satisfy the limits that are given in the original integral. However, for the case $s = s'$ we have to be careful to satisfy $t' \leq t$ and find

$$D_{s,s} = \int_{t_s}^{t_{s+1}} \int_{t_s}^t \cos(\mu t) \cos(\mu t') \sin[(\omega_p - \mu)(t - t')] dt' dt. \tag{43}$$

This method can be and is applied for other cases, for instance, to compute the fidelity with respect to the off-resonant carrier term as given in section 3.3.3.

4.3. Results

The frequency of the axial normal modes $\omega_{x,n} = \sqrt{\psi_{x,n}} \omega_x$ is specified by the frequency ω_x as described in section 3.1 which determines the displacements between the individual

ions. The directions of the laser beams that leave the grating are designed according to a base axial frequency of $\omega_x = 2\pi \times 422$ kHz which results in a spacing of 6.5 μm between the inner ions and 7.3 μm for the outer ions, respectively.

The most important modes are the radial normal modes in z -direction which are used entangle two ions. In the following optimization, the parameters were chosen as $\omega_z = 2\pi \times 3.5$ MHz, an experimentally feasible radial frequency satisfying $\omega_z \sim 10 \cdot \omega_x$. The frequencies are obtained in a similar way by $\omega_{z,n} = \sqrt{\zeta_{z,n}}\omega_z$. According to previous experiments in the lab, I have chosen $\omega_y = 0.8 \cdot \omega_z$ as the frequency in the y -direction. Normal modes in different directions incorporate a different Lamb-Dicke parameter. Using the usual representation in spherical coordinates where a vector of unit length is described by $\vec{r} = (\cos(\varphi) \sin(\theta), \sin(\varphi) \sin(\theta), \cos(\theta))^T$, we define the angles φ and θ for the beams that leave the structure through the grating couplers of the chip design in figure 1. The angle with respect to the z -direction is designed the same for each ion as $\theta_{\text{ion}} \equiv \theta = 36^\circ$. The other angles were designed as $\varphi = [235^\circ, 110^\circ, 270^\circ, 70^\circ, 305^\circ]$ because the beams are tilted by $\pm 20^\circ$ and $\pm 35^\circ$ with respect to the y -direction.

For a symmetrical five-ion chain, there are only six different ion pairs that need different Rabi pulses: (1,2), (1,3), (1,4), (1,5), (2,3) and (2,4), where we labelled the ions from left to right. Any other pair can be entangled using one of those six sequences by simply relabelling the ions. Initially the contribution of only the radial modes in z -direction was taken into account for χ . However, since we also take the other modes into account for the fidelity calculations, it only makes sense to add them to the calculation of χ . We observe that the main contribution comes from the closest modes, as expected. The absolute magnitudes of the Rabi frequency as initial guess is not very important because they will be normalized. The initial guess for the detuning is more significant because the optimization is looking for a solution in the vicinity of the initial value and therefore, produces good or bad solutions depending on the initial guess.

This section covers the optimal pulse shapes obtained by the code. We have choosen four different gate times $\tau_g = 100$ μs , 80 μs , 60 μs and 40 μs . The obtained Rabi frequency sequences to entangle any pair within the linear ion chain of five ions are presented.

4.3.1. Individual optimal pulse shapes for a gate time of $\tau_g = 100$ μs

To get a rough idea of a good initial value for the detuning, we take a look at the structure of the modes which we would like to mainly drive as shown in figure 3. On the ions that should be entangled, a large projection of the mode is necessary, leading to a large projection for certain laser intensity.

Let's consider ions 1 and 2 as an example. The projection on ion 1 from the 4th and 5th modes is minor. For ion 2 the projections from all modes are similar. Therefore, the optimal detuning is likely located between the tilt mode and the third mode. Looking at the formula for χ , we can define $\chi = \sum_k \chi^{(k)}$ with $\chi^{(k)} \propto \eta_{1,k} \cdot \eta_{2,k}$, where k is the

index for the normal modes. Since for one mode the detuning is red and for the other blue, it makes sense that the product $\eta_{1,k} \cdot \eta_{2,k}$ also has a sign change for the two modes that are closest to the detuning such that they work towards the same result. Following this approach explicitly, we have $\eta_{1,2} \cdot \eta_{2,2} > 0$ and $\eta_{1,3} \cdot \eta_{2,3} < 0$ for ion 1 and 2. When the optimal detuning is between the tilt mode with frequency ω_2 and the third mode with frequency ω_3 , the difference of $\mu - \omega_2$ has a different sign compared to $\mu - \omega_3$, so $\chi^{(2)}$ has the same sign as $\chi^{(3)}$. Applying the same analysis to other ion pairs, we would expect all detunings to be naturally between the second and the third or the fourth and the fifth mode.

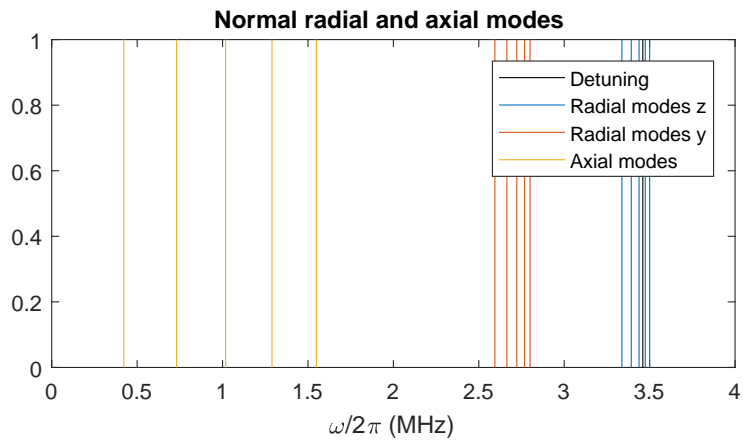
The exact value of the detuning is primarily determined by the infidelity of the off-resonant carrier term. All ion pair entanglements can be analyzed in this way. If ion 3 is involved, this intuitive analysis is not straightforward, because for any detuning one of the closest modes to the detuning will have zero displacement. There the magnitude of the displacement plays a more important role.

The optimal solutions for all ion pairs are summarized in table 1. As an example, the optimal solution for ion 1 and 2 is shown in figure 7. The infidelity is calculated as 1.9×10^{-5} considering all 15 normal modes for the optimization as well as the infidelity due to the off-resonant carrier excitation (equation 40). As motivated above, the value of detuning $\mu = 2\pi \times 3.4602$ MHz is indeed between the tilt and third mode frequency. We observe that the shape of the Rabi frequency gradually increases until a maximal value of $\Omega \sim 2\pi \times 300$ MHz. The corresponding phasespace diagram is depicted in figure 7. We observe that the modes that are closer to the laser detuning experience a higher excitation. As desired, the phasespace trajectories close at the end of the gate. All Rabi frequency pulses and the corresponding phasespace diagrams can be found in appendix A.

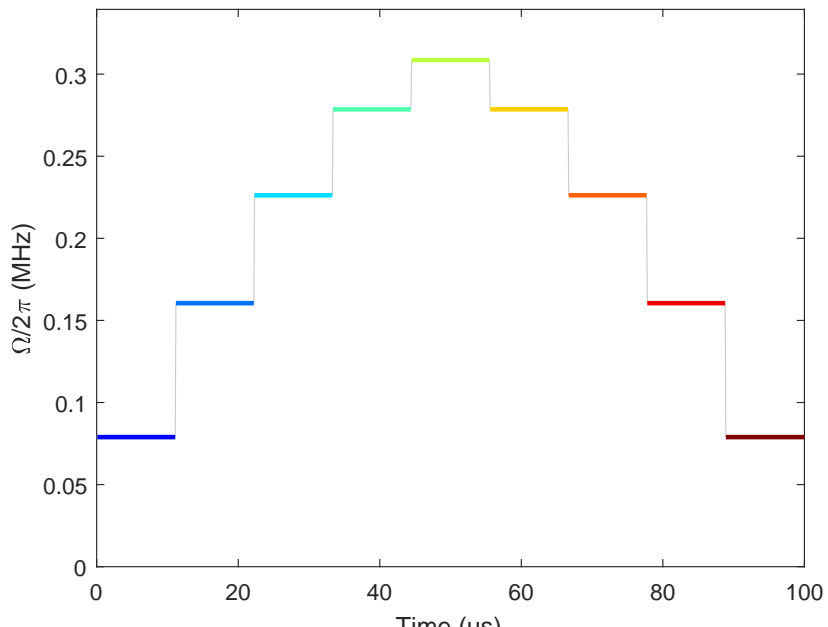
We also assumed the mean phonon number $\bar{n} = 0$ for all modes. Increasing the mean phonon number to $\bar{n} = 0.1$ (0.2, 1) raises the infidelity by a factor of ~ 1.2 (1.4, 3) for the same pulse sequence. Values of $\bar{n} \ll 1$ are achieved by EIT cooling [32] which indicates that the fidelity is not limited by this. We obtain similar infidelities with

Table 1: Optimal solution for a gate time of $\tau_g = 100$ μ s for all ion pairs including optimal detuning and the corresponding infidelity.

Ion pair	Optimal detuning	Infidelity
(1, 2)	3.4602 MHz	1.9×10^{-5}
(1, 3)	3.4600 MHz	1.8×10^{-5}
(1, 4)	3.3702 MHz	4.2×10^{-5}
(1, 5)	3.4550 MHz	4.2×10^{-5}
(2, 3)	3.3702 MHz	1.8×10^{-5}
(2, 4)	3.3612 MHz	3.7×10^{-5}



(a)



(b)

Figure 7: Optimal solution for $\tau_g = 100 \mu\text{s}$ for entangling ion 1 and 2. (a) Frequencies of the normal modes and detuning of the applied laser beam. (b) Optimal pulse sequence showing the different Rabi frequency levels. The infidelity of this solution is calculated to be $1.9 \cdot 10^{-5}$.

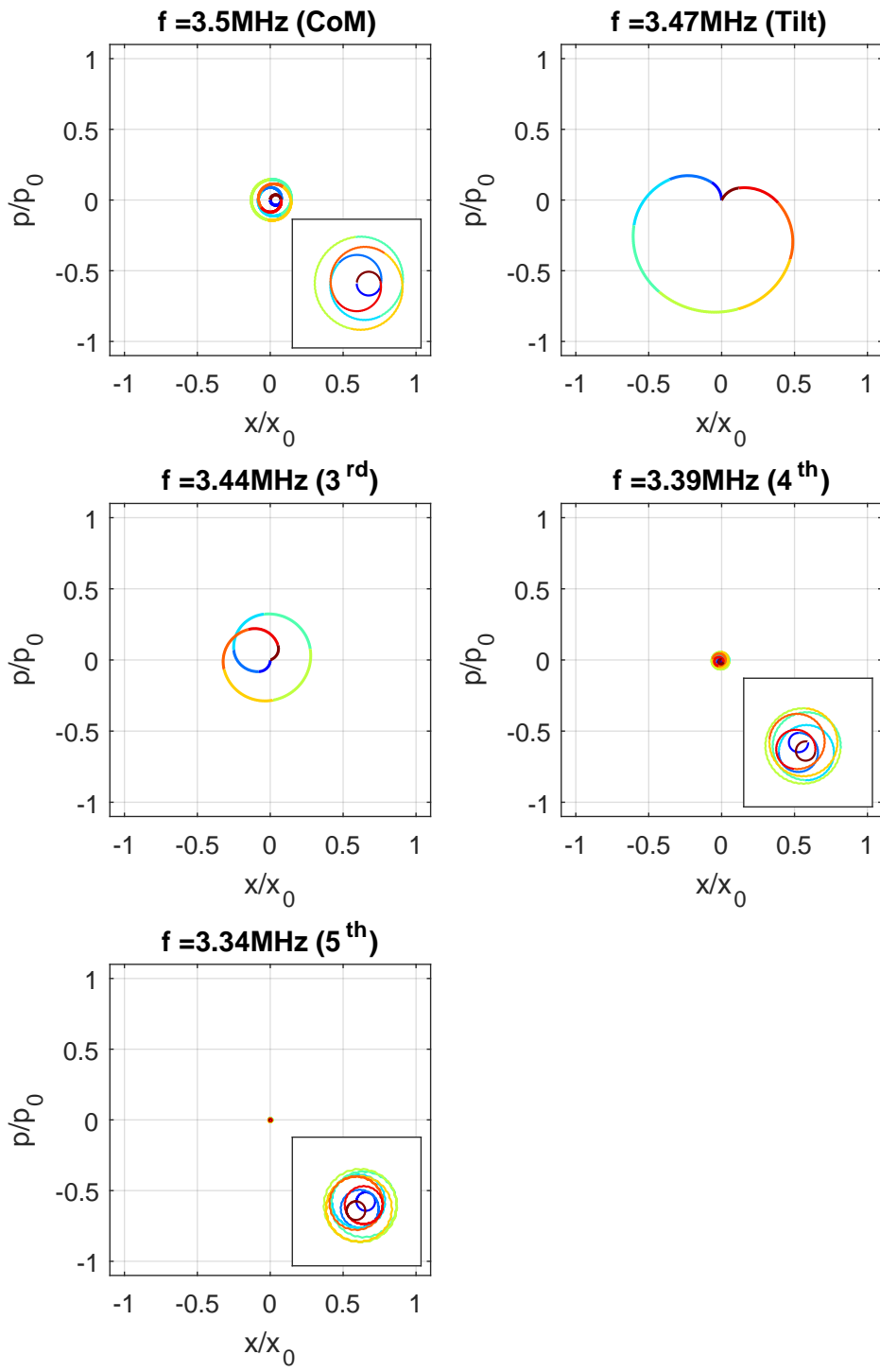


Figure 8: Phasespace diagrams of the normal modes in z -direction. The color code corresponds to the Rabi levels as in figure 7. For each solution, there are different Rabi frequency levels.

different detunings, Rabi frequency levels and therefore, phasespace diagrams.

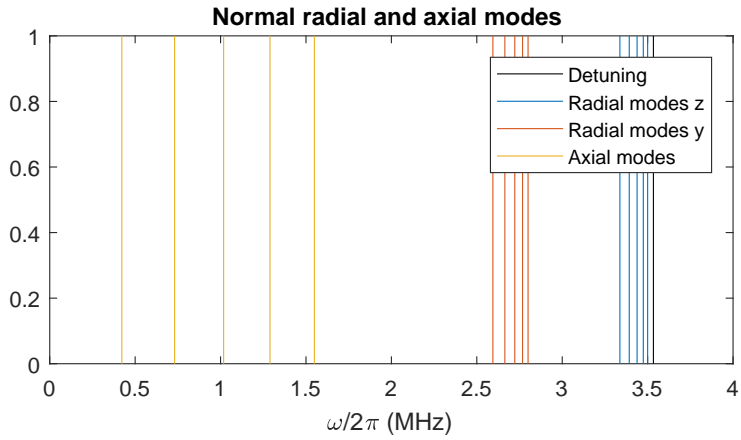
4.3.2. Individual optimal pulse shapes for faster gates

I have simulated the same gate for shorter gate times, namely 80 μs , 60 μs and 40 μs . For the faster gate times, we are approaching the limit where the approximations done in section 3.3.3 hold. The optimal solutions are summarized in table 2 for $\tau_g = 80 \mu\text{s}$. We observe that the detuning of the laser is very similar for each ion pair. The reason behind this is probably the minimization of the infidelity caused by the off-resonant carrier drive which is highly frequency dependent. Changing the initial detuning for the optimization produced worse solutions in terms of infidelity. Whereas for 80 μs we achieve good fidelity with only five different levels, we need to add more levels for shorter gate times.

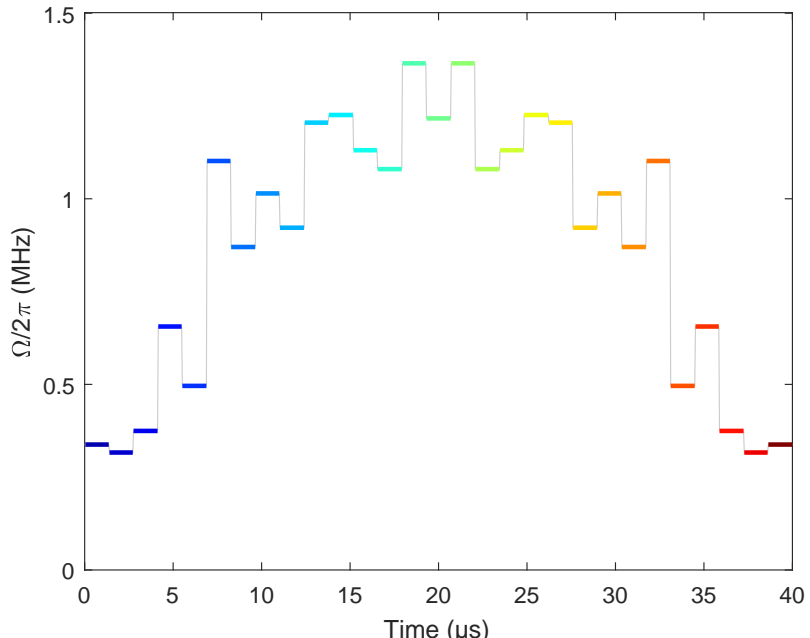
For the simulation of 60 μs and 40 μs , we choose 15 different Rabi frequency levels. This is necessary because a higher laser intensity makes the other 10 motional modes more excited, thus for good gate fidelity, we achieve closing their phasespace loops by introducing more degrees of freedom to the optimization. Since each mode whose phasespace loop needs to be closed requires one degree of freedom to satisfy its constraint on α_p , we pick 10 more levels. The optimal solution for gate times $\tau_g = 60 \mu\text{s}$ and 40 μs are shown in table 3. For a gate time of $\tau_g = 60 \mu\text{s}$ we find that all Rabi frequency levels are below $2\pi \times 1 \text{ MHz}$. For the case of $\tau_g = 40 \mu\text{s}$, the Rabi frequency levels are in most cases below $2\pi \times 1.5 \text{ MHz}$, but reach in some cases values around $2\pi \times 2 \text{ MHz}$. We can observe that for example for ion 1 and 3, where the optimal solution for a gate time of $\tau_g = 40 \mu\text{s}$ is shown in figures 9 and 10. As compared to the case of 100 μs , where the Rabi frequency levels rise step by step until they reach a maximal value and then are by design mirrored, we note that for the faster gates with more Rabi frequency levels this is not the case. A potential explanation is that we reach the limits of the optimization because the 15 different Rabi frequency levels bring along a solution space with more dimensions and the optimization may be

Table 2: Optimal solution for a gate time of $\tau_g = 80 \mu\text{s}$ for all ion pairs including optimal detuning and the corresponding infidelity. For each solution, there are five different Rabi frequency levels.

Ion pair	Optimal detuning	Infidelity
(1, 2)	3.4126 MHz	5.3×10^{-5}
(1, 3)	3.4126 MHz	7.9×10^{-5}
(1, 4)	3.4126 MHz	3.2×10^{-5}
(1, 5)	3.4129 MHz	5.0×10^{-5}
(2, 3)	3.4126 MHz	5.0×10^{-5}
(2, 4)	3.4126 MHz	1.7×10^{-5}



(a)



(b)

Figure 9: Optimal solution for $\tau_g = 40 \mu\text{s}$ for entangling ion 1 and 3. (a) Frequencies of the normal modes and detuning of the applied laser beam. (b) Optimal pulse sequence showing the different Rabi frequency levels.

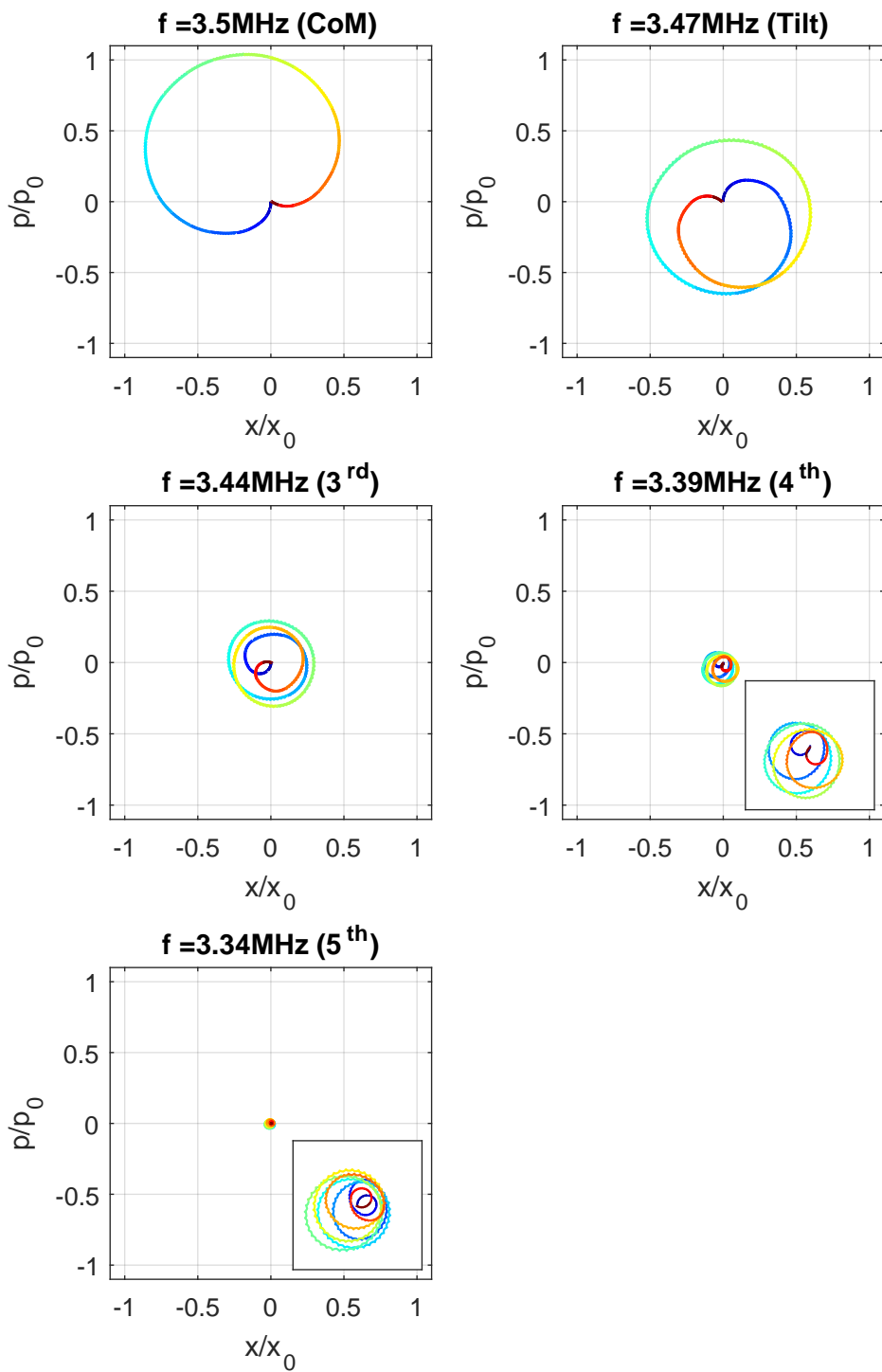


Figure 10: Phasespace diagrams of the normal modes in z -direction. The color code corresponds to the Rabi levels as in figure 9.

Table 3: Optimal solution for a gate time of $\tau_g = 60 \mu\text{s}$ and $\tau_g = 40 \mu\text{s}$ for all ion pairs including optimal detuning and the corresponding infidelity. For each solution, there are 15 different Rabi frequency levels.

Ion pair	Gate time	Optimal detuning	Infidelity
(1, 2)	60 μs	3.4153 MHz	2.3×10^{-5}
(1, 3)	60 μs	3.4153 MHz	4.9×10^{-6}
(1, 4)	60 μs	3.4153 MHz	1.0×10^{-5}
(1, 5)	60 μs	3.4153 MHz	5.5×10^{-6}
(2, 3)	60 μs	3.4153 MHz	4.7×10^{-5}
(2, 4)	60 μs	3.4153 MHz	2.0×10^{-5}
(1, 2)	40 μs	3.5375 MHz	4.6×10^{-4}
(1, 3)	40 μs	3.5336 MHz	7.3×10^{-4}
(1, 4)	40 μs	3.5315 MHz	6.3×10^{-4}
(1, 5)	40 μs	3.3649 MHz	5.6×10^{-4}
(2, 3)	40 μs	3.3650 MHz	3.4×10^{-4}
(2, 4)	40 μs	3.3649 MHz	1.1×10^{-4}

trapped at a local minimum. The increase of the Rabi frequency levels explains the larger phasespace that is moved through during the gate as observed in figure 10.

For the faster gates, the limit $\Omega \ll \mu$, the time considerations and the approximations for the computation of off-resonant carrier excitation do no longer hold and therefore, equation 36 is not strictly valid. An expansion of the Dyson series to $\mathcal{O}([\Omega/\mu]^5)$ indicates that the infidelity does not change much from the results quoted in tables 1, 2 and 3. In fact, we observe that the infidelity contribution of the off-resonant carrier infidelity is $\leq 10^{-7}$. Therefore, it is recommended to simulate the full Hamiltonian using the von-Neumann equation $-i\hbar\rho = [H, \rho]$ while neglecting the thermal state which is not part of the off-resonant carrier term to reduce simulation complexity. This simulation will become necessary to estimate the infidelity for faster gates. It was not conducted within the thesis due to time limitations.

Given the reduced fidelity for $\tau_g = 40 \mu\text{s}$ which does not yet take into account any experimental effects, we did not perform any simulation beyond that time. To achieve faster gates, we probably have to go for a different scheme, like positioning the ions to the nodes of a standing wave to suppress the off-resonant excitation of the carrier transition [8].

We have implemented a method that allows to compute the optimal pulse sequence for the implementation of an entangling gate for two ions within a linear chain of N ions. The number of Rabi frequency levels as well as the gate time can be set by the user. We have shown the examples of the computed optimal pulse shapes for different

gate times. For gate times $\tau_g = 100 \mu\text{s}$ and $80 \mu\text{s}$ it is sufficient to segment the Rabi frequency into five different levels in order to obtain infidelities $< 10^{-4}$. For faster gates it is necessary to implement more segments because the necessary Rabi levels are higher and with increased optical power, all the normal modes are more excited during the gate. Nevertheless, the fidelities are not as good, likely, because the solution space of the optimization increases by 10 dimensions.

5. Fiber-coupled AOM characterization

The implementation of the entangling gates in the previous section requires adjustments of the laser amplitude, frequency and phase. We plan to use an AOM to pulse the beams and connect their output to waveguides in the chip trap. We will examine the specifications given by the manufacturer and further investigate the AOM device with respect to its response time and power drifts. An imperfect experimental implementation of the optimized pulse sequence is a potential source of infidelity. Characterizing the AOM response allows us to bound this infidelity, and also to improve the experimental gate fidelity by compensating the imperfect implementations in the pulse sequence design.

Typically, double pass AOMs are used for shifting the laser frequency by orders of 100 MHz and for adjusting the amplitude or the phase of the laser beam. The optical setup for these double pass AOMs is quite space consuming. Moving towards more ions that will all need to be individually addressed, the amount of double pass AOMs and thus, required space for the setup, increases linearly. In terms of scalability, many more ions will be trapped which all need an individual AOM, but eventually lab space would be the limit in terms of the scale of trapped-ion quantum computer. A possible way to go around this is the use of fiber-coupled AOMs where a fiber takes the light to the AOM device and subsequently, is collected by another piece of fiber.

In this section the working principle of an AOM is explained. Then the measurement setup and the characterization of the fiber-coupled AOM are discussed. The characterization includes optical efficiency for different AOM drive frequencies as well as timing details when using the device for pulse-shaping.

5.1. Working principle of an AOM

The underlying principle of an AOM is based on the acousto-optic effect [33]. Driving the piezo-electric transducer with an RF signal ω_{RF} generates a traveling acoustic wave inside the AOM crystal. The acousto-optic effect leads to a periodic modulation of the refractive index and light travelling through this moving grating-like structure experiences Bragg diffraction. Due to the movement of the grating, the n -th order diffracted beam experiences a frequency shift of $\pm n \cdot \omega_{RF}$. The working principle is depicted in figure 11. The amplitude of the applied signal determines the power of the diffracted beam. We are usually interested in the diffracted beam of order ± 1 and optimize the AOM for them. As a summary, an AOM can control the optical power, frequency, phase and propagation direction of a laser beam by application of the corresponding RF signal.

A well-aligned AOM typically reaches a single-pass efficiency of up to 80%, where the efficiency is defined as the ratio of the optical output power in the desired order and the optical input power.

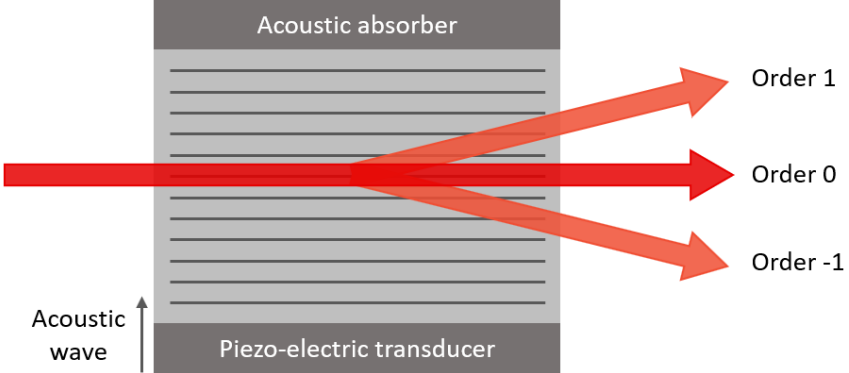


Figure 11: Schematic of the working principle of an AOM. The piezo-electric transducer generates the acoustic wave which works as a grating for the incident beam. This can be diffracted as indicated by the lighter beams which indicates the reduced optical power of the diffracted beams. Adapted from [33].

5.2. Fiber-coupled AOM

The fiber-coupled AOM that is characterized is a 780 nm Fibre-Coupled Acousto-Optic Modulator called Fibre-Q which is manufactured by Gooch & Housego (T-M150-0.5C2W-3-F2S/ T-M150-0.5C2W-3-F2P). The crystal inside the device is optimized for a laser wavelength of 729 nm. The device in this case is optimized for a first order shift where the frequency of the laser beam is increased. The manufacturer can in principle configure it to down-shift the laser frequency by optimizing for the diffraction of order -1. However, the configuration cannot be adjusted by the user once this device is manufactured. The fiber attached to the AOM is a Nufern 780-HP single mode fiber [34]. All specifications of the fiber-coupled AOM are given in [35].

5.3. Measurement setup

For the characterization of the fiber-coupled AOM we use a laser with a wavelength of 729 nm. Before the fiber-coupled AOM, our optical setup incorporates a double pass AOM. For the characterization itself, the double pass AOM was turned off. A double pass AOM features a larger frequency bandwidth, because the laser beam passes through the device twice. It is typically used to adjust the overall laser frequency at the beginning. Since it is not used during the characterization, it will not be described any further. The setup used is depicted in figure 12.

At the beginning of this setup, there is a polarizing beamsplitter (PBS) which is used to share the laser light with another setup. After that we use a pick-off mirror which together with a diode (PDA36A-EC by Thorlabs) allows us to monitor the total optical power and observe potential power and/or polarization drifts due to the PBS at the beginning. Before the fiber-coupled AOM, there are two mirrors (in a 45° position) which

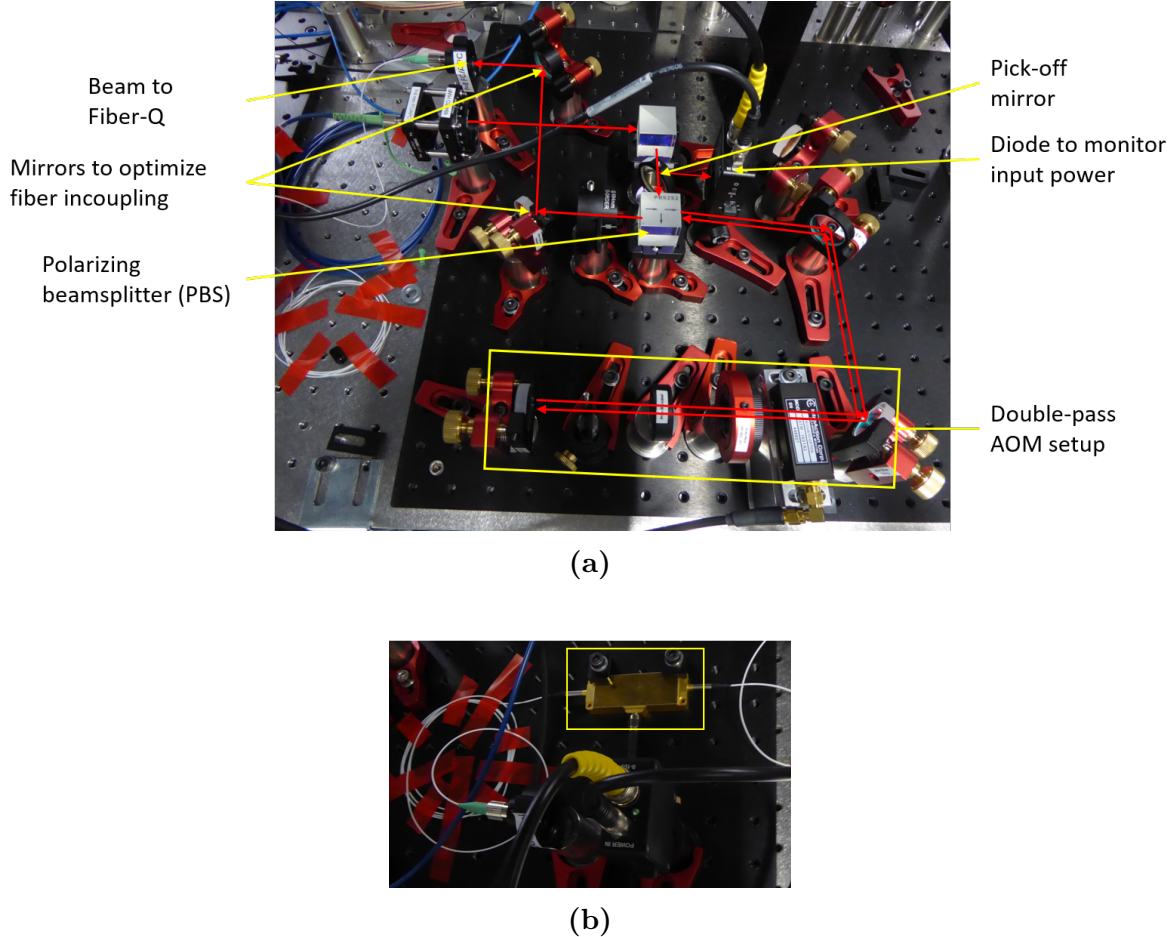


Figure 12: Setup for fiber-coupled AOM characterization. (a) As indicated by the red arrows, the incident laser beam is first split with a polarizing beamsplitter (PBS), then it is directed towards the double-pass AOM setup and is finally coupled into the fiber that is attached to the fiber-coupled AOM. (b) Fiber-coupled AOM (indicated by the yellow box) where the incident laser beam is diffracted and coupled into the second fiber. The light is then collected in a diode.

are used to optimize the coupling into the fiber. The AOM is driven by a Direct Digital Synthesizer (DDS) where the amplitude, the frequency, the phase and the duration of the signal are user-defined. More information about the DDS system can be found in [36]. The DDS output signal passes through an amplifier (ZHL-1-2W-S+) and then goes through a directional coupler (ZFDC-20-1H-S+ by Mini-Circuits). After the coupler the RF signal can be monitored through an RF power detector (CPDETLS-400 by Crystek microwave) which was mainly used for debugging. The optical signal after the fiber-coupled AOM is again monitored by a diode. Both diodes are calibrated such that we can compute the optical power before and after the Fibre-Q based on the voltage outputs from the diodes.

In our control program, we trigger a digital TTL signal together with any RF pulse. This means the TTL is switched on during the same time the DDS is outputting. The TTL signal is used in this characterization as a reference signal and helps to determine latencies in section 5.5. Therefore, we can use it to indicate the start and end of an RF pulse. We measured this TTL signal after a BNC cable roughly of the same length as the cable delivering the DDS RF output to the Fibre-Q AOM. In this way we made sure the TTL signal has similar propagation delay as the RF input to the AOM. The TTL signal is also used to distinguish between different AOM drive frequencies in the 2D scan described in the next section. The TTL signal, the diode signals and the signal out of the RF power detector were monitored using an oscilloscope.

5.4. AOM-device efficiency

5.4.1. Efficiency characterization

As a first step, the efficiency of the fiber-coupled AOM is measured. The coupling of the light into the fiber is optimized by tweaking the two mirrors before the fiber. Then the RF frequency that drives the AOM and its amplitude can be altered while the optical power after the fiber-coupled AOM is measured. The RF input power is calibrated using a spectrum analyzer (N9912A by FieldFox). A 2D measurement that scans through the RF power and frequency, that drives the AOM, is depicted in figure 13. The depicted

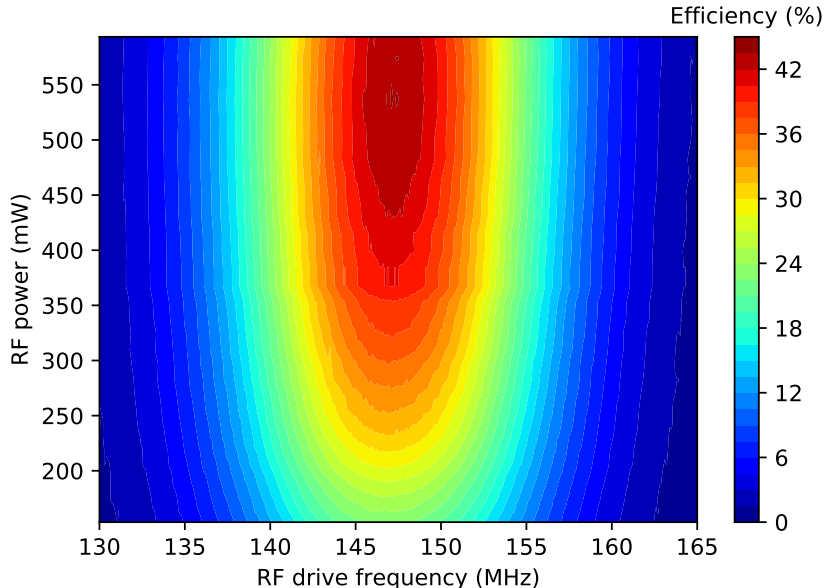


Figure 13: Efficiency of the fiber-coupled AOM as a function of the applied RF power and RF frequency. The plot is roughly centered around the RF frequency with the maximal efficiency. The RF power range is selected up to slightly above the saturation point.

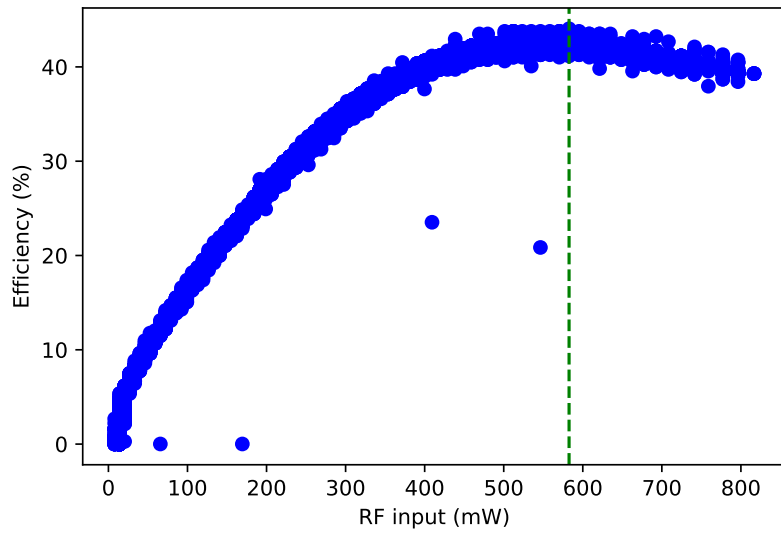
efficiency is the combined efficiency of the fiber-coupled AOM and the coupling into the fiber that is attached to the AOM.

Figure 14a shows the efficiency as a function of the amplitude of the RF input at a frequency of 147 MHz. We observe that after an offset the efficiency increases linearly until it reaches a saturation point. At an RF power of ~ 580 mW, the optical signal is maximal. The offset is likely to be an artifact of the calibration of the diodes which is less accurate for a low optical power. With the optimal RF power we scan through the RF drive frequency as depicted in figure 14b. From that we determined the bandwidth of the AOM as 15.7 MHz and the maximal efficiency is found at 147.3 MHz around 42%.

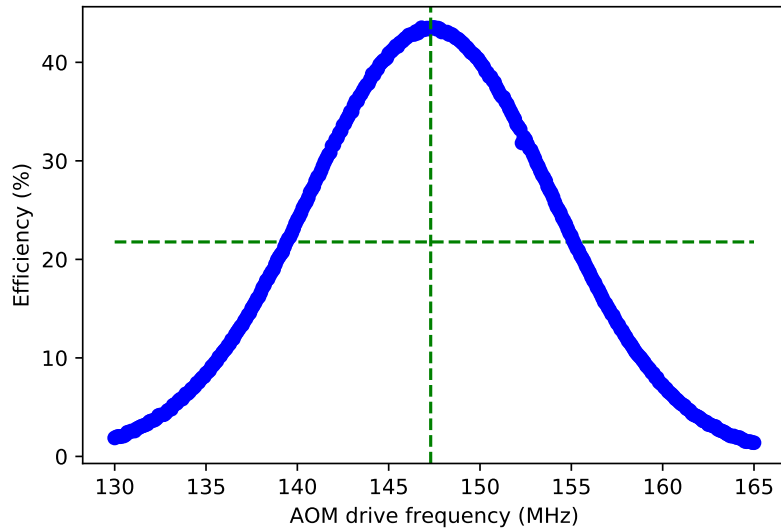
According to the specifications of the manufacturer, the AOM-device efficiency can reach values up to about 67%. This includes only the losses through the AOM and the coupling after the AOM into the attached fiber, however, it does not include any coupling losses from coupling into the fiber of the Fibre-Q. We verified this by using a mating sleeve and another fiber. The obtained AOM-device efficiency is consistent with the data from the manufacturer within the accuracy of this measurement. For this, the following steps are performed:

1. Calibration of the efficiency of the mating sleeve
 - Measurement of the optical power after the fiber-coupled AOM
 - Connect the output of the Fibre-Q to a second fiber (Nufern 630-HP) with a mating sleeve and measure optical output power after the fiber
 - The first value is the input of the latter and by this we can determine the efficiency of the mating sleeve joining these specific fibers to be $\sim 87\%$.
2. Estimation of AOM-device efficiency
 - Measure optical power through the Nufern 630-HP fiber
 - Connect the output of the fiber to the fiber-coupled AOM via mating sleeve and measure the optical power output of the Fibre-Q
 - We use the efficiency of the mating sleeve and the first value to determine the input power for the Fibre-Q. Then we compute the AOM-device efficiency together with the second value as 69.8% which corresponds well to the data from the manufacturer (67.6%).
3. Estimation of fiber coupling efficiency (of Fibre-Q fiber)

Given the 42% maximal efficiency including fiber in-coupling and the 69.8% Fibre-Q efficiency excluding the fiber in-coupling, we conclude that the in-coupling efficiency to the Nufern 780-HP fiber attached to the Fiber-Q AOM is only $\sim 60\%$. Using another fiber of the same kind we could not observe a higher efficiency. A possible limit is the cutoff frequency (730 ± 30) nm of the Nufern 780-HP fiber.



(a)



(b)

Figure 14: Efficiency measurements of the fiber-coupled AOM. (a) Efficiency of the fiber-coupled AOM as a function of the applied RF power with an RF frequency of 147 MHz. The dashed line indicates the maximum. (b) Efficiency of the fiber-coupled AOM as a function of the applied RF frequency with an RF power of ~ 580 mW. The dashed lines indicate the maximum efficiency and half of it.

5.4.2. Approaches and considerations to improve efficiency

Before we have managed to figure out the reason for the lower-than-expected efficiency, the following error sources are checked and excluded as being responsible for the low efficiency:

- The S_{11} reflection coefficient of the AOM is measured with a spectrum analyzer, see figure 15. Within the bandwidth of the AOM, we find a maximal reflection of $S_{11} = 15\%$ and at the frequency with maximal efficiency the reflection is $S_{11} = 3.8\%$. This corresponds to a power reflection of less than 0.3%.
- We check that the used fiber and AOM is indeed polarization independent by inserting a half-wave plate (HWP) and quarter-wave plate (QWP) before the laser beam is coupled into the fiber.
- We check the free-space fiber coupling by using another fiber of the same type.
- The shape of the laser beam before and after the fiber is checked as well, as displayed in figure 16. A moveable aspheric lens (A240TM-B with $f = 8$ mm by Thorlabs) has briefly been used to detect a potential improvement of the mode matching of the input beam to the fiber mode. We have moved back to the original setting due to lack of sufficient improvement.
- The fiber input and output is reversed to check if there is some odd behaviour.
- We check the fiber tip for dirt and scratches.

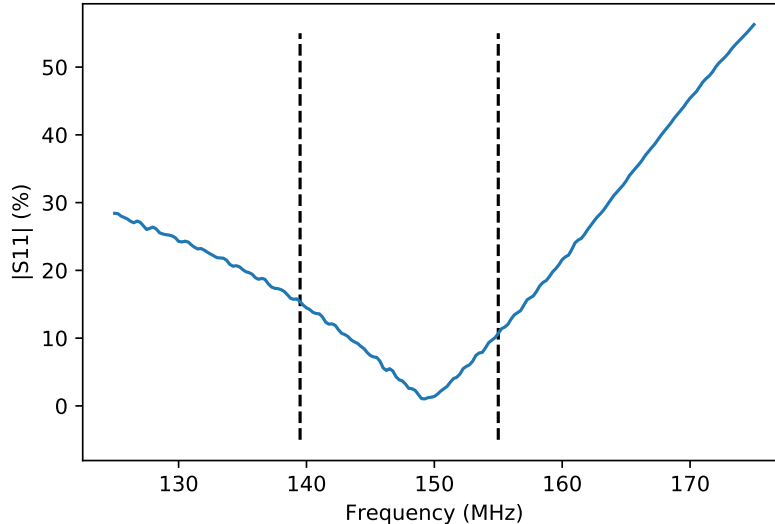


Figure 15: Reflection of the fiber-coupled AOM. The dashed lines indicate the bandwidth of the AOM.

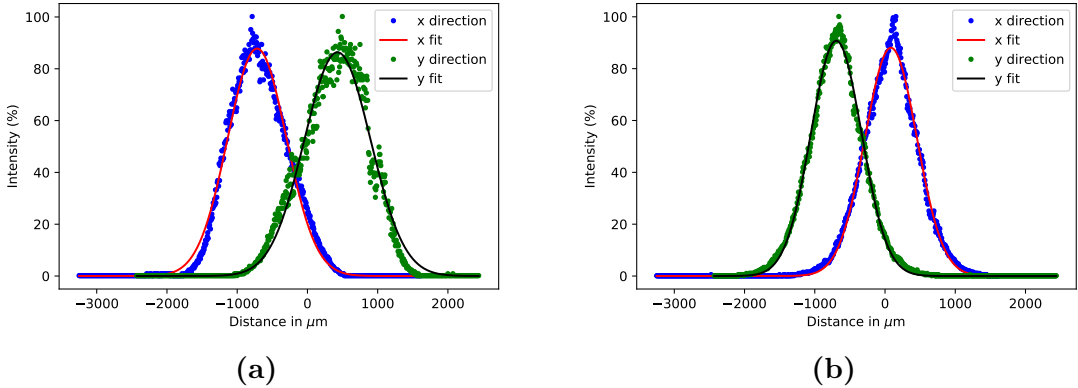


Figure 16: Laser beams in x - and y -direction (a) before and (b) after the fiber-coupled AOM. The beam diameter before the Fibre-Q is 1504 μm in x -direction and 1702 μm in y -direction. After the Fibre-Q the beam diameter is found to be 1329 μm in x -direction and 1302 μm in y -direction.

5.5. Pulse shaping effects

Since we plan to use this AOM to implement the pulse sequence for the entanglement of two ions, we are interested in how the AOM responds to the set parameters. Any distortion of pulses contributes to the gate fidelity. For this, we analyze the fiber-coupled AOM considering its rise and fall time when applying an RF pulse as well as the delay of the signal with respect to the TTL signal. Contrary to the overall efficiency, the manufacturer does not provide any specifications concerning the rise and fall time. The goal of this measurement is to check whether the rise and fall times are symmetric and if the overall duration set with the DDS is indeed implemented.

For this characterization we repeat the same pulse several times to gather statistics. The RF drive frequency and the amplitude was chosen such that the maximal diffraction efficiency of the fiber-coupled AOM is obtained, as found earlier. We use the minimal pulse length allowed by our control system, 1.5 μs , for this test. The setup is the same as the one for the previous case, except that we use a faster diode (DET10A/M by Thorlabs) to record the optical power after the Fibre-Q.

5.5.1. Delay of optical signal with respect to TTL signal

To determine the overall pulse duration of the AOM, we use the TTL signal as a reference. The TTL signal is measured close to the Fibre-Q AOM input to ensure a comparable delay time. Similar coaxial cables are used to deliver the TTL signal and the RF pulses driving the Fibre-Q AOM. We have defined the delay time as about 50% of the maximum of the TTL signal and also 50% of the maximal optical signal. Since the raise of the TTL signal is too fast to be resolved with the oscilloscope, only the rough value of 50% is used in the definition. A sequence of three pulses is shown in figure 17.

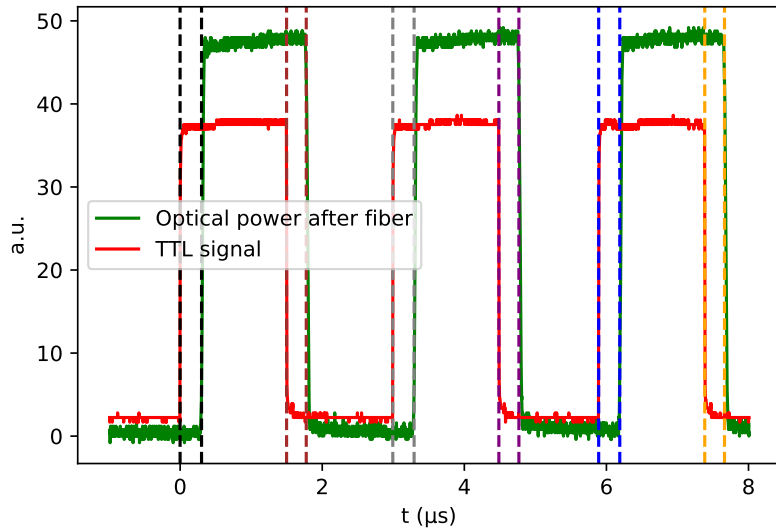


Figure 17: Sequence of three pulses showing the induced TTL signal (in red) and the optical signal (in green). The dashed lines indicate the start (and end) of the TTL and the optical signal.

We observe that the delay time is different for the rising and falling edge. Averaging over 50 pulses, we find that the delay time of the optical signal with respect to the TTL signal for the rising edge is (315.6 ± 2.3) ns while the delay time for the falling edge is found to be (298.7 ± 2.5) ns. This indicates that the optical output pulse is shorter than the electronic input pulse. We have also taken a measurement where we monitor the TTL signal and the RF signal before and after amplification as well as over the power detector after the amplification. The delays displayed in figure 18 indicate that we have indeed a delay of the RF signal compared to the TTL signal, however, we observe that the total delay of about 40 ns (see figure 18) is only a small part of the delay of the optical signal relative to the TTL signal.

5.5.2. Rise and fall time

The rise time is defined by the difference of the time it takes in which the signal goes from 10% to 90% of its final value. On the contrary, the fall time is defined by the time it takes for the signal to drop from the 90%-level to the 10%-level. We have used the same setup to measure the rise and fall time of the Fibre-Q AOM. An example of the analysis there is given in figure 19. Averaging over the same 50 pulses as above, we observe an average rise time of (32.2 ± 0.9) ns and fall time of (36.8 ± 1.3) ns. Consequently, each Rabi frequency level in equation 37 is in fact time-dependent.

It may be interesting to explore this further, especially when moving towards faster gates. Within this thesis, the rise and fall times are a minor effect, because the pulses we intend to use have a much longer duration where we expect that this effect would

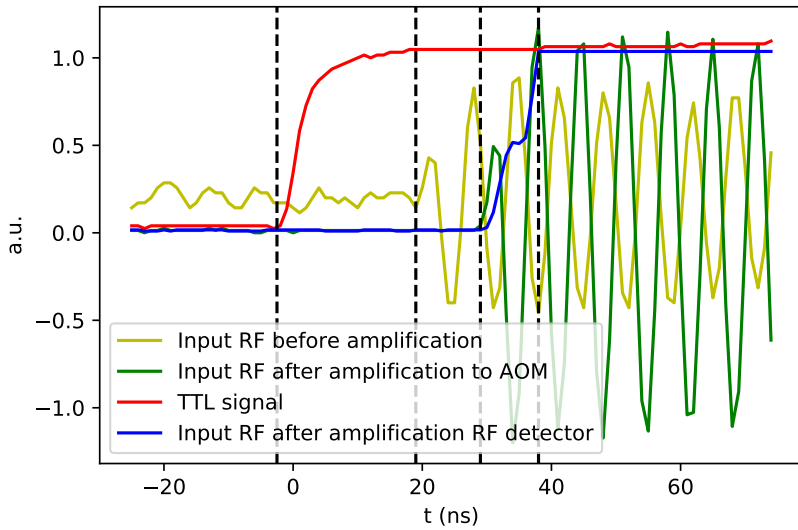


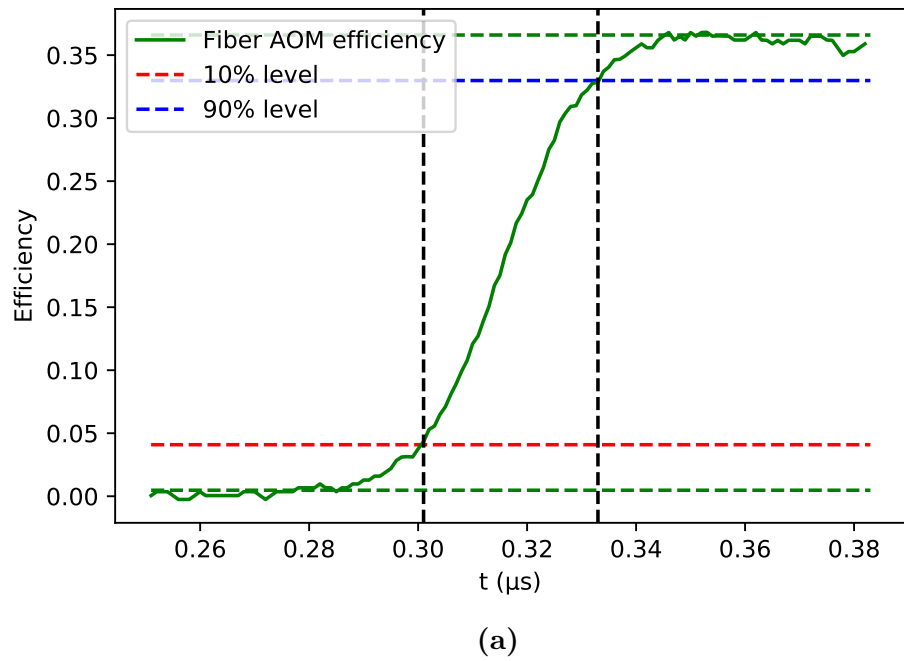
Figure 18: Monitoring delay times of the RF signal at several places with respect to the TTL signal. The RF signal is triggered from the DDS and then monitored before (yellow) and after amplification in two ways. We monitor the RF signal that drives the AOM (green) and through a RF detector (blue). The power detector allows to monitor the RF signal when the RF signal is connected to the AOM. In this measurement the RF signal that usually goes to the AOM is connected to the oscilloscope as well.

have only little influence. Also, in real experiment we can calibrate the Rabi frequencies to compensate this effect.

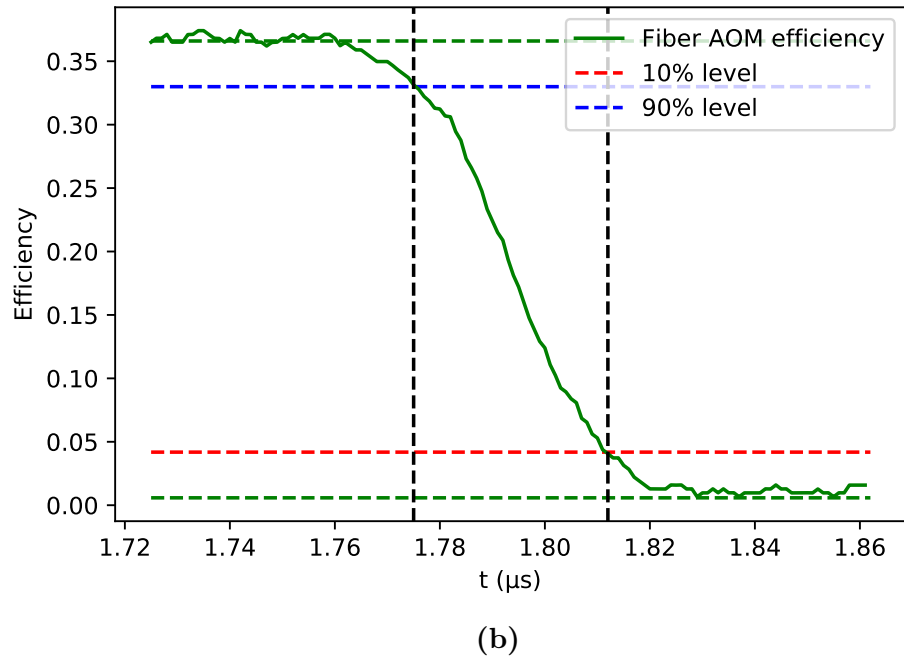
5.5.3. Optical power fluctuations and drifts

In figure 17, we note that the amplitude of the pulse, i.e. the AOM efficiency, increases slightly when the AOM is driven. This effect is minor considering that our intended pulse sequences will be of much longer duration and therefore, by calibration is likely compensated.

We have also investigated the effect due to the duty cycle of the pulses on the optical output power. The reasoning for this is the RF drive of the AOM that can heat up the device which may result in different outputs depending on how long the AOM is switched off between two pulse sequences. It turned out that the average amplitude of a pulse stays constant over a set of 100 pulses with a spread of 0.4% – 0.6% for a pulse length of 100 μ s and an off-time of 4.5 μ s, 50 μ s, 100 μ s, 200 μ s, 400 μ s and 800 μ s. This spread is also observed when monitoring the laser power without the AOM. We conclude that duty cycle effects are below these fluctuations.



(a)



(b)

Figure 19: Example for the analysis of the (a) rise and (b) fall time. Red and blue dashed lines indicate the levels that are needed to determine the corresponding times, green dashed lines show the start and final levels of the efficiency and black dashed lines mark the corresponding times.

5.5.4. Influence of power fluctuations and pulse length on gate fidelity

Given the optimal pulse sequences computed in section 4, we have done a small check on how the fidelity changes, if we take the findings of the previous sections into account. In this short sanity check we only consider the delay of the optical signal with respect to the TTL signal, because this signal defines the effective length of the pulse, and do not take into account the small asymmetry of the rise and fall time. Given the delay of the TTL signal, a single optical pulse is on average 16.9 ns shorter than its electronic setting. Given nine (29) Rabi levels, the pulse is shortened by 152.1 ns (466.9 ns).

As an example we will look at the optimal pulse sequence for the entanglement of ion 1 and 2 for 100 μs and 40 μs . The infidelity for the 100 μs -gate increases slightly from $1.9 \cdot 10^{-5}$ to $3.4 \cdot 10^{-5}$. For the faster gate with more Rabi levels we find an increasing infidelity from $4.6 \cdot 10^{-4}$ to $5.5 \cdot 10^{-3}$.

The above assumption highly overestimates the overall effect because it assumes that each levels is turned on and off rather than actually raising (or lowering) to the next level. In fact, in the latter case, only the pulse in the middle of the sequence will be shortened, since the delay is equal for all other segments because the delay of rising (falling) different levels is expected to be similar. Nevertheless, it shows that the influence of this distortion gets more significant, when the gate is implemented in a faster way.

The power fluctuations can also affect the overall gate fidelity. Based on the previously found power drift of up to 0.6%, we again compute the infidelity with reduced (and increased) Rabi frequency levels. Since $\Omega \propto \sqrt{P}$, for $\frac{\Delta P}{P} = 0.3\%$ we find that $\frac{\Delta \Omega}{\Omega} = \frac{1}{2} \frac{\Delta P}{P} = 0.15\%$.

As an example, we again look at the case of ion 1 and 2 for a gate time of 100 μs and 40 μs . Raising (lowering) the Rabi frequency levels by 0.15% leads to an increase of infidelity from $1.9 \cdot 10^{-5}$ to $2.0 \cdot 10^{-5}$ ($2.8 \cdot 10^{-5}$) for the 100 μs -gate. For the faster gate, we find $4.9 \cdot 10^{-4}$ ($4.3 \cdot 10^{-4}$) instead of $4.6 \cdot 10^{-4}$. We conclude that power fluctuations are minor error sources.

6. Characterization of SiN photonics within an ion trap

The goal of the ion trapping chip is not only to actually trap the ions. It also provides a route for the optical signals necessary to perform computations that are implemented by single qubit gates as well as entangling gates such as simulated in section 4. It is, therefore, important that the laser light propagates towards the ion in a reliable way. The laser beam will go through amplification stages and an AOM setup to obtain the desired amplitude, phase and frequency. Then it needs to be coupled from the fiber to the waveguides of the chip. Once the light is coupled into the waveguides, the design of the chip ensures that it propagates towards the ion in a fixed angle by passing the corresponding grating couplers. The challenge addressed here is to optimize the fiber coupling to each waveguide addressing a different ion.

First, some basic theory on waveguides is presented. The losses caused by coupling from a fiber to a waveguide and the waveguide losses due to absorption and scattering are characterized. Different possibilities to improve fiber-to-waveguide coupling are explored afterwards.

6.1. Theory on waveguides

To get a basic understanding of waveguides, we consider ray optics. A waveguide is schematically presented in figure 20. The core of the waveguide has a higher refractive index than the cladding. Through Snell's law we can find the condition of the critical angle $\theta_c = \arccos \frac{n_2}{n_1}$. If $\theta \leq \theta_c$, Snell's law for transmission into the cladding of the waveguide cannot be satisfied and we find that all light is reflected inside the core. This total internal reflection makes the guidance of light in waveguides possible. The zig-zag form of the propagation leads effectively to a superposition of two waves with a different propagation direction. Any superposition is then of the form $E \propto e^{-i\beta z}$ where $\beta = n_{\text{eff}} k_0$ is propagation constant in z -direction. In principle, we can have many different modes that are guided through the same waveguide, however, in our case, the design only allows for one mode.

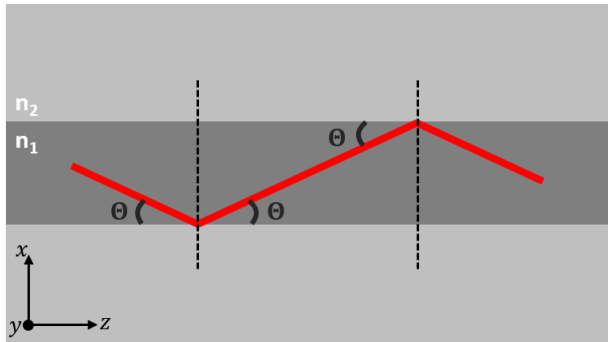


Figure 20: Schematic of a planar waveguide with $n_1 > n_2$. Since the light gets fully reflected at the boundary of the core, the incident angle satisfies $\theta \leq \theta_c$.

The mode solutions can be calculated by solving the wave equation. We give a brief overview of the derivation where we follow [37].

Maxwell's equations combined lead to the second-order wave equation which is given by

$$\nabla^2 U - \frac{n^2}{c^2} \frac{\partial^2 U}{\partial t^2} = 0,$$

where U denotes a component of the electric E or magnetic field H , n is the refractive index and c denotes the vacuum speed of light. After the application of a Fourier transform, the equation is solved in the frequency domain. We make the ansatz $U(x, y, z) = A(x, y)e^{i\beta z}$ which assumes a field solution perpendicular to the propagation direction and are left to solve

$$\left(\frac{\partial^2}{\partial x^2} + \frac{\partial^2}{\partial y^2} \right) A + (n^2 k_0^2 - \beta^2) A = 0.$$

If we assume that the core has a thickness of d , then the TE mode is given by

$$E_y \propto \begin{cases} e^{-\gamma_x(x-d/2)} & \text{for } x > d/2 \\ \cos(k_x x) & \text{for } |x| < d/2 \\ e^{\gamma_x(x+d/2)} & \text{for } x < -d/2. \end{cases} \quad (44)$$

The propagation constant in x -direction is given by k_x and the γ_x denotes the penetration depth.

We observed that there is an electric field inside the core that oscillates as a function of x . There is also an electric field in the cladding which decays over distance.

A similar calculation leads to the solution of the TM mode.

6.2. Measurement setup and investigated samples

Laser light is brought to a waveguide edge with a bare fiber which is adjusted by manual stages to maximize the overlap of the laser beam of the fiber with the waveguide. The location of the fiber relative to the waveguide is monitored with a microscope. Light leaving the waveguide at the end of the chip is collected with another bare fiber, and delivered to a powermeter for measurement. We use a fiber splitter (TW670R1A1 by Thorlabs) to pick off 1% of the input power which is sent to a powermeter for monitoring. An image of the setup is displayed in figure 21.

The waveguides that were used for this measurement are shown in figure 22. Figure 22a shows the full chip with different waveguides, figure 22b shows the waveguides with different testing lengths that were used for the measurement and figure 22c shows a close-up of individual resonators that are coupled to a single waveguide.

The chips are manufactured by *LioniX*. The layer structure of the chip is shown in figure 23. Silicon is chosen as the substrate for the chip. The waveguides are structured by two layers of Si_3N_4 on top of a layer of silicon dioxide. After light is coupled into

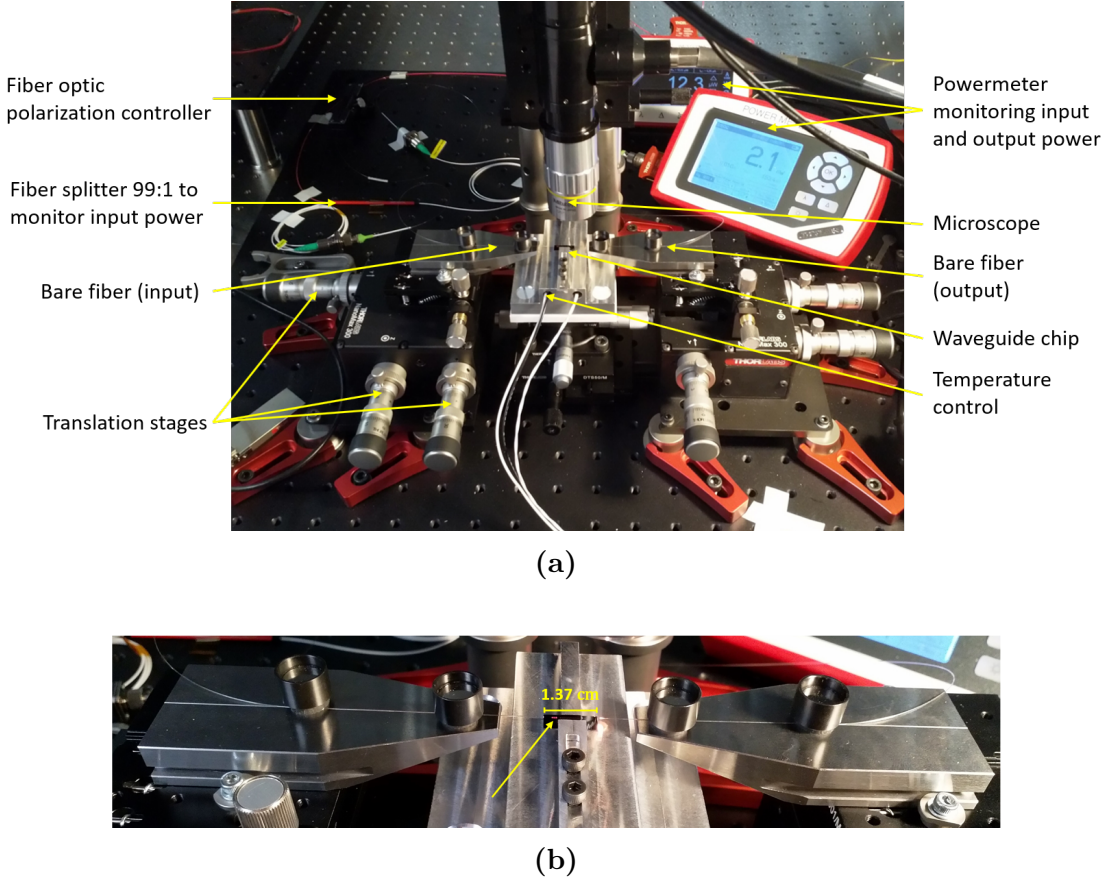


Figure 21: Experimental setup. Image (a) shows all relevant parts of the setup, (b) shows a close-up of the sample in the vicinity of the fibers. The red light (indicated by yellow arrow) that can be seen on the surface of the sample corresponds to the waveguide losses in one of the tested waveguides shown in figure 22b.

the waveguide in the low-confinement layer with a thickness of 25 nm, it is transferred to a more confining waveguide structure with a thickness of 170 nm which allows to guide light through the chips to its dedicated location while reducing losses. The trap electrodes are located on top of the chip. Each two functional layers are spaced by a silicon dioxide insulation layer. Between the top metal layer and the SiN layer, there is a Pt layer forming a ground plane. The usage of the ground plane is discussed in [38].

6.3. Characterization of waveguide losses

Since the waveguide chips are used to direct laser light to the trapped ions, we need to know the optical power losses to determine the overall input power. This is essential to have the right Rabi frequency for ion entanglement. We start by simple measurements where the transmission for a set of waveguides of different length is measured. Another approach to determine power losses is to measure ring resonator resonances.

Coupling light from a fiber to a waveguide results also in losses. These coupling losses will be discussed and methods to improve the coupling are outlined.

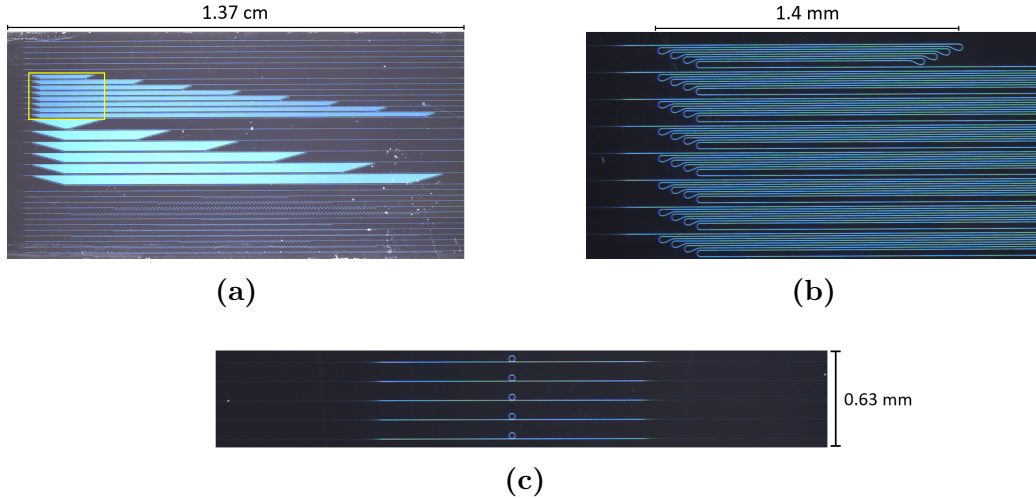


Figure 22: Images of the testing chips. (a) Full image of chip with different testing lengths of waveguides, (b) close-up of used waveguides for waveguide loss characterization (indicated by the yellow box in (a)). (c) Close-up of single waveguides coupled to single ring resonators.

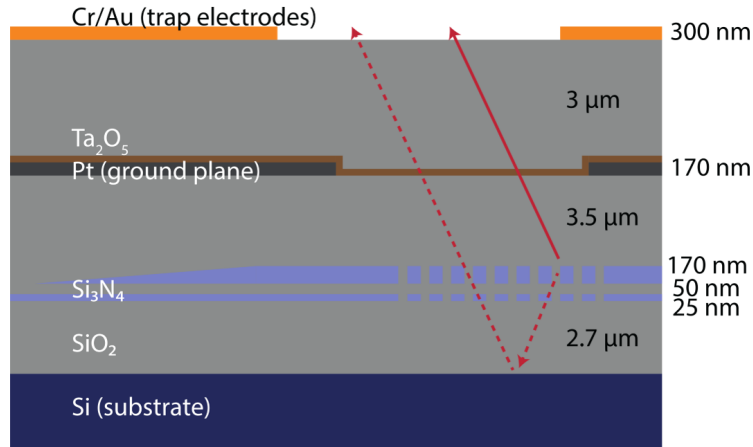


Figure 23: Schematic of the layer structure on the chip. The waveguides (light blue) have two different stacks. The smaller structure and therefore, less confining waveguide is used to couple light into the waveguide (at the left of schematic). The larger and more confining waveguide directs light through the chip towards its dedicated target by passing the gratings as indicated by the red arrows. The trap electrodes are at the top of the chip with a ground plane that is 3 μm below. Courtesy of Dr. Karan K. Mehta.

6.3.1. Measurement of optical power transmission for different waveguide lengths

One approach to determine the losses is to measure the transmission through waveguides of different length. The loss constant α is defined by [39, p. 348]

$$\alpha = \frac{1}{L} 10 \log_{10} \frac{1}{\mathcal{T}}, \quad (45)$$

where L denotes the length of the waveguide and $\mathcal{T} = \frac{P(L)}{P(0)}$ is the optical power transmission. For waveguides of different length, the transmission plotted on a dB-scale as a function of length of the waveguide indicates the coupling loss by fitting a straight line onto the data points. Taking into account any waveguide length in addition to the testing lengths, we can determine the coupling. The loss constant is determined by the slope of this straight line.

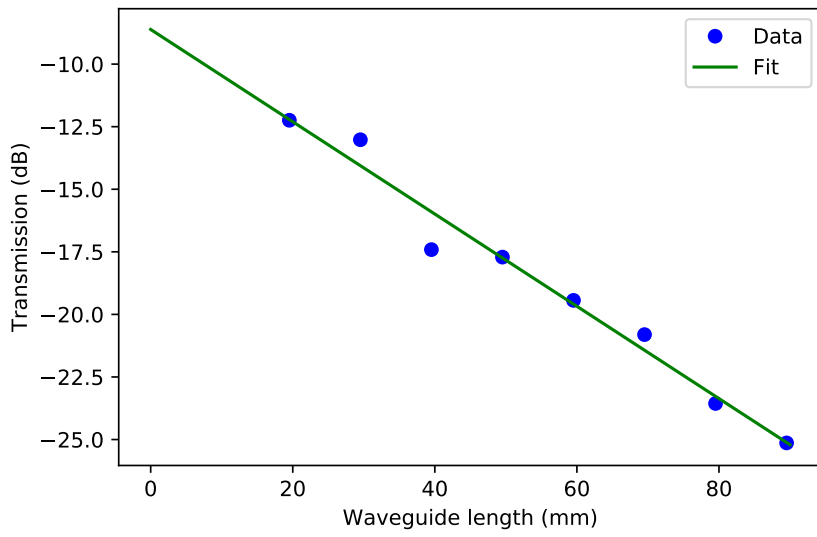
This measurement was conducted for different samples of the same design. However, the samples are placed on different locations of the wafer. Two examples are shown in figure 24. The measurements indicate a waveguide loss of $\alpha = (1.84 \pm 0.12) \text{ dB/cm}$ and $\alpha = (2.43 \pm 0.14) \text{ dB/cm}$, respectively, and a constant loss of $\gamma = (4.31 \pm 0.37) \text{ dB}$ and $\gamma = (3.31 \pm 0.41) \text{ dB}$, respectively. The constant loss includes the coupling loss and the bent structures of the tested waveguides. This points out the difficulty to reach the optimal coupling for each waveguide and shows the sensitivity of the waveguide losses on the coupling. To determine the waveguide loss more independently from the coupling loss, the resonances of a ring resonator, that is coupled to the waveguide, are measured. This is discussed in the following.

6.3.2. Waveguide losses determined by resonator resonances

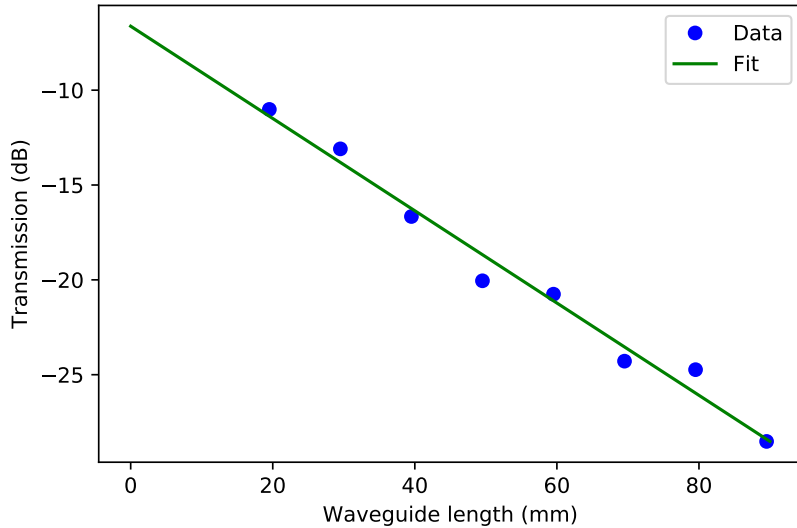
Some parts of the samples are dedicated to ring resonators. Ring resonators with a grating on its inner boundary can emit circularly polarized light which can be exploited for quantum operations when using integrated optics. More details about this topic can be found in [40]. For the determination of the waveguide losses given by absorption and reflection we only look at resonators without the grating on the inner boundary of the ring.

The following theory is based on [41] adjusted to the case of one rather than two waveguides coupled to a ring resonator as shown in figure 25. Essentially, this is a modified Fabry-Perot resonator where one of the mirrors has reflectivity of 100%. The main aspect that is taken into account in [41] is the surface roughness of the waveguide. This leads to a splitting of the resonance where the degeneracy of the forward and backward propagating modes in the resonators is lifted. The authors define an effective reflection coefficient R which is due to random surface perturbations.

To determine the transmission, the amplitudes in the waveguide and ring resonator as shown in figure 25 are taken into account to compute the steady-state response of the



(a)



(b)

Figure 24: Transmission measurements of different samples with eight different waveguides of testing length 10 mm to 80 mm in 10 mm-steps. For each waveguide we have an additional length of 9.52 mm. Measurement (a) indicates a loss of $\alpha = (1.84 \pm 0.12) \text{ dB/cm}$ and a constant loss of $\gamma = (4.31 \pm 0.37) \text{ dB}$, measurement (b) leads to a loss of $\alpha = (2.43 \pm 0.14) \text{ dB/cm}$ and a constant loss of $\gamma = (3.31 \pm 0.41) \text{ dB}$. Both measurement series were taken with 729 nm light. The optical power that is coupled to the waveguides is $\sim 1 \text{ mW}$.

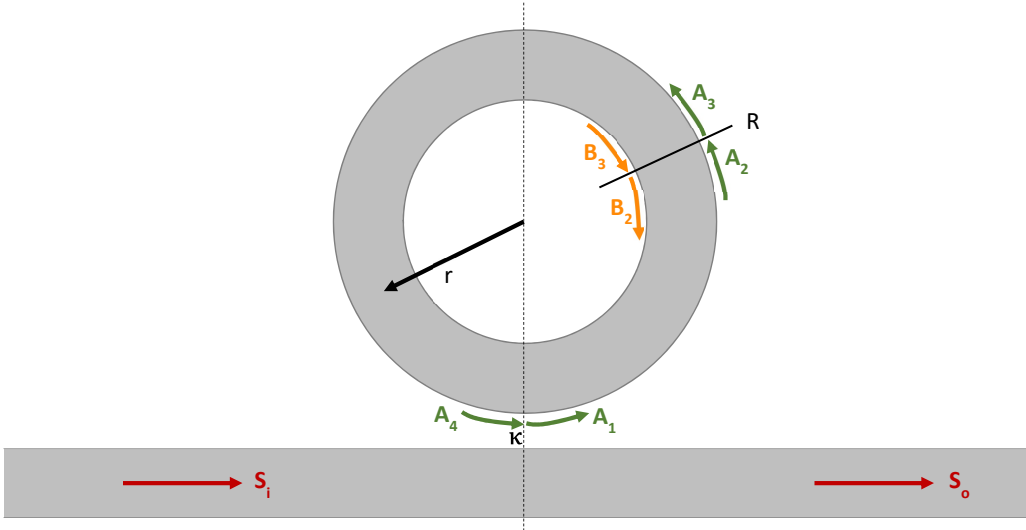


Figure 25: Waveguide coupled to a ring resonator. S_i (S_o) denotes the amplitude of the input (output) power. The amplitudes A_i (B_i) indicates the counter-clockwise (clockwise) propagating mode. The coupling between the waveguide and the resonator is denoted by κ and the effective reflective index is given by R . The radius of the ring resonator is r .

ring resonator. In the schematic, S_i determines the amplitude of the input power, S_o the one of the output power. The amplitudes A_i indicate the counter-clockwise propagating mode and B_i the clockwise propagating mode. The coupling between the waveguide and the resonator is denoted by $\kappa = \sqrt{1 - t_\kappa}$, where t_κ denotes the transmission within the waveguide and resonator, respectively. Similarly, the effective reflective index is given by $R = \sqrt{1 - t_R}$. The radius of the ring resonator is denoted by r . The equations for the amplitudes are now given by

$$\begin{aligned} A_1 &= -i\kappa S_i + t_\kappa A_4 \\ A_2 &= A_1 & B_2 &= -iR A_2 + t_R B_3 \\ A_3 &= t_R A_2 - iR B_3 & B_3 &= t_\kappa e^{-i\phi} B_2 \\ A_4 &= e^{-i\phi} A_3, \end{aligned} \tag{46}$$

where $\phi = 2\pi r \beta_r - i\alpha_{\text{ring}} \pi r$ where $\beta_r = \frac{2\pi}{\lambda} n_{\text{eff}}$ is the ring propagation constant. The waveguide loss is attached to the phase for simpler notation, which leads to a complex number within the phase. The wavelength is denoted by λ , the effective refractive index is given by n_{eff} . The quantity α_{ring} describes the loss in the ring resonator. To deduce the waveguide loss α from α_{ring} , we consider an input power $|E_{\text{in}}|^2 = 1$. Then the power after one loop is reduced with respect to the losses to $|E_{\text{out}}|^2 = e^{-2\alpha_{\text{ring}} \pi r}$. We use equation 45 for $L = 2\pi r$ to finally compute α . In this manner, we neglect the losses from the bend structure which was simulated to be of order 10^{-4} dB/cm.

Putting the equations together and using $S_o = -i\kappa A_4 + t_\kappa S_i$, the transmission is given by

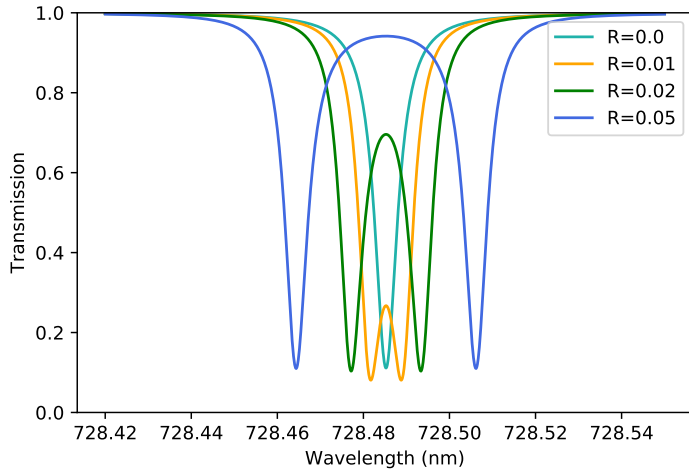
$$\mathcal{T} = \left| \frac{S_o}{S_i} \right|^2 = \left| \frac{-\kappa^2 e^{-i\phi} (t_R - t_\kappa e^{-i\phi})}{1 - 2t_\kappa t_R e^{-i\phi} + t_\kappa^2 e^{-2i\phi}} + t_\kappa \right|^2. \quad (47)$$

Together with the effective refractive index, the radius of the ring defines the frequency of the resonance. The coupling between the waveguides determines the depth of the resonance dip. The impact of the effective reflectivity and the loss constant are shown by simple example plots in figure 26 to get some basic understanding. The reflectivity defines the separation of the two resonances which approaches zero as the reflectivity is decreased. The loss essentially defines the width and depth of the resonances.

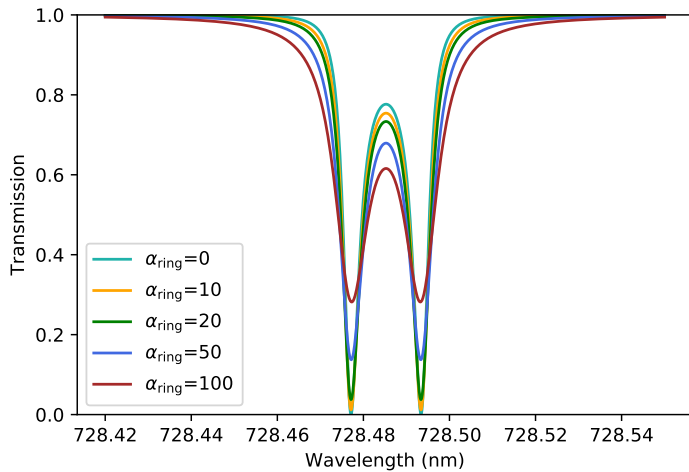
Figure 27 shows example transmission measurements of resonators with two different spacings between the waveguide and the resonance. The measurements were conducted on two different samples with identical design. The transmission given in equation 47 needs to be multiplied by a factor which takes into account the coupling losses and the waveguide losses for the light propagating from the beginning of the waveguide to the resonator and then to the end of the waveguide. Within the range of one measurement, the waveguide losses are considered to be independent of the wavelength because the wavelength is changed by only ~ 0.02 nm. An initial approach to fit a noise model of the form $a\lambda + b$ onto the data was dismissed, because the noise model had a higher weight compared to the physical model. Fitting the measured data requires a good initial guess of the parameters to be successful. A simple *Mathematica Manipulate* notebook was used to determine these. The corresponding fitted parameter are summarized in table 4. The coupling is not consistent within error bars for the two different samples. A possible explanation may be the level of noise. The coupling indicates that it is reduced with increased distance between the waveguide and the resonator which is consistent with our expectations. The effective reflectivity is different for each of the measured resonances indicating that the surface roughness differs for the individual resonators. The waveguide loss ranges between 1.78 – 2.21 dB/cm for 15 fitted measurements which gives a coupling

Table 4: Fitted parameters for measurements shown in figure 27. The ring resonator losses can be transferred to waveguide loss per cm, where we assume that the losses due to the bending are neglectable and consider α_{ring} for one loop in the resonator. We find (1.96 ± 0.04) dB/cm, (2.21 ± 0.08) dB/cm, (2.03 ± 0.01) dB/cm and (1.89 ± 0.08) dB/cm in the displayed order.

	Coupling κ	Effective reflectivity R	α_{ring} (1/m)
(a)	0.0372 ± 0.0002	$0.00364 \pm 3 \times 10^{-5}$	45.1 ± 0.9
(b)	0.0291 ± 0.0004	$0.00544 \pm 7 \times 10^{-5}$	50.8 ± 1.9
(c)	0.0337 ± 0.0004	0.00123 ± 0.00015	46.6 ± 2.2
(d)	0.0257 ± 0.0003	$0.00263 \pm 6 \times 10^{-5}$	43.4 ± 1.9



(a)



(b)

Figure 26: Transmission of waveguide coupled to ring resonator as a function of wavelength. The figures plot different values of (a) effective reflectivity and (b) loss constant while keeping the other parameters fixed. The first parameter defines the width of the splitting of the resonance whereas the second parameter define the depth and width of the resonances.

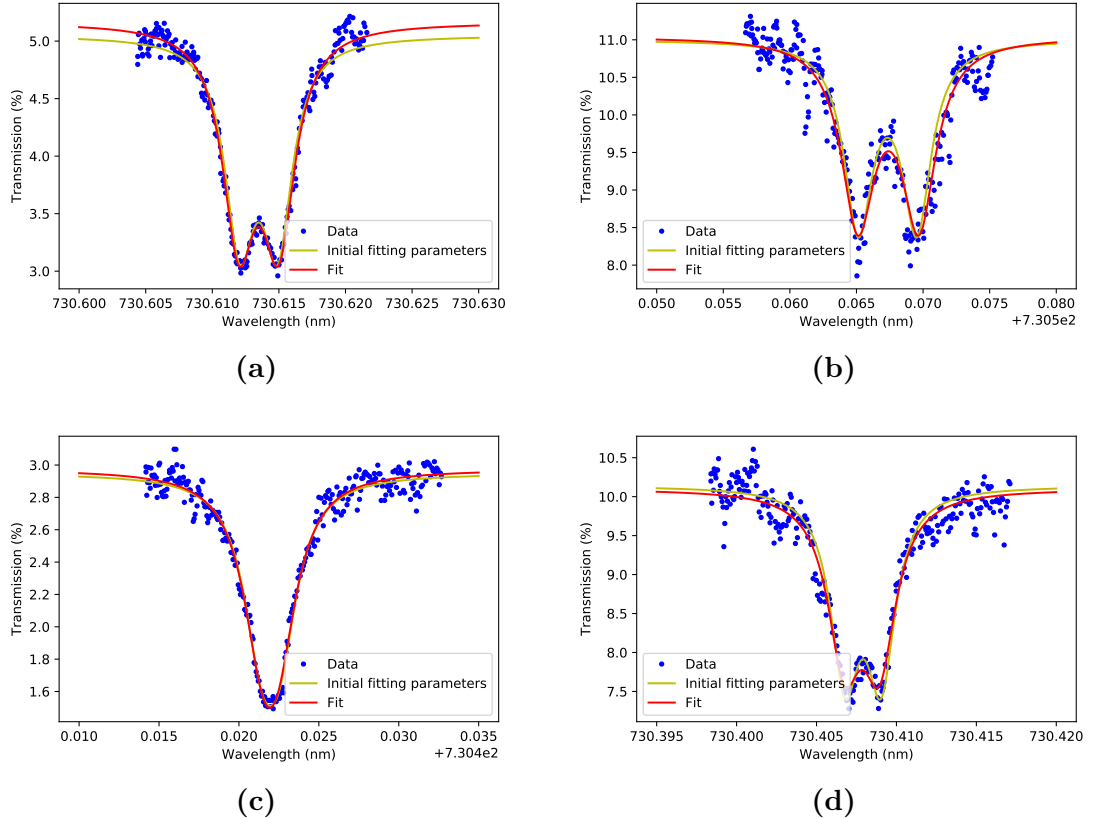


Figure 27: Transmission of waveguide coupled to a ring resonator with a radius of $20 \mu\text{m}$ as a function of wavelength. (a) and (b) as well as (c) and (d) are resonators on the same sample. The distance between the resonator and the waveguide, that it couples to, is 489 nm for (a) and (c) and 529 nm for (b) and (d), respectively. The plots represent examples of the measured data. The fitted parameters are summarized in table 4. The optical power that is incoupled to the waveguides is $\sim 1 \text{ mW}$.

independent estimation and confirms the previous measurement of about 2 dB/cm. A waveguide loss of 2 dB/cm is a relatively high compared to the values stated by *LioniX* in [42].

6.3.3. Methods to improve fiber to waveguide coupling

To improve coupling losses, index matching gel (type G608N3) can be used which removes the small air gap between the fiber and the waveguide. The gel seems to improve the overall transmission first, however, the drawback is that it is hard to see the exact location of the fiber relative to the chip under the microscope. This reduces the probability to achieve consistent coupling into different waveguides. Since the gel gets more viscous over time, it is even harder to adjust because of the induced tension. Due to these disadvantages, the gel was no longer used after some initial measurements. Besides, the index-matching gel would not be used for the fiber array attachment to the ion trapping chip.

The edges of the samples are not polished after dicing. To decrease coupling losses, we polished the edges of the sample to reduce its surface roughness. A piece of fused silica was glued upon the chip to ensure that the fiber can still be adjusted close to the waveguide. This helps to keep the curvature induced by polishing only at the edges of the glass and the bottom of the chip, rather than at the location of the waveguides.

The chip was fixed in a holder to handle the polishing procedure. The surface was polished in a four step polishing process where polishing papers with a grit size of 6 μm , 3 μm , 1 μm and 0.02 μm were used. The results after each step are shown in figure 28. The chip was moved up and down ($\uparrow\downarrow$) as indicated by the red arrow. We do not want to move the chip in the other direction (\leftrightarrow) to prevent a curvature along the different waveguides. This would lead to a non-uniform coupling for the set of waveguides under test. This procedure can be easily understood when taking into account that we want to glue a stack of fibers onto the chip where all fibers ideally have the same coupling into the waveguide. The chip was flipped every 10 to 20 movements by 180° such that the pressure is applied onto the surface in a uniform way.

Figure 29 shows a transmission measurement of an unpolished sample and the same polished sample. The constant losses improved from $\gamma = (4.02 \pm 0.36)$ dB for the unpolished version of the sample to $\gamma = (3.44 \pm 0.31)$ dB/cm for the polished one. We note that they are consistent within the error bars, but we are confident that polishing does lead to an improvement: First, for every single measurement point, we can observe that the transmission is improved. Also, we observe that the waveguide losses α appear to be less for the polished case. Since we expect these losses to be the same, the coupling for the polished sample is likely overestimated or alternatively underestimated for the unpolished sample. Both considerations indicate that polishing the edge of the sample leads to an improvement of the coupling from fiber to waveguide.

As a sanity check, we also looked at the straight waveguides of the samples and compared the measurements of the unpolished and polished versions. They confirm the

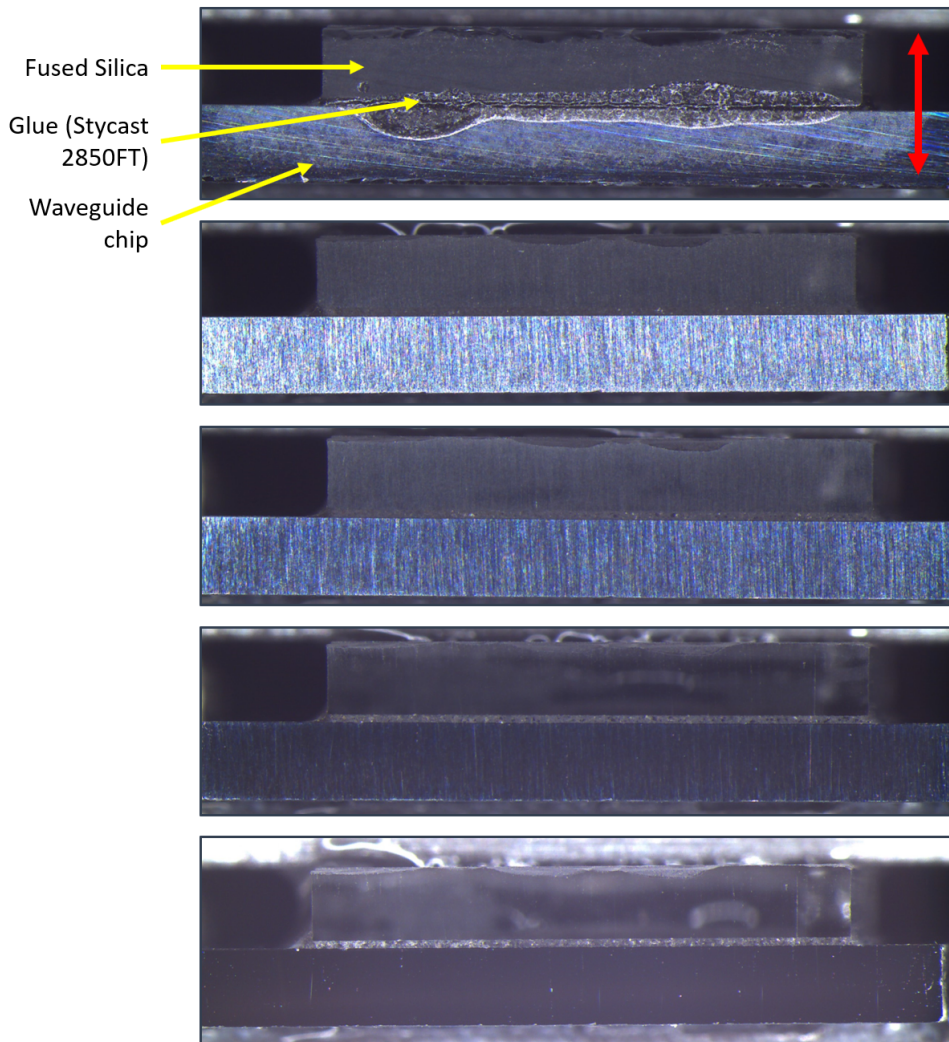


Figure 28: Sample surface with glass piece glued upon. The waveguides are located just below the surface of the chip. The red arrow indicates the movement during the polishing process. The images show the unpolished sample (top) and the result of all polishing steps (second to last).

improvement in coupling when polishing the edges of the sample where the loss per coupler decreased from 3.4 dB to 2.8 dB. This indicates that the coupling is, in fact, improved by polishing. The bent structures in the tested waveguides were neglected and contribute approximately 0.7 dB per waveguide to the constant losses which results in an expected coupling loss of \sim 3.1 dB for a polished sample and is consistent within error bars of the finding for straight waveguides.

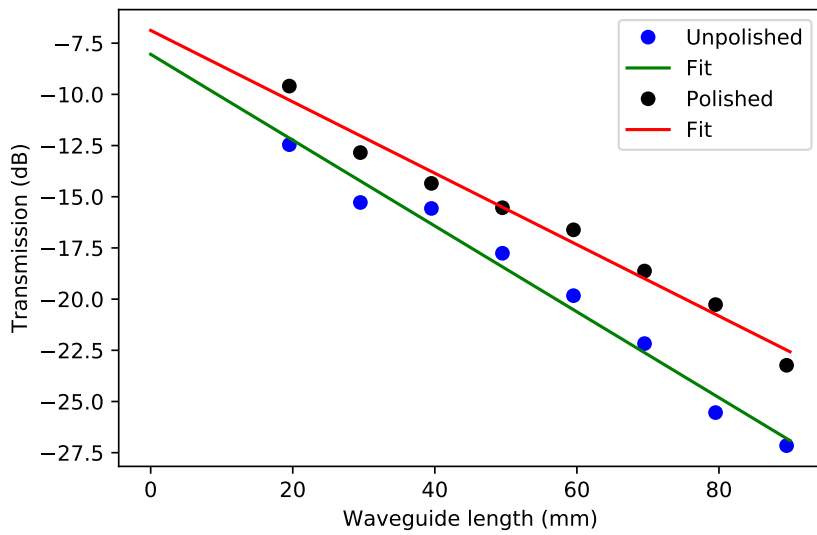


Figure 29: Transmission measurements as in figure 24. The measurement was conducted of one sample before (blue/green) and after polishing (black/red). The losses for the unpolished sample are found to be $\alpha = (2.1 \pm 0.1)$ dB/cm and $\gamma = (4.02 \pm 0.36)$ dB. The polished sample results in losses of $\alpha = (1.74 \pm 0.11)$ dB/cm and $\gamma = (3.44 \pm 0.31)$ dB/cm. The measurement series was taken with 729 nm (730 nm) light for the unpolished (polished) sample. The optical power that is incoupled to the waveguides is ~ 1 mW.

7. Conclusion and outlook

In this thesis, I have presented the theoretical background on the entanglement of two ions within a linear ion chain. Based on this theory, I have implemented an optimization that determines the optimal pulse shape to entangle a given pair of ions in the ion chain and a specific gate time. Expected infidelities for the entanglement of all possible ion pairs are computed. The simulations on entangling gates indicate that any pair of a linear ion chain with five ions can be entangled for gate times $\geq 60 \mu\text{s}$ with an infidelity of $< 10^{-4}$. For lower gate times, the number of different Rabi frequency levels may need to be increased to reach better infidelities. The induced Stark effect, that is not considered in this simulation so far, can be compensated by changing the detuning μ for each of the Rabi levels appropriately. The off-resonant carrier excitation is of greater importance, the faster the MS-gate is implemented. This will limit the overall infidelity in the end.

The fiber-coupled AOM appears to be a good device to shape the laser light accordingly. We have observed that the electronic pulse is not exactly the one that is implemented when driving the AOM. For gate times on the order of tens of μs , these characteristics do not seem to limit us in terms of infidelity.

The characterization of the waveguides has shown that the waveguide losses are $\sim 2 \text{ dB/cm}$. The coupling losses could be improved by 0.6 dB per coupler if the edges of the sample were polished in the four step polishing process. Initial tests on the chips with the electrodes on top indicate that the same effect can be obtained.

It remains to implement the optimal pulse sequences on the trap. Next steps include to attach the fiber array to the chip and test each of the fiber-to-waveguide couplings as well as the gratings which direct laser light from the waveguides to the trapped ions.

We hope to gain further knowledge by testing the traps in terms of scalability. The possibility of addressing each ion individually together with a segregated trap would allow us to work towards better scalability in the field of trapped ion quantum computing.

To work towards faster gates, we need to reduce the effect of the off-resonant carrier excitation in the MS-Hamiltonian. A potential solution is to implement a standing wave during the gate which compensates this effect. Simulations were obtained in another project [43] and the corresponding chip designs will be tested soon [8].

A. Optimal pulse shape and phasespace diagrams

The optimal solutions for entanglement of any ion pair for different gate times τ_g is presented. The Rabi frequency levels as well as the phasespace diagrams for the radial normal modes in z -direction are shown. Relevant numbers are stated in the corresponding captions of the figures.

A.1. Solutions for a gate time of $\tau_g = 100 \mu\text{s}$

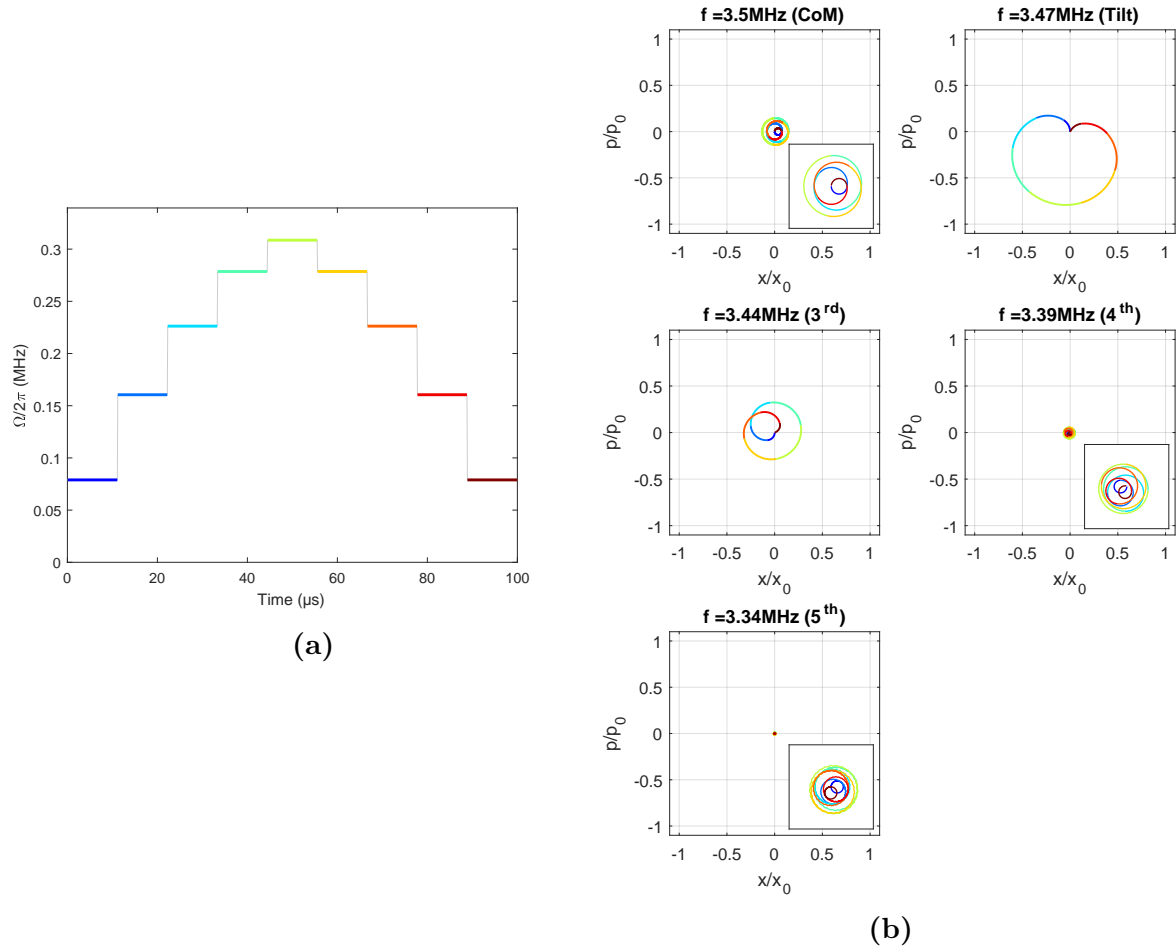


Figure 30: Optimal solution for $\tau_g = 100 \mu\text{s}$ for entangling ion 1 and 2. (a) Rabi frequency levels with a detuning $\mu = 2\pi \cdot 3.4602 \text{ MHz}$. (b) Phasespace diagram of the radial normal modes in z -direction. The color code corresponds to the Rabi levels in (a). The infidelity of this solution is calculated to be $1.8 \cdot 10^{-5}$.

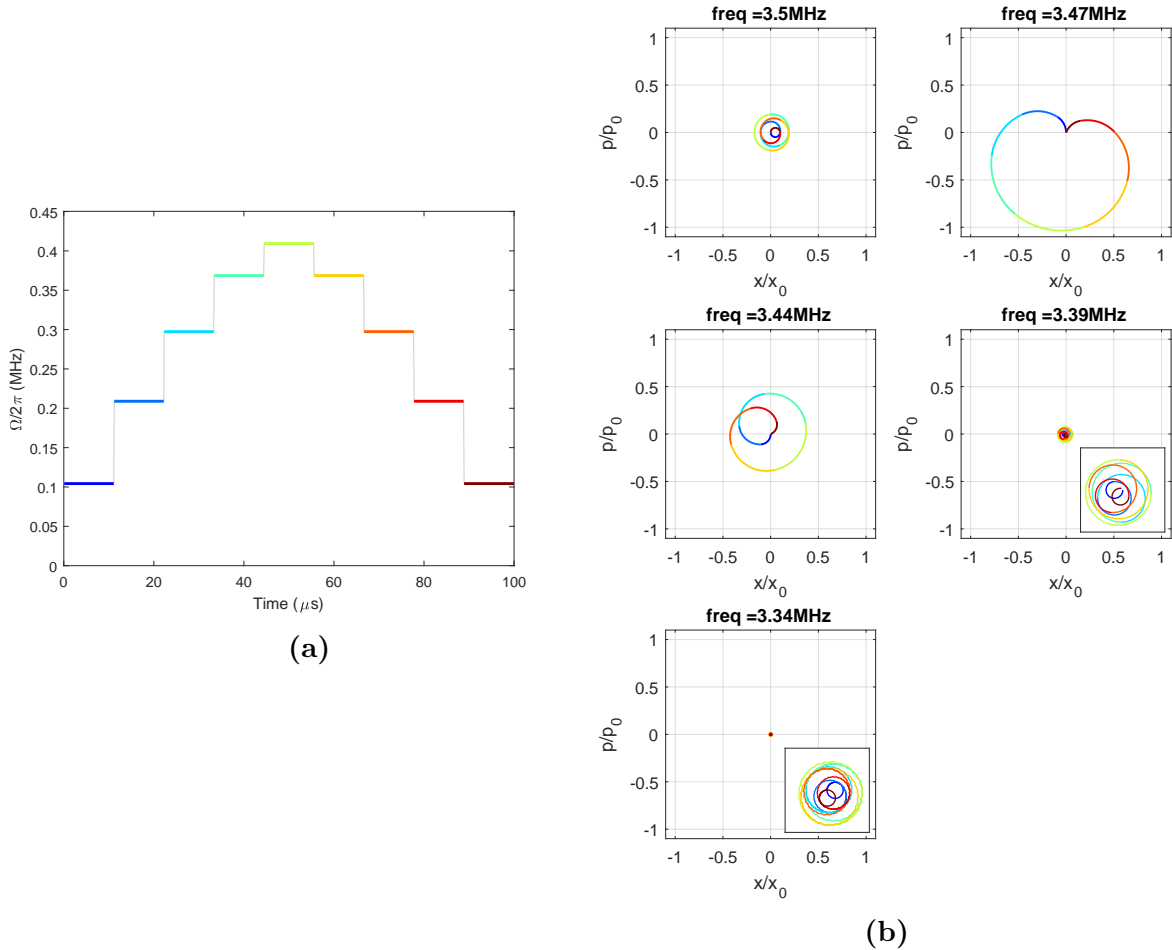


Figure 31: Optimal solution for $\tau_g = 100 \mu s$ for entangling ion 1 and 3. (a) Rabi frequency levels with a detuning $\mu = 2\pi \cdot 3.4600 \text{ MHz}$. (b) Phasespace diagram of the radial normal modes in z -direction. The color code corresponds to the Rabi levels in (a). The infidelity of this solution is calculated to be $1.8 \cdot 10^{-5}$.

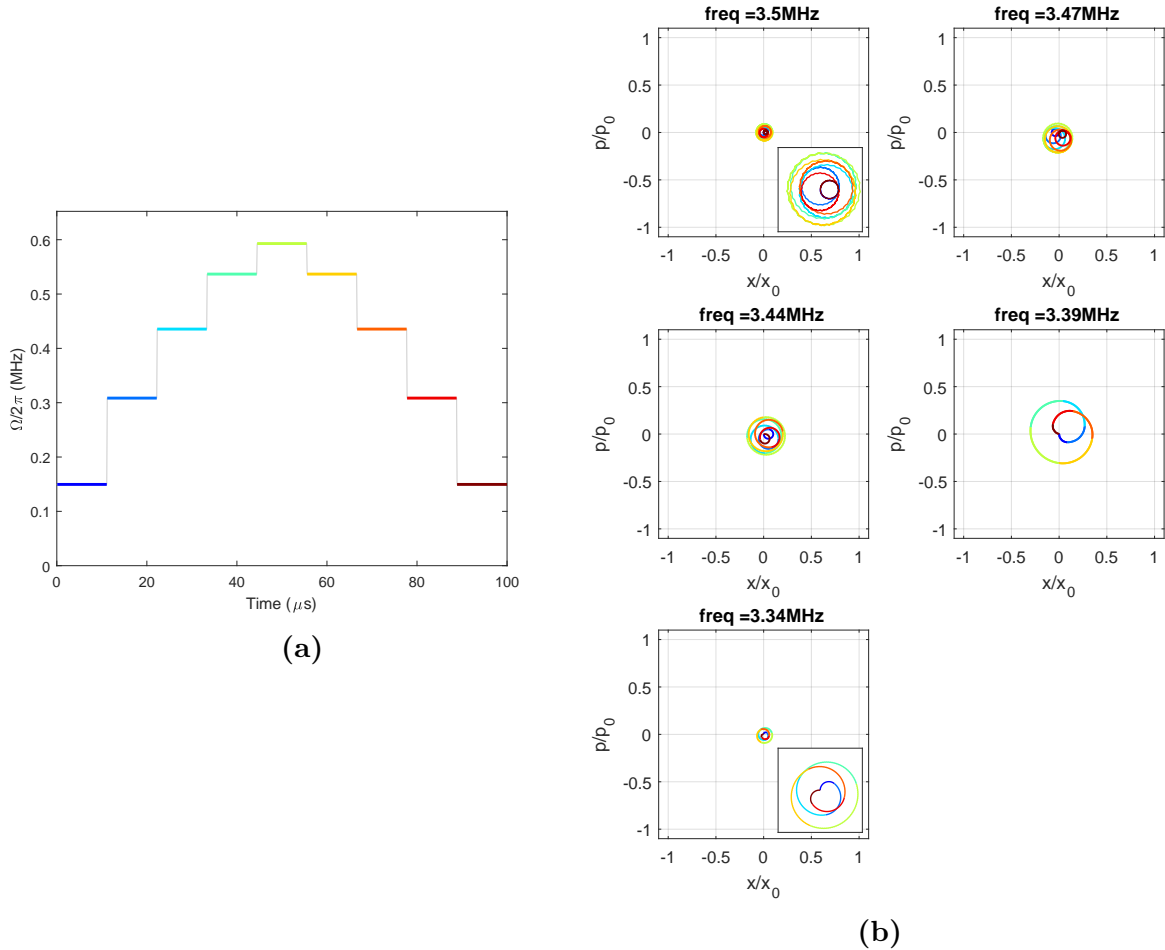


Figure 32: Optimal solution for $\tau_g = 100 \mu\text{s}$ for entangling ion 1 and 4. (a) Rabi frequency levels with a detuning $\mu = 2\pi \cdot 3.3702 \text{ MHz}$. (b) Phasespace diagram of the radial normal modes in z -direction. The color code corresponds to the Rabi levels in (a). The infidelity of this solution is calculated to be $4.3 \cdot 10^{-5}$.

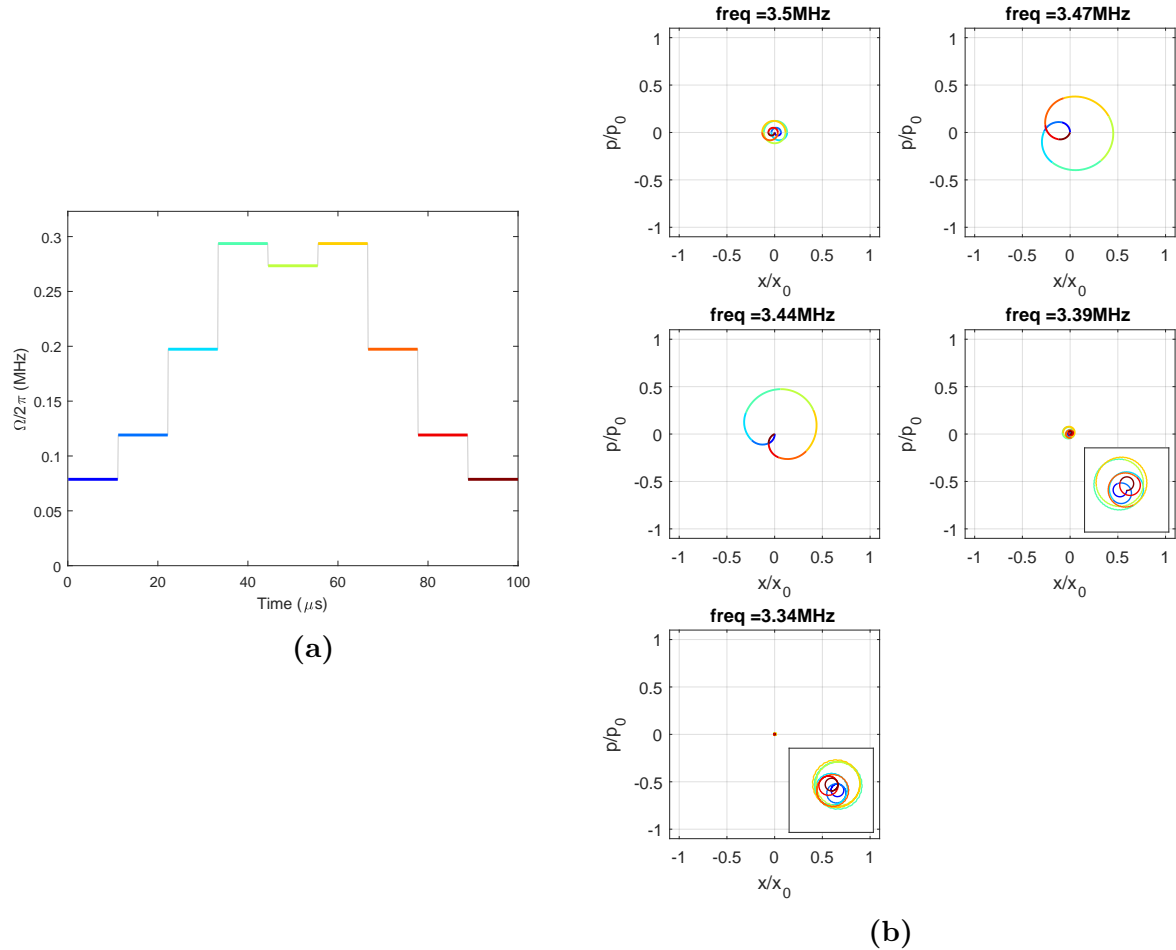


Figure 33: Optimal solution for $\tau_g = 100 \mu s$ for entangling ion 1 and 5. (a) Rabi frequency levels with a detuning $\mu = 2\pi \cdot 3.4550 \text{ MHz}$. (b) Phasespace diagram of the radial normal modes in z -direction. The color code corresponds to the Rabi levels in (a). The infidelity of this solution is calculated to be $4.2 \cdot 10^{-5}$.

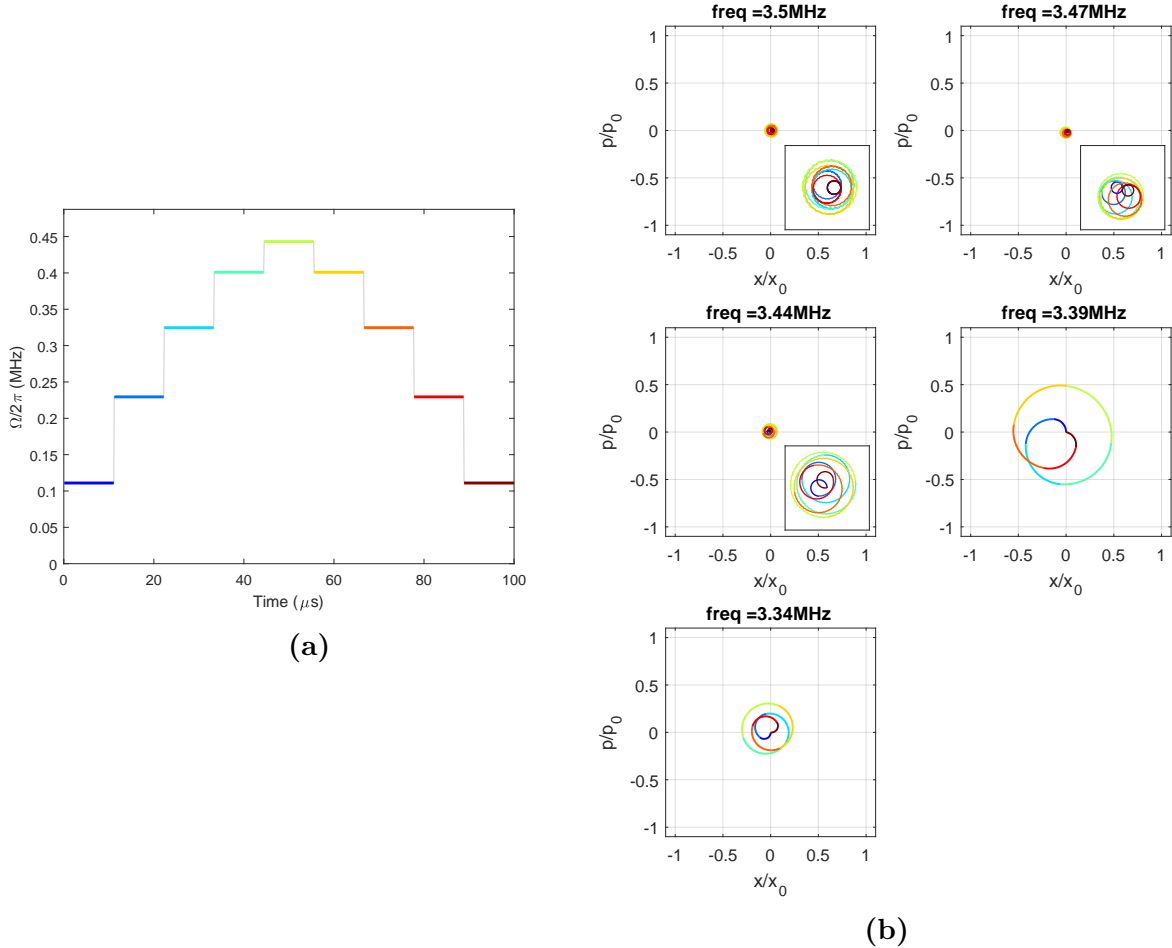


Figure 34: Optimal solution for $\tau_g = 100 \mu s$ for entangling ion 2 and 3. (a) Rabi frequency levels with a detuning $\mu = 2\pi \cdot 3.3702 \text{ MHz}$. (b) Phasespace diagram of the radial normal modes in z -direction. The color code corresponds to the Rabi levels in (a). The infidelity of this solution is calculated to be $1.8 \cdot 10^{-5}$.

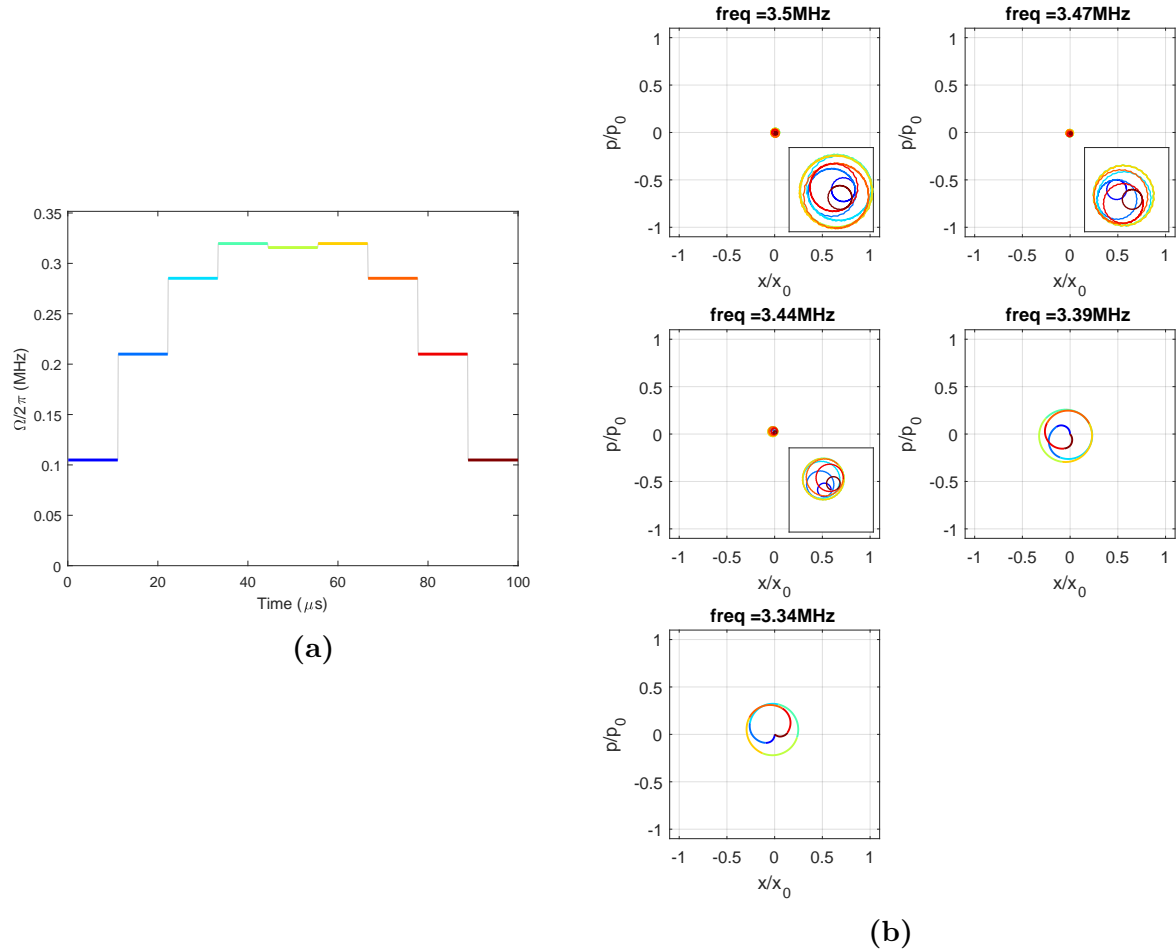


Figure 35: Optimal solution for $\tau_g = 100 \mu s$ for entangling ion 2 and 4. (a) Rabi frequency levels with a detuning $\mu = 2\pi \cdot 3.3612 \text{ MHz}$. (b) Phasespace diagram of the radial normal modes in z -direction. The color code corresponds to the Rabi levels in (a). The infidelity of this solution is calculated to be $3.7 \cdot 10^{-5}$.

A.2. Solutions for a gate time of $\tau_g = 80 \mu\text{s}$

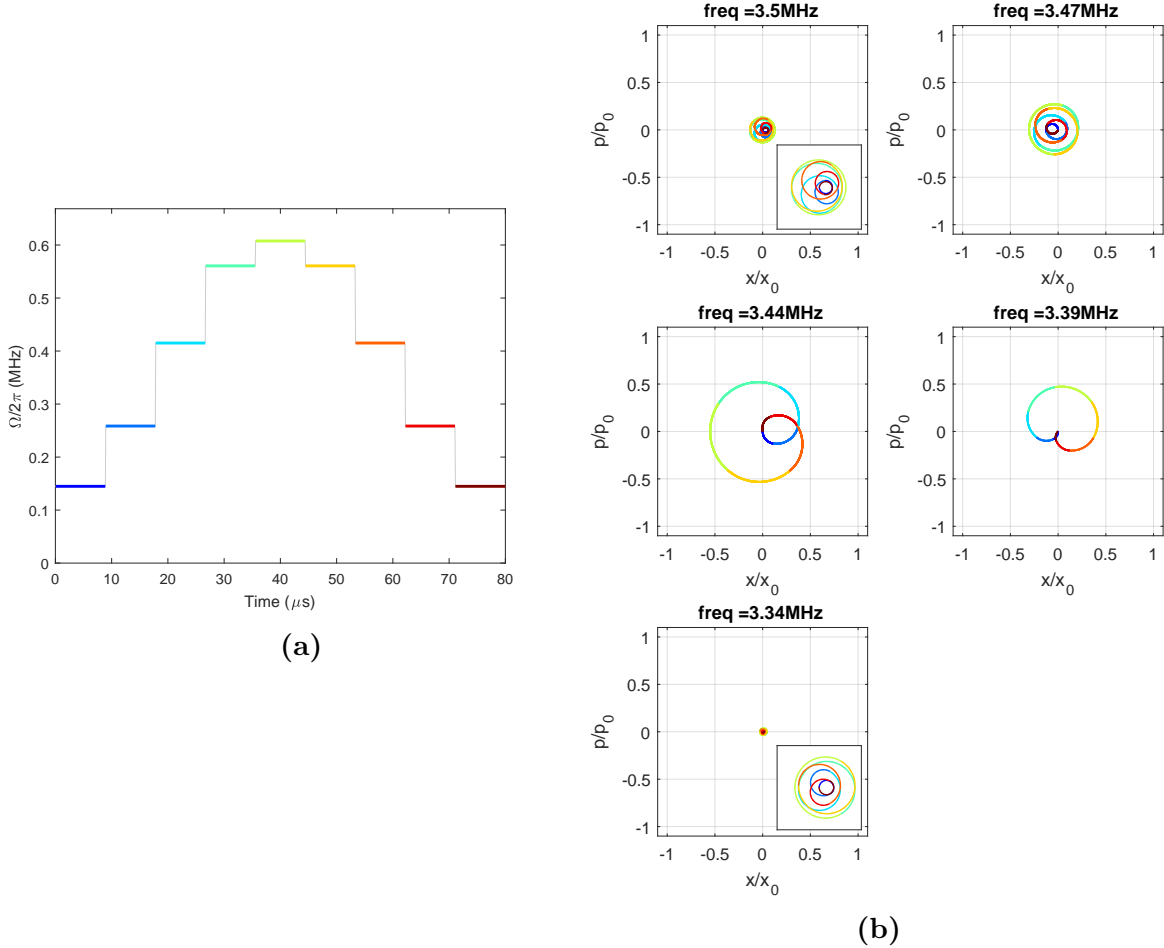


Figure 36: Optimal solution for $\tau_g = 80 \mu\text{s}$ for entangling ion 1 and 2. (a) Rabi frequency levels with a detuning $\mu = 2\pi \cdot 3.4126 \text{ MHz}$. (b) Phasespace diagram of the radial normal modes in z -direction. The color code corresponds to the Rabi levels in (a). The infidelity of this solution is calculated to be $5.3 \cdot 10^{-5}$.

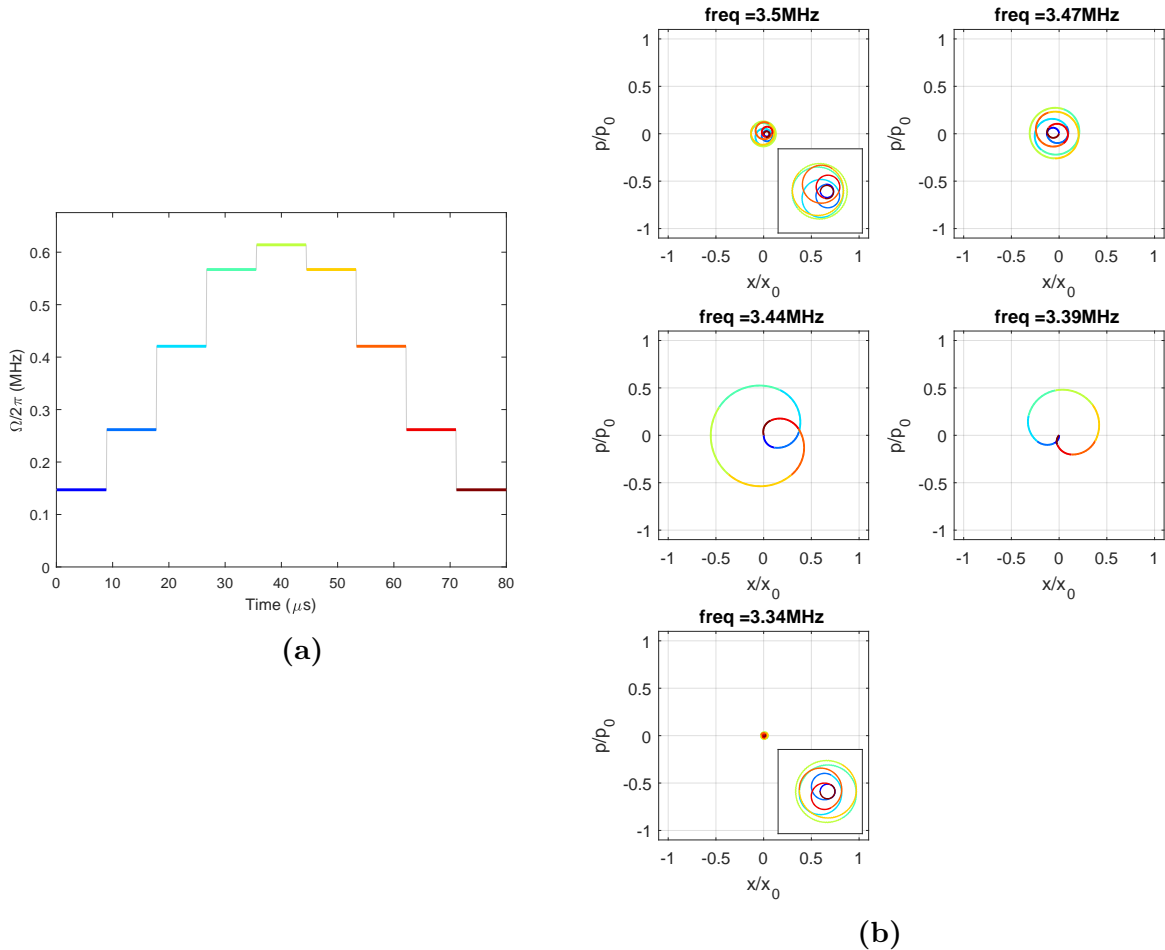


Figure 37: Optimal solution for $\tau_g = 80 \mu s$ for entangling ion 1 and 3. (a) Rabi frequency levels with a detuning $\mu = 2\pi \cdot 3.4126$ MHz. (b) Phasespace diagram of the radial normal modes in z -direction. The color code corresponds to the Rabi levels in (a). The infidelity of this solution is calculated to be $7.9 \cdot 10^{-5}$.

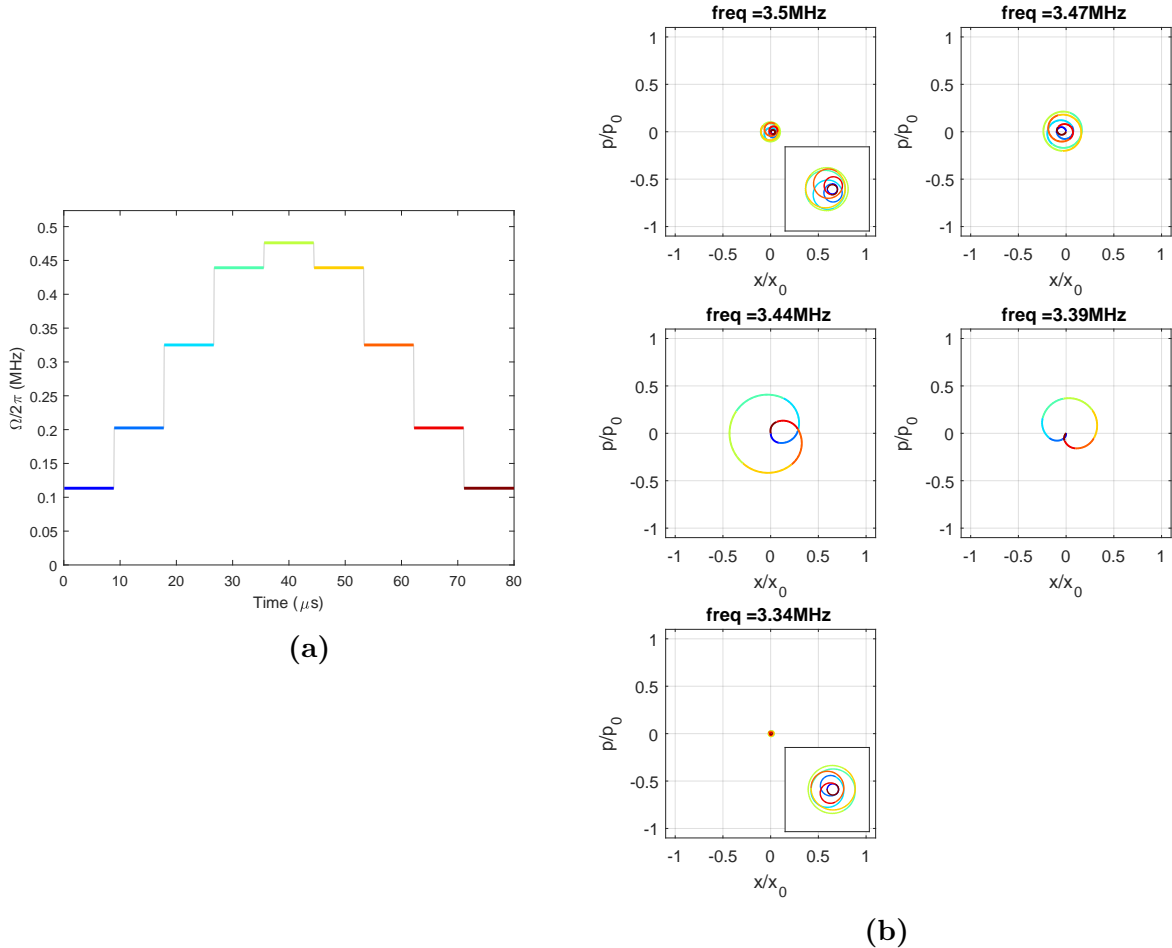


Figure 38: Optimal solution for $\tau_g = 80 \mu s$ for entangling ion 1 and 4. (a) Rabi frequency levels with a detuning $\mu = 2\pi \cdot 3.4126$ MHz. (b) Phasespace diagram of the radial normal modes in z -direction. The color code corresponds to the Rabi levels in (a). The infidelity of this solution is calculated to be $3.2 \cdot 10^{-5}$.

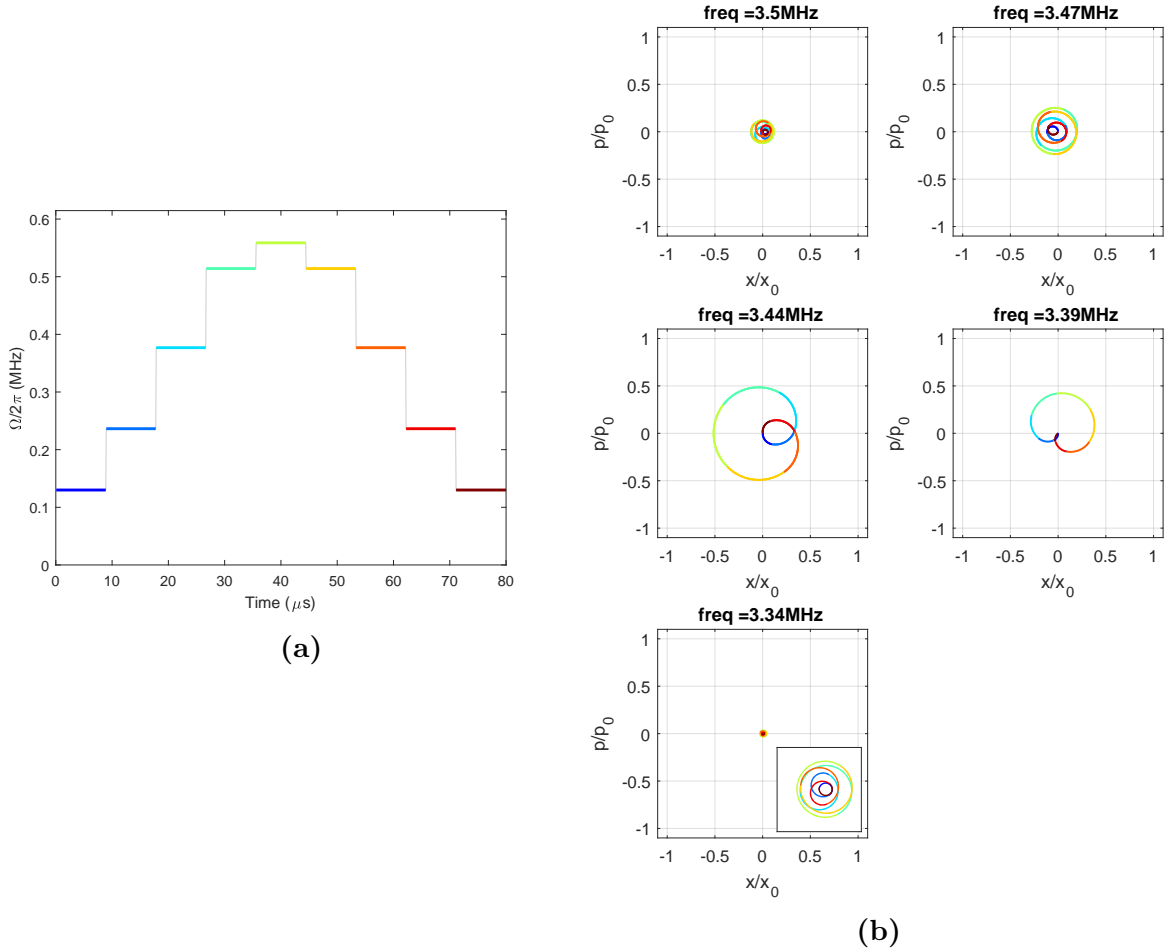


Figure 39: Optimal solution for $\tau_g = 80 \mu s$ for entangling ion 1 and 5. (a) Rabi frequency levels with a detuning $\mu = 2\pi \cdot 3.4129$ MHz. (b) Phasespace diagram of the radial normal modes in z -direction. The color code corresponds to the Rabi levels in (a). The infidelity of this solution is calculated to be $5.0 \cdot 10^{-5}$.

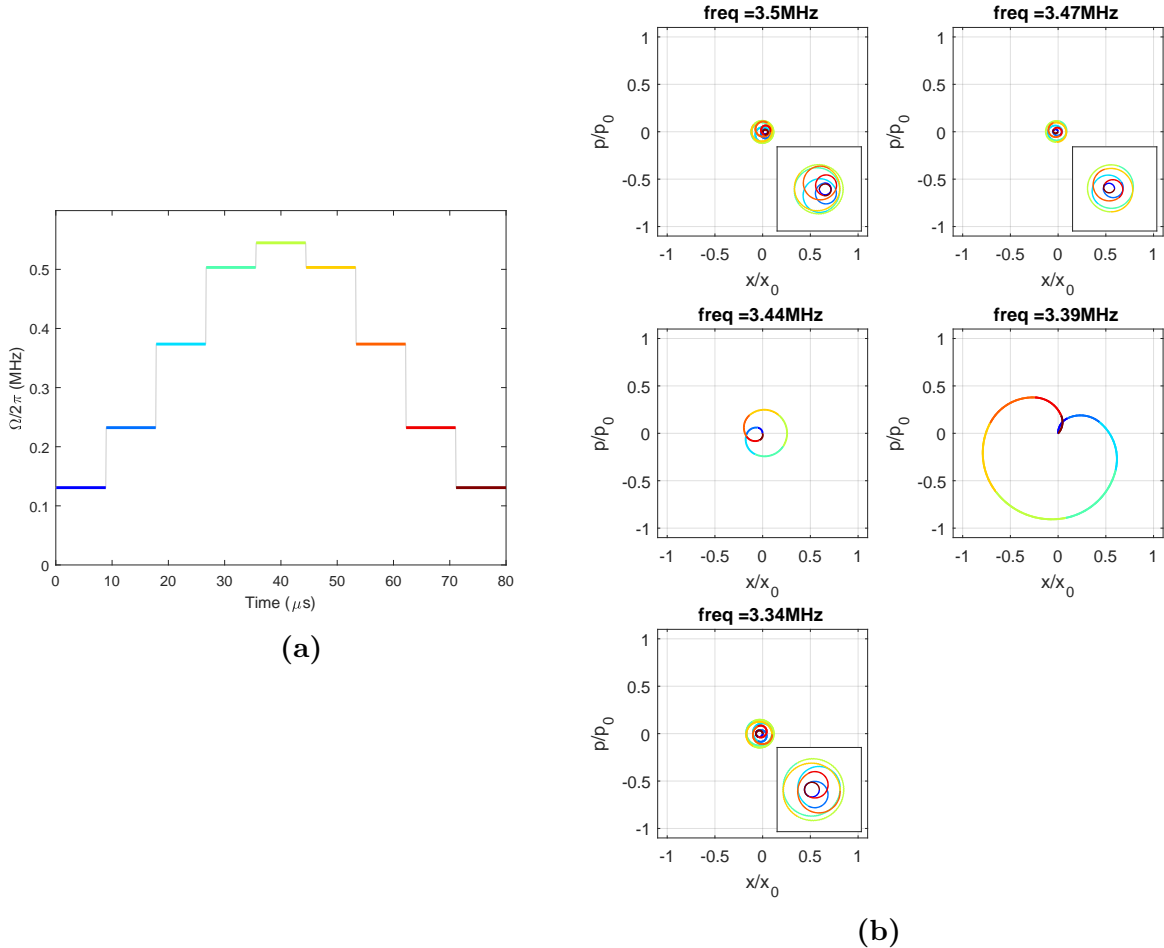


Figure 40: Optimal solution for $\tau_g = 80 \mu s$ for entangling ion 2 and 3. (a) Rabi frequency levels with a detuning $\mu = 2\pi \cdot 3.4126$ MHz. (b) Phasespace diagram of the radial normal modes in z -direction. The color code corresponds to the Rabi levels in (a). The infidelity of this solution is calculated to be $5.0 \cdot 10^{-5}$.

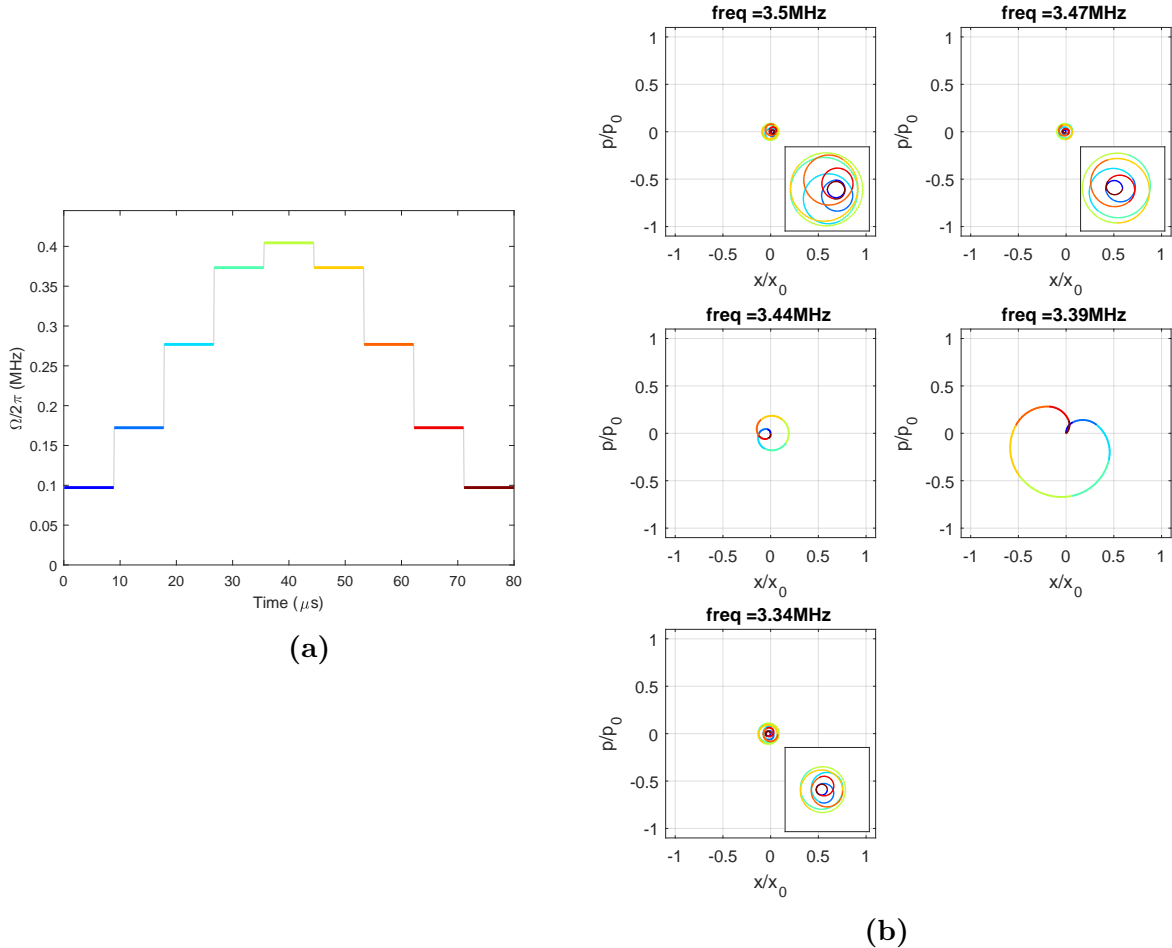


Figure 41: Optimal solution for $\tau_g = 80 \mu s$ for entangling ion 2 and 4. (a) Rabi frequency levels with a detuning $\mu = 2\pi \cdot 3.4126$ MHz. (b) Phasespace diagram of the radial normal modes in z -direction. The color code corresponds to the Rabi levels in (a). The infidelity of this solution is calculated to be $1.7 \cdot 10^{-5}$.

A.3. Solutions for a gate time of $\tau_g = 60 \mu\text{s}$

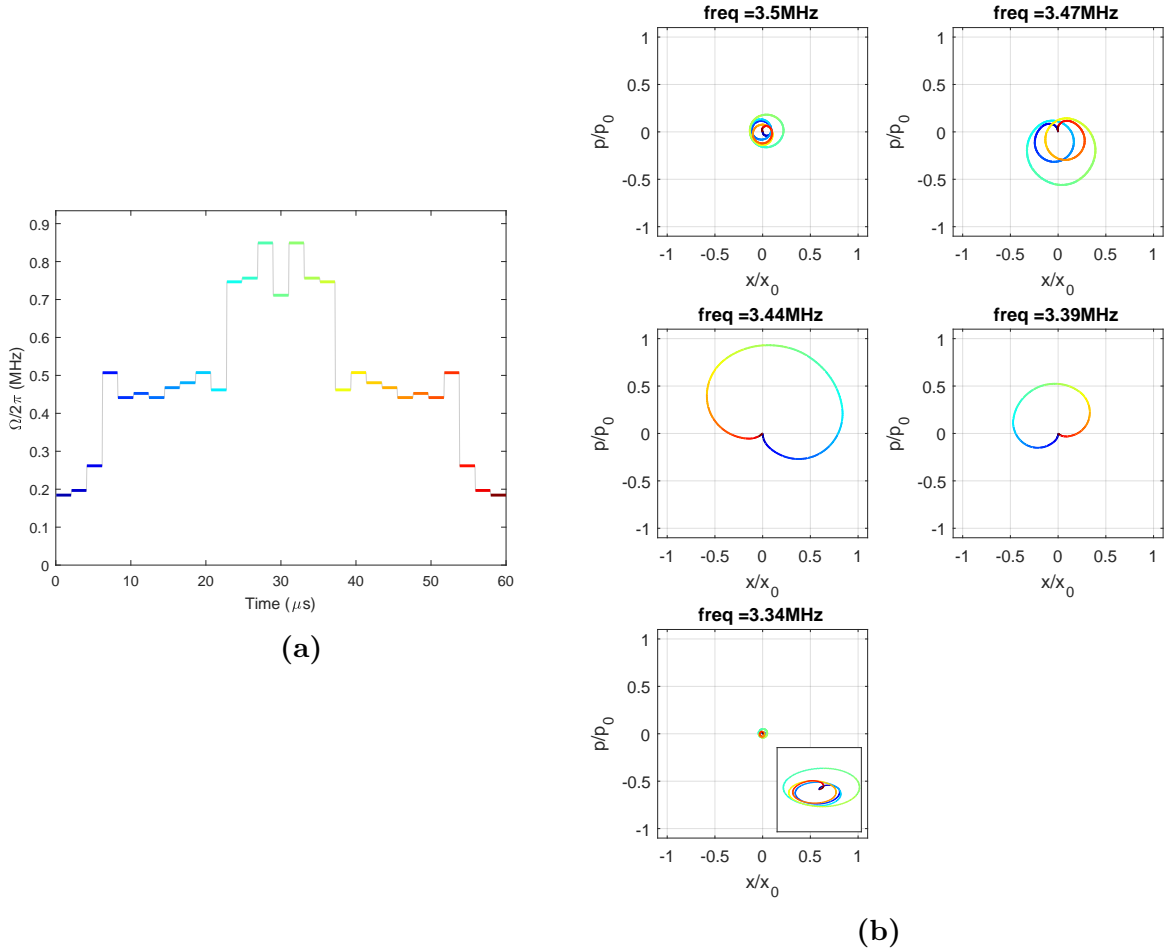


Figure 42: Optimal solution for $\tau_g = 60 \mu\text{s}$ for entangling ion 1 and 2. (a) Rabi frequency levels with a detuning $\mu = 2\pi \cdot 3.4153 \text{ MHz}$. (b) Phasespace diagram of the radial normal modes in z -direction. The color code corresponds to the Rabi levels in (a). The infidelity of this solution is calculated to be $2.3 \cdot 10^{-5}$.

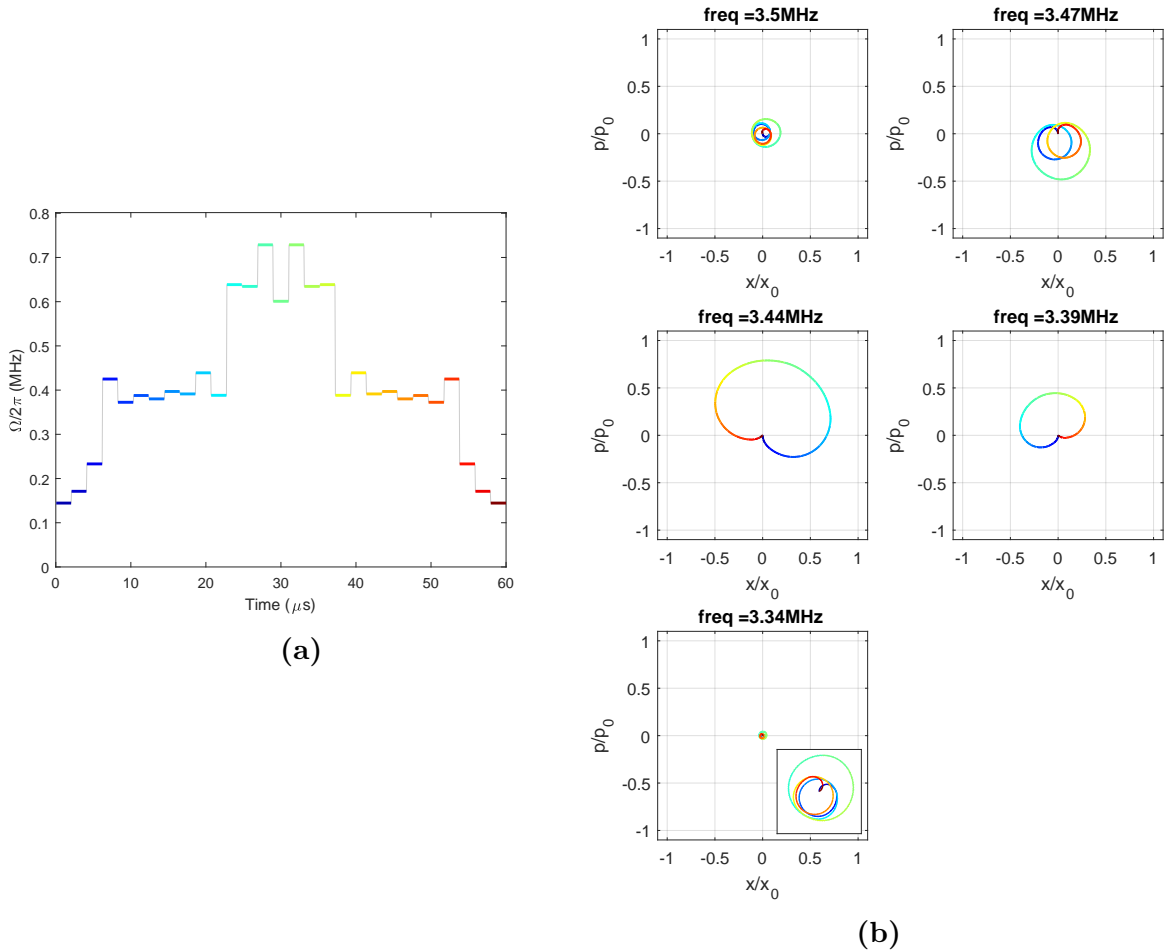


Figure 43: Optimal solution for $\tau_g = 60 \mu s$ for entangling ion 1 and 3. (a) Rabi frequency levels with a detuning $\mu = 2\pi \cdot 3.4153$ MHz. (b) Phasespace diagram of the radial normal modes in z -direction. The color code corresponds to the Rabi levels in (a). The infidelity of this solution is calculated to be $4.9 \cdot 10^{-6}$.

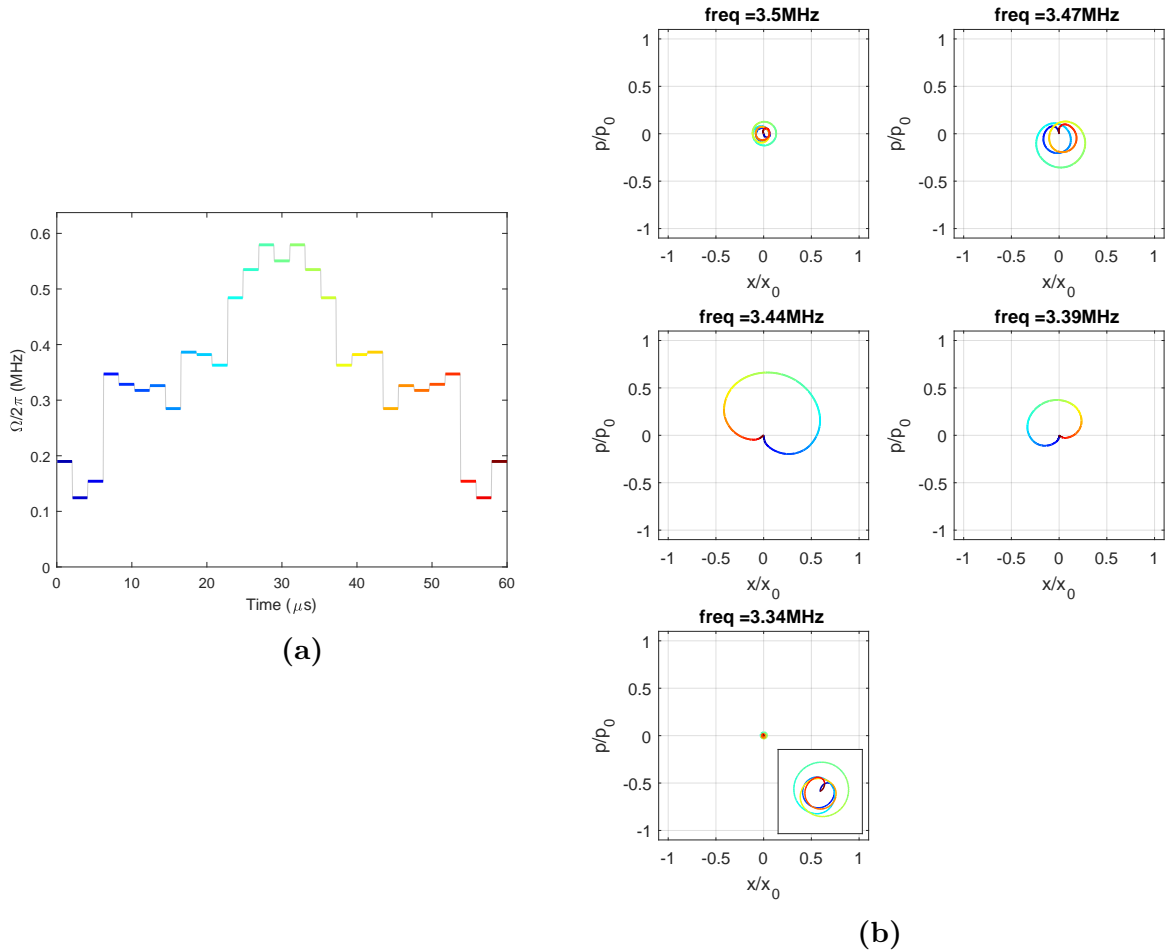


Figure 44: Optimal solution for $\tau_g = 60 \mu s$ for entangling ion 1 and 4. (a) Rabi frequency levels with a detuning $\mu = 2\pi \cdot 3.4153$ MHz. (b) Phasespace diagram of the radial normal modes in z -direction. The color code corresponds to the Rabi levels in (a). The infidelity of this solution is calculated to be $1.0 \cdot 10^{-5}$.

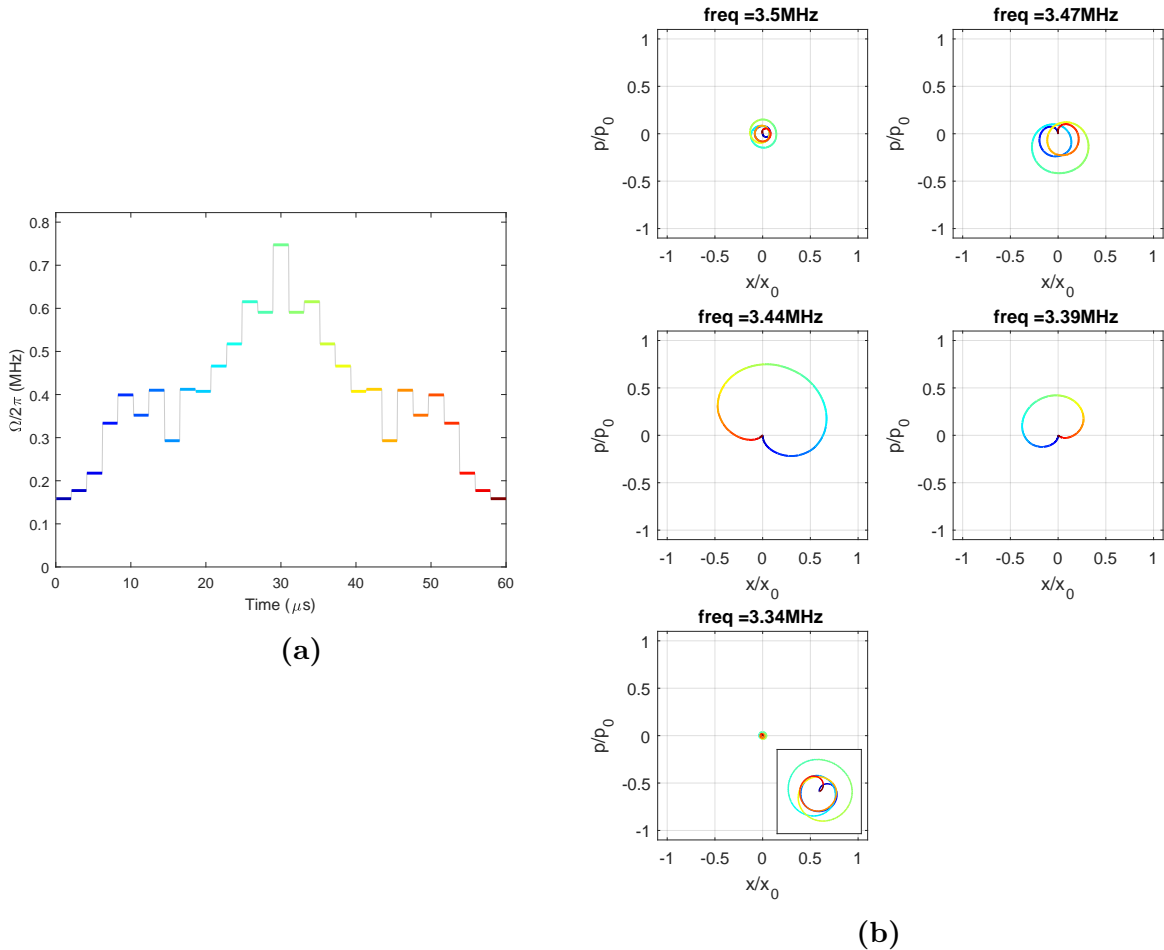


Figure 45: Optimal solution for $\tau_g = 60 \mu s$ for entangling ion 1 and 5. (a) Rabi frequency levels with a detuning $\mu = 2\pi \cdot 3.4153$ MHz. (b) Phasespace diagram of the radial normal modes in z -direction. The color code corresponds to the Rabi levels in (a). The infidelity of this solution is calculated to be $5.5 \cdot 10^{-6}$.

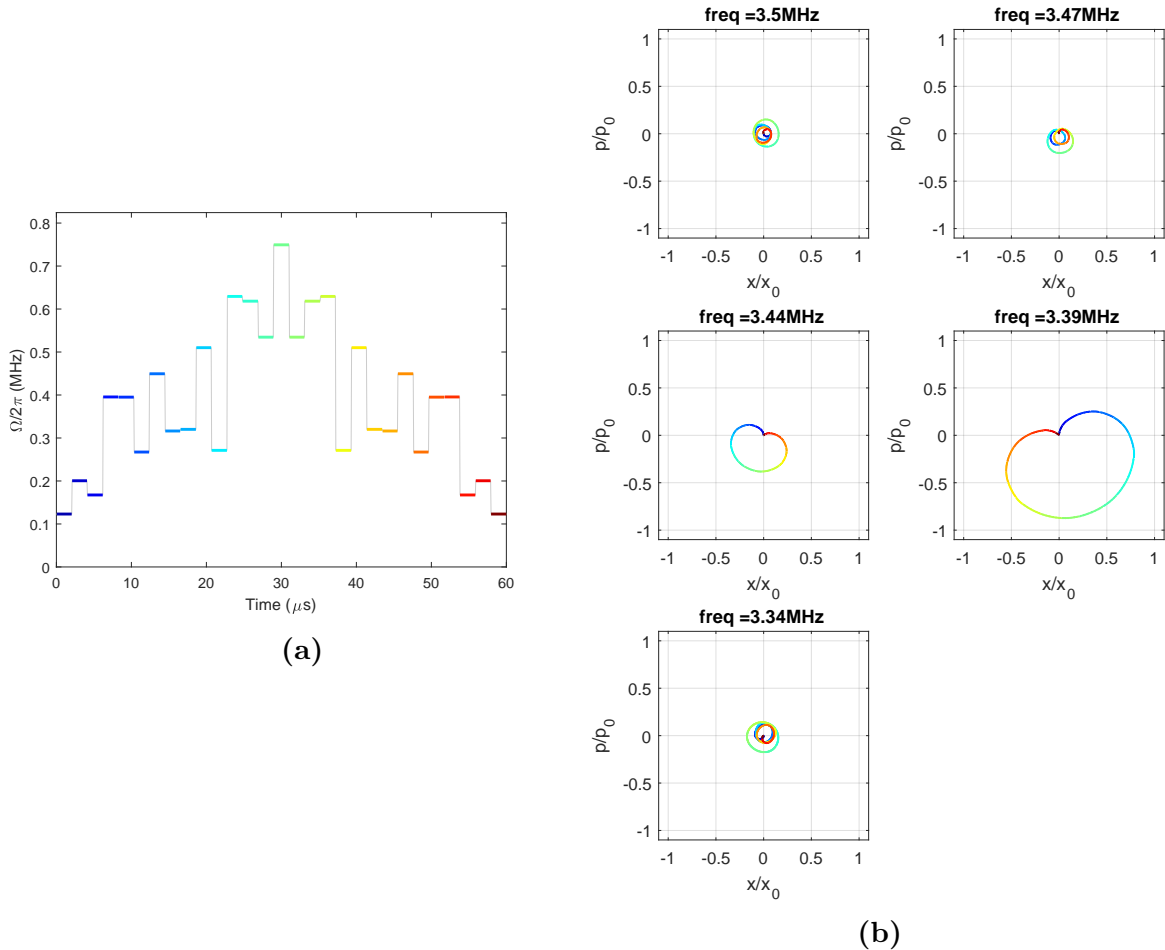


Figure 46: Optimal solution for $\tau_g = 60 \mu s$ for entangling ion 2 and 3. (a) Rabi frequency levels with a detuning $\mu = 2\pi \cdot 3.4153$ MHz. (b) Phasespace diagram of the radial normal modes in z -direction. The color code corresponds to the Rabi levels in (a). The infidelity of this solution is calculated to be $4.7 \cdot 10^{-5}$.

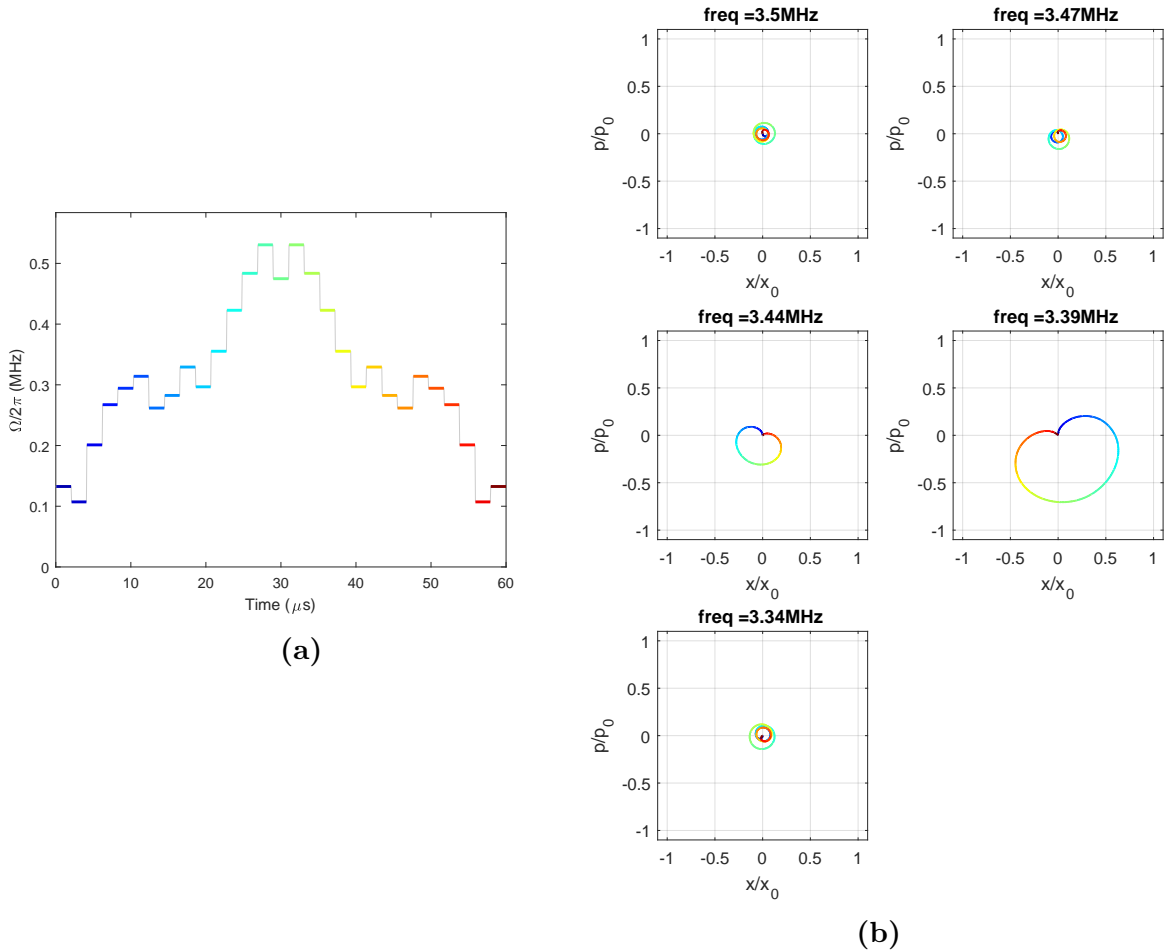


Figure 47: Optimal solution for $\tau_g = 60 \mu s$ for entangling ion 2 and 4. (a) Rabi frequency levels with a detuning $\mu = 2\pi \cdot 3.4153$ MHz. (b) Phasespace diagram of the radial normal modes in z -direction. The color code corresponds to the Rabi levels in (a). The infidelity of this solution is calculated to be $2.0 \cdot 10^{-5}$.

A.4. Solutions for a gate time of $\tau_g = 40 \mu\text{s}$

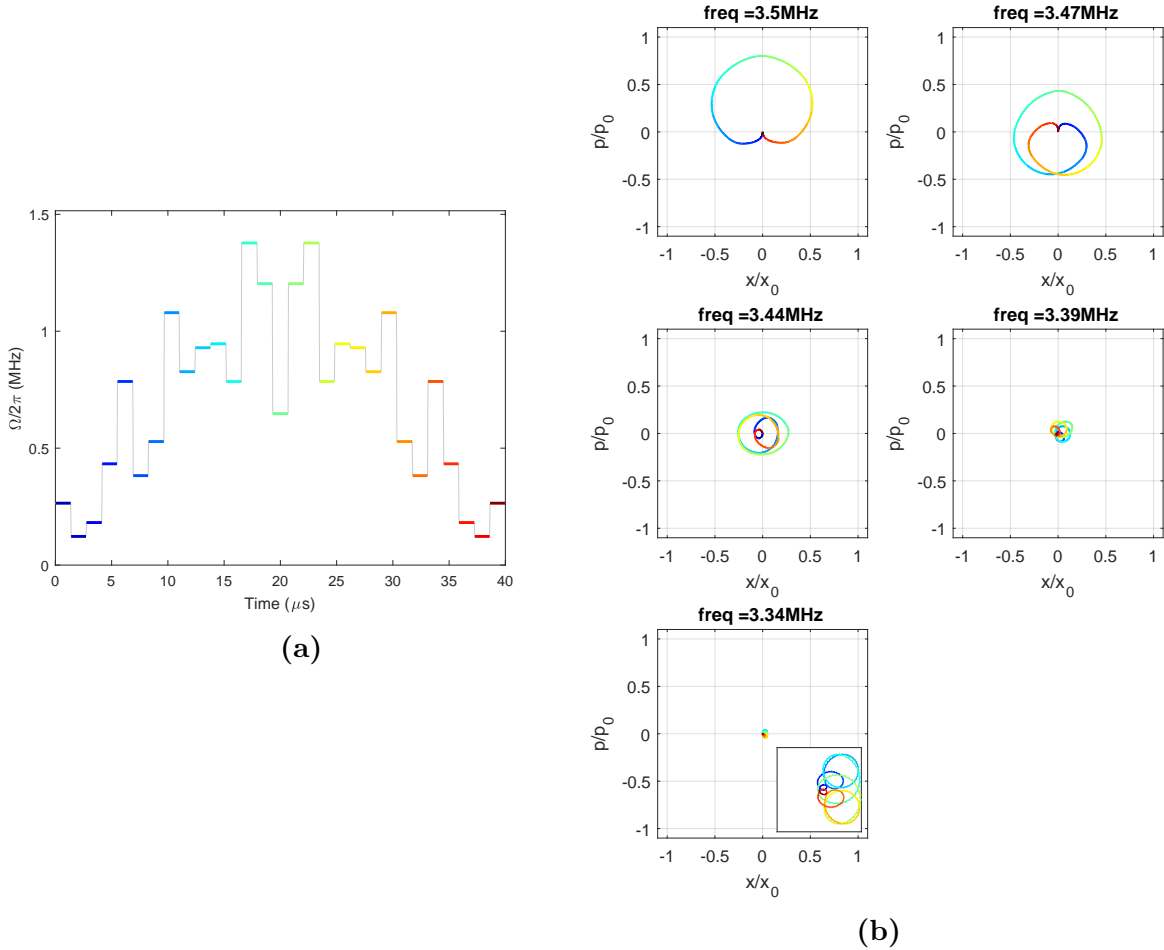


Figure 48: Optimal solution for $\tau_g = 40 \mu\text{s}$ for entangling ion 1 and 2. (a) Rabi frequency levels with a detuning $\mu = 2\pi \cdot 3.5375 \text{ MHz}$. (b) Phasespace diagram of the radial normal modes in z -direction. The color code corresponds to the Rabi levels in (a). The infidelity of this solution is calculated to be $4.6 \cdot 10^{-4}$.

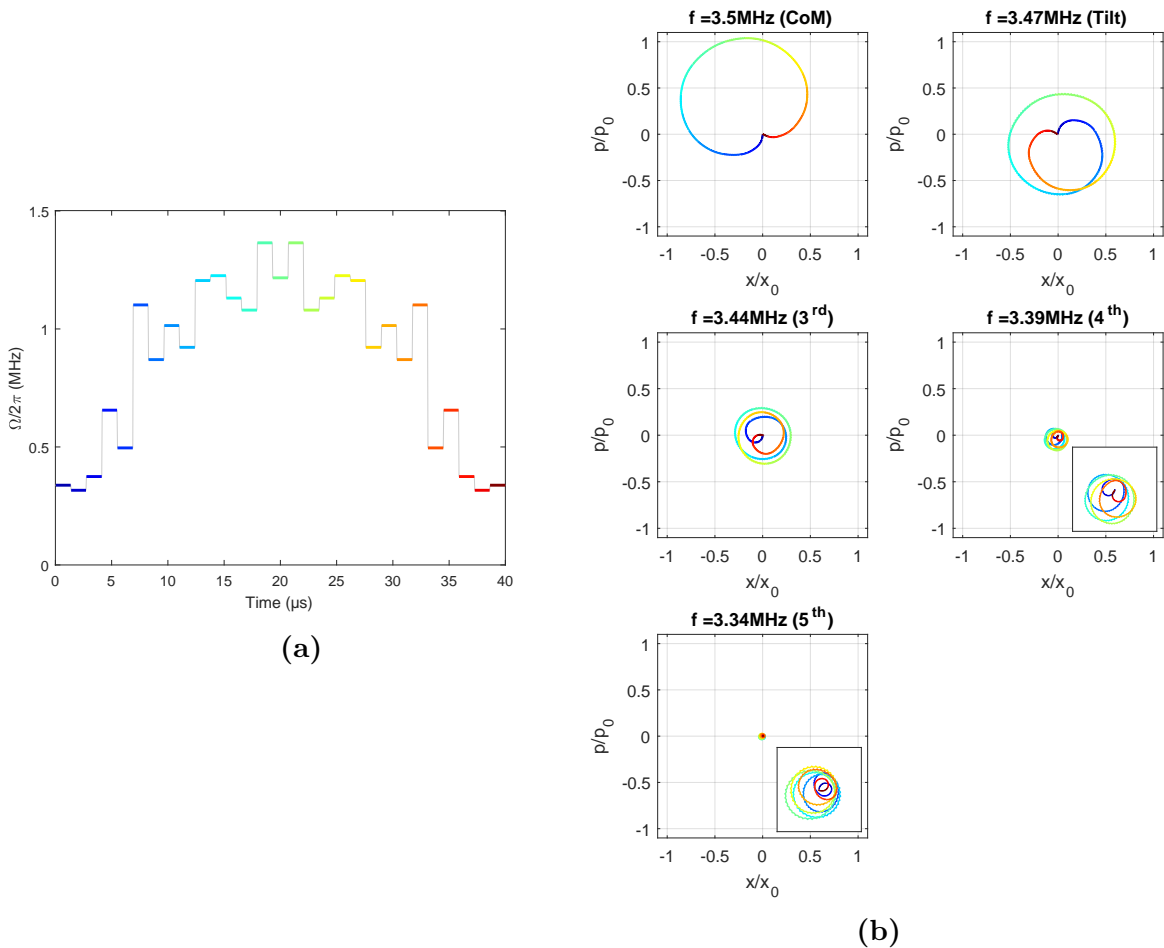


Figure 49: Optimal solution for $\tau_g = 40 \mu\text{s}$ for entangling ion 1 and 3. (a) Rabi frequency levels with a detuning $\mu = 2\pi \cdot 3.5336 \text{ MHz}$. (b) Phasespace diagram of the radial normal modes in z -direction. The color code corresponds to the Rabi levels in (a). The infidelity of this solution is calculated to be $7.3 \cdot 10^{-4}$.

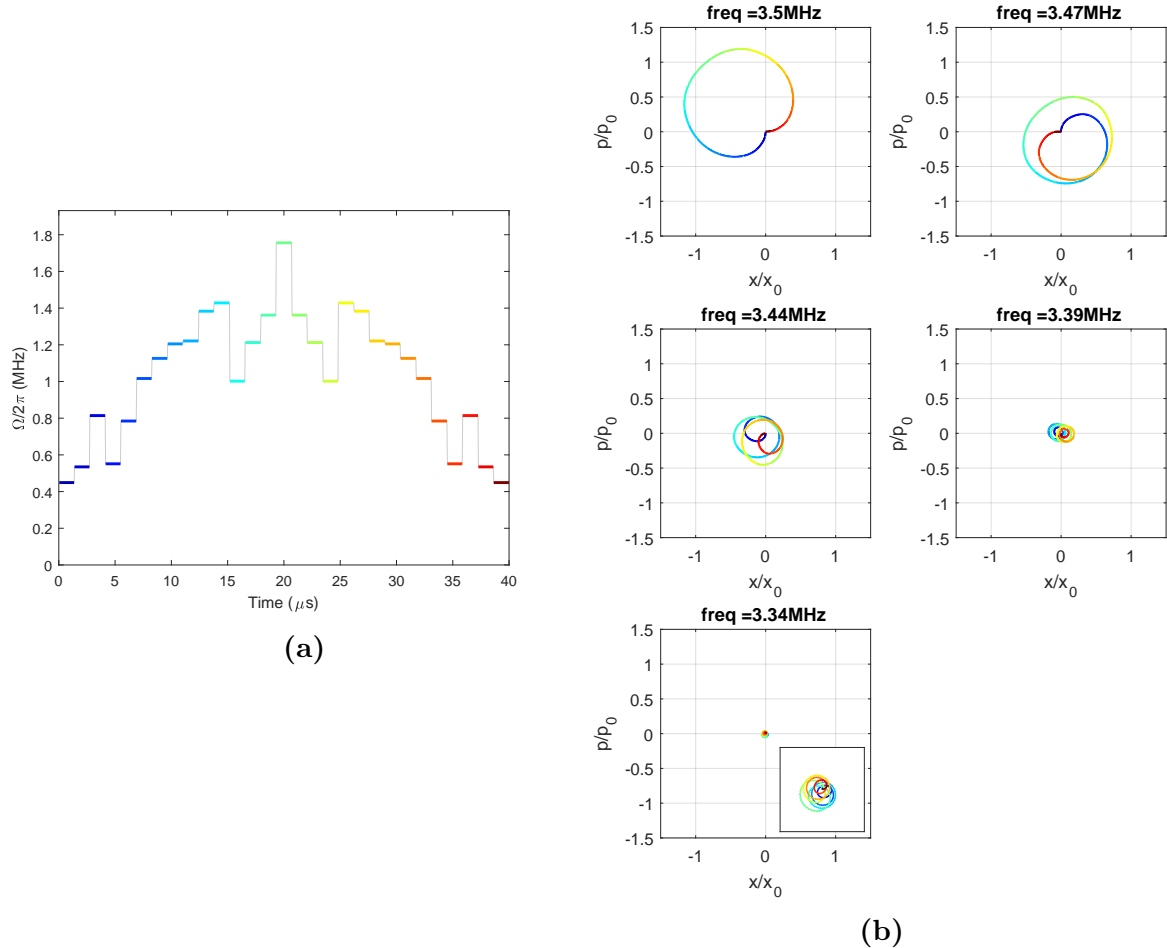


Figure 50: Optimal solution for $\tau_g = 40 \mu\text{s}$ for entangling ion 1 and 4. (a) Rabi frequency levels with a detuning $\mu = 2\pi \cdot 3.5315 \text{ MHz}$. (b) Phasespace diagram of the radial normal modes in z -direction. The color code corresponds to the Rabi levels in (a). The infidelity of this solution is calculated to be $6.3 \cdot 10^{-4}$.

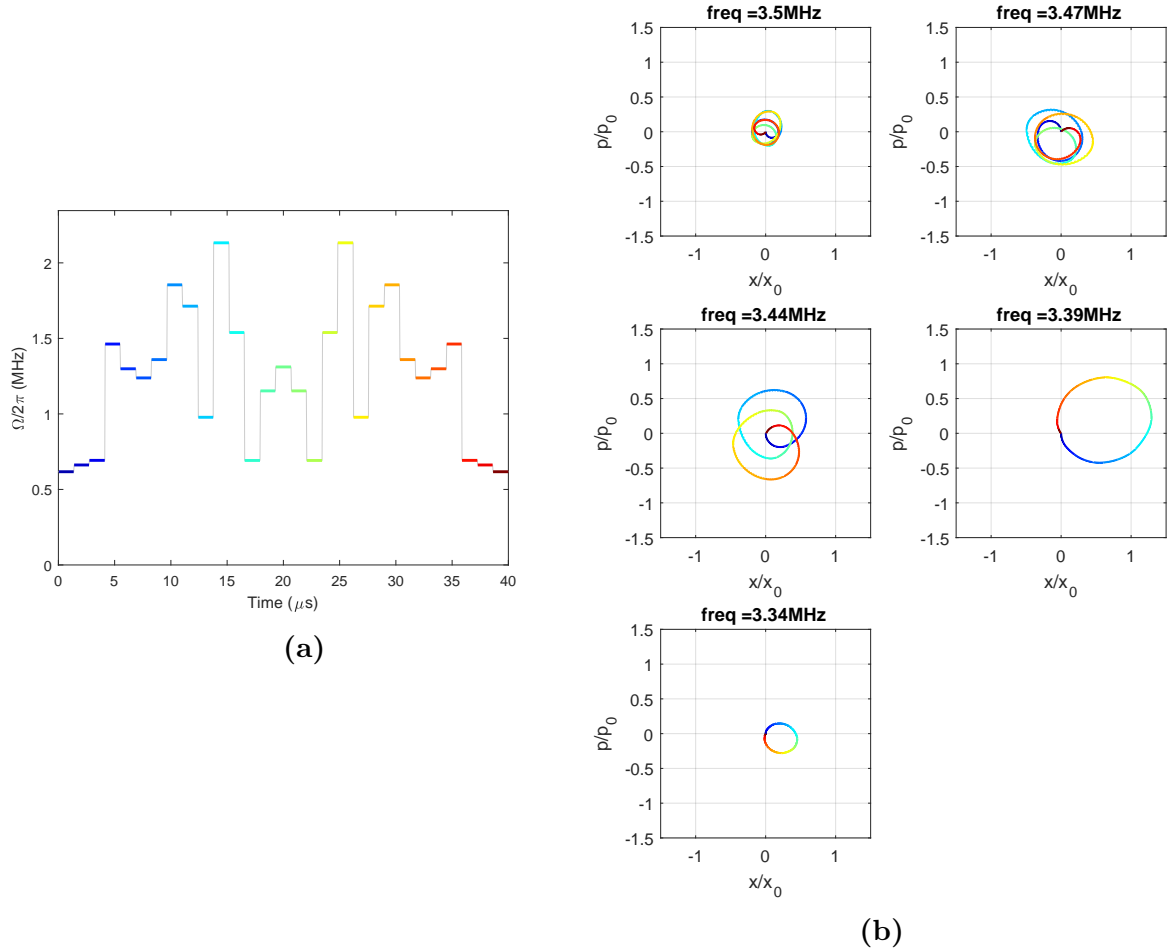


Figure 51: Optimal solution for $\tau_g = 40 \mu s$ for entangling ion 1 and 5. (a) Rabi frequency levels with a detuning $\mu = 2\pi \cdot 3.3649$ MHz. (b) Phasespace diagram of the radial normal modes in z -direction. The color code corresponds to the Rabi levels in (a). The infidelity of this solution is calculated to be $5.6 \cdot 10^{-4}$.

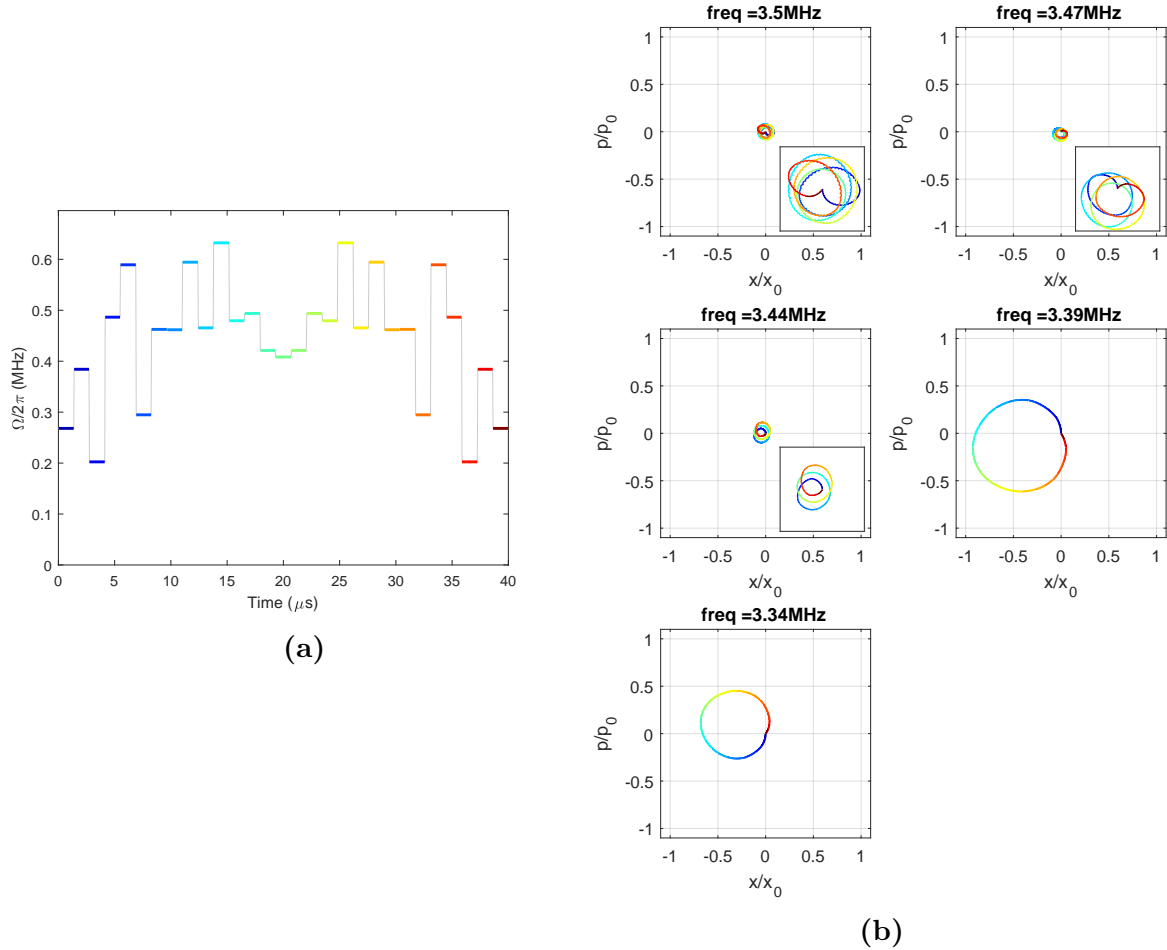


Figure 52: Optimal solution for $\tau_g = 40 \mu s$ for entangling ion 2 and 3. (a) Rabi frequency levels with a detuning $\mu = 2\pi \cdot 3.3650$ MHz. (b) Phasespace diagram of the radial normal modes in z -direction. The color code corresponds to the Rabi levels in (a). The infidelity of this solution is calculated to be $3.4 \cdot 10^{-4}$.

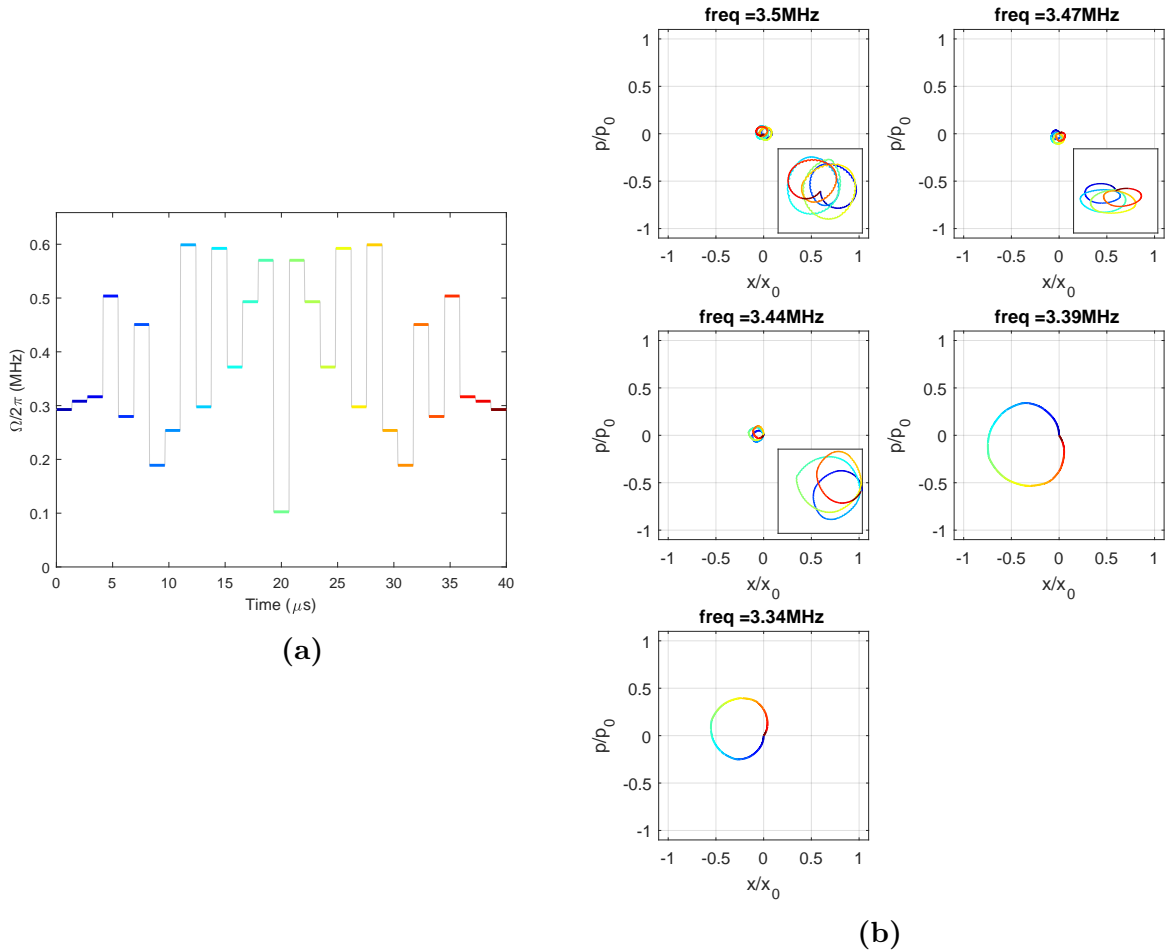


Figure 53: Optimal solution for $\tau_g = 40 \mu s$ for entangling ion 2 and 4. (a) Rabi frequency levels with a detuning $\mu = 2\pi \cdot 3.3649$ MHz. (b) Phasespace diagram of the radial normal modes in z -direction. The color code corresponds to the Rabi levels in (a). The infidelity of this solution is calculated to be $1.1 \cdot 10^{-4}$.

References

- [1] Michael A. Nielsen and Isaac L. Chuang. *Quantum Computation and Quantum Information*. Cambridge University Press, 2000.
- [2] Alexandre Blais, Ren-Shou Huang, Andreas Wallraff, S. M. Girvin, and R. J. Schoelkopf. Cavity quantum electrodynamics for superconducting electrical circuits: An architecture for quantum computation. *Phys. Rev. A*, 69:062320, Jun 2004.
- [3] D. Leibfried, R. Blatt, C. Monroe, and D. Wineland. Quantum dynamics of single trapped ions. *Rev. Mod. Phys.*, 75:281–324, Mar 2003.
- [4] R. Hanson, L. P. Kouwenhoven, J. R. Petta, S. Tarucha, and L. M. K. Vandersypen. Spins in few-electron quantum dots. *Rev. Mod. Phys.*, 79:1217–1265, Oct 2007.
- [5] F. Jelezko and J. Wrachtrup. Single defect centres in diamond: A review. *physica status solidi (a)*, 203(13):3207–3225.
- [6] D. J. Wineland, C. Monroe, W. M. Itano, D. Leibfried, B. E. King, and D. M. Meekhof. Experimental issues in coherent quantum-state manipulation of trapped atomic ions. *arXiv e-prints*, pages quant-ph/9710025, Oct 1997.
- [7] D. Kielpinski, C. Monroe, and D. J. Wineland. Architecture for a large-scale ion-trap quantum computer. *Nature*, 417(6890):709–711, 2002.
- [8] Karan K. Mehta, Chi Zhang, Stefanie Miller, and Jonathan P. Home. Towards fast and scalable trapped-ion quantum logic with integrated photonics. In *Proc. SPIE 10933*, 2019.
- [9] Karan K. Mehta, Colin D. Bruzewicz, Robert Mcconnell, Rajeev J. Ram, Jeremy M. Sage, and John Chiaverini. Integrated optical addressing of an ion qubit. *Nat. Nanotechnol.*, 11(12):1066–1070, 2016.
- [10] F.G. Major, V.N. Gheorghe, and G. Werth. *Charged Particle Traps*, volume 37 of *Springer Series on Atomic, Optical, and Plasma Physics*. Springer-Verlag, Berlin/Heidelberg, 2005.
- [11] Cornelius Hempel, Christine Maier, Jonathan Romero, Jarrod McClean, Thomas Monz, Heng Shen, Petar Jurcevic, Ben P. Lanyon, Peter Love, Ryan Babbush, Alán Aspuru-Guzik, Rainer Blatt, and Christian F. Roos. Quantum chemistry calculations on a trapped-ion quantum simulator. *Phys. Rev. X*, 8:031022, Jul 2018.
- [12] J. Chiaverini, R. B. Blakestad, J. Britton, J. D. Jost, C. Langer, D. Leibfried, R. Ozeri, and D. J. Wineland. Surface-Electrode Architecture for Ion-Trap Quantum Information Processing. *arXiv e-prints*, pages quant-ph/0501147, Jan 2005.

- [13] P. J. Lee, K. A. Brickman, L. Deslauriers, P. C. Haljan, L. M. Duan, and C. Monroe. Phase control of trapped ion quantum gates. *J. Opt. B Quantum Semiclassical Opt.*, 7(10), 2005.
- [14] Klaus Mølmer and Anders Sørensen. Multiparticle entanglement of hot trapped ions. *Phys. Rev. Lett.*, 82:1835–1838, Mar 1999.
- [15] D.F.V. James. Quantum dynamics of cold trapped ions with application to quantum computation. *Applied Physics B*, 66(2):181–190, Feb 1998.
- [16] C. E. Langer. *High fidelity quantum information processing with trapped ions*. PhD thesis, University of Colorado at Boulder, 2006.
- [17] S. Debnath. *A Programmable Five Qubit Quantum Computer Using Trapped Atomic Ions*. PhD thesis, University of Maryland, 2016.
- [18] Anders Sørensen and Klaus Mølmer. Entanglement and quantum computation with ions in thermal motion. *Phys. Rev. A*, 62:022311, Jul 2000.
- [19] S. Blanes, F. Casas, J.A. Oteo, and J. Ros. The magnus expansion and some of its applications. *Physics Reports*, 470(5):151 – 238, 2009.
- [20] T. Choi, S. Debnath, T. A. Manning, C. Figgatt, Z.-X. Gong, L.-M. Duan, and C. Monroe. Optimal quantum control of multimode couplings between trapped ion qubits for scalable entanglement. *Phys. Rev. Lett.*, 112:190502, May 2014.
- [21] Vera M. Schäfer. *Fast gates and mixed-species entanglement with trapped ions*. PhD thesis, University of Oxford, 2018.
- [22] Shi Liang Zhu, C. Monroe, and L. M. Duan. Arbitrary-speed quantum gates within large ion crystals through minimum control of laser beams. *Europhys. Lett.*, 73(4):485–491, 2006.
- [23] Caroline Margaret Figgatt. *Building and Programming a Universal Ion Trap Quantum Computer*. PhD thesis, University of Maryland, 2018.
- [24] C. Flühmann, V. Negnevitsky, M. Marinelli, and J. P. Home. Sequential modular position and momentum measurements of a trapped ion mechanical oscillator. *Phys. Rev. X*, 8:021001, Apr 2018.
- [25] Shengtao Wang. *Applications of Atomic Systems in Quantum Simulation, Quantum Computation and Topological Phases of Matter*. PhD thesis, University of Michigan, 2017.
- [26] G. Kirchmair, J. Benhelm, F. Zähringer, R. Gerritsma, C. F. Roos, and R. Blatt. Deterministic entanglement of ions in thermal states of motion. *New J. Phys.*, 11, 2009.

- [27] Christian F. Roos. Ion trap quantum gates with amplitude-modulated laser beams. *New J. Phys.*, 10, 2008.
- [28] Pak Hong Leung, Kevin A. Landsman, Caroline Figgatt, Norbert M. Linke, Christopher Monroe, and Kenneth R. Brown. Robust 2-qubit gates in a linear ion crystal using a frequency-modulated driving force. *Phys. Rev. Lett.*, 120:020501, Jan 2018.
- [29] Yao Lu, Shuaining Zhang, Kuan Zhang, Wentao Chen, Yangchao Shen, Jialiang Zhang, Jing-Ning Zhang, and Kihwan Kim. Scalable global entangling gates on arbitrary ion qubits. *arXiv e-prints*, page arXiv:1901.03508, Jan 2019.
- [30] Ping Zou and Zhi-Ming Zhang. Robust quantum gates between trapped ions using shaped pulses. *Physics Letters A*, 379(47):3045 – 3049, 2015.
- [31] C. Figgatt, A. Ostrander, N. M. Linke, K. A. Land sman, D. Zhu, D. Maslov, and C. Monroe. Parallel Entangling Operations on a Universal Ion Trap Quantum Computer. *arXiv e-prints*, page arXiv:1810.11948, Oct 2018.
- [32] Florian Michael Leupold. *Bang-bang Control of a Trapped-Ion Oscillator*. PhD thesis, ETH Zürich, 2015.
- [33] RP Photonics Encyclopedia. *Acousto-optic Modulators*. available online at https://www.rp-photonics.com/acousto_optic_modulators.html (last accessed 8 January 2019).
- [34] 780 nm Select Cutoff Single-Mode Fiber. available online at https://www.nufern.com/pam/optical_fibers/883/780-HP/ (last accessed 8 January 2019).
- [35] Gooch & Housego. 780nm fibre-coupled acousto-optic modulator. available online at https://goochandhousego.com/wp-content/uploads/2016/11/GH_DS_FO_FiberQ_780nm_150MHz_Fiber_Coupled_Acousto_Optic_Modulator.pdf (last accessed 8 January 2019).
- [36] Vlad Negnevitsky. *Feedback-stabilised quantum states in a mixed-species ion system*. PhD thesis, ETH Zürich, 2018.
- [37] John Heebner, Rohit Grover, and Tarek Ibrahim. *Optical Microresonators. Theory, Fabrication, and Applications*. Springer-Verlag London Limited, 2008.
- [38] K. K. Mehta, A. M. Eltony, C. D. Bruzewicz, I. L. Chuang, R. J. Ram, J. M. Sage, and J. Chiaverini. Ion traps fabricated in a CMOS foundry. *Appl. Phys. Lett.*, (105):044103, 2014.
- [39] Bahaa E. A. Saleh and Malvin Carl Teich. *Fundamentals of Photonics*. John Wiley & Sons, 2nd edition, 2007.

- [40] Tom Schatteburg. *Simulation of high-purity circularly polarized light from a waveguide ring resonator with azimuthal grating*. Semester Thesis, ETH Zürich, 2018.
- [41] Brent E. Little, Juha-Pekka Laine, and Sai T. Chu. Surface-roughness-induced contradirectional coupling in ring and disk resonators. *Opt. Lett.*, 22(1):4–6, Jan 1997.
- [42] K. Wörhoff, R. G. Heideman, A. Leinse, and M. Hoekman. TriPleX: a versatile dielectric photonic platform. *Advanced Optical Technologies*, 4:189–207, April 2015.
- [43] Marco Mancini. *Numerical simulation of fast Mølmer-Sørensen gate driven by optical standing waves*. Semester Thesis, ETH Zürich, 2018.



Eidgenössische Technische Hochschule Zürich
Swiss Federal Institute of Technology Zurich

Eigenständigkeitserklärung

Die unterzeichnete Eigenständigkeitserklärung ist Bestandteil jeder während des Studiums verfassten Semester-, Bachelor- und Master-Arbeit oder anderen Abschlussarbeit (auch der jeweils elektronischen Version).

Die Dozentinnen und Dozenten können auch für andere bei ihnen verfasste schriftliche Arbeiten eine Eigenständigkeitserklärung verlangen.

Ich bestätige, die vorliegende Arbeit **selbständig** und in eigenen Worten verfasst zu haben. Davon ausgenommen sind sprachliche und inhaltliche Korrekturvorschläge durch die Betreuer und Betreuerinnen der Arbeit.

Titel der Arbeit (in Druckschrift):

Optical pulse shaping for trapped-ion quantum computing with integrated photonics

Verfasst von (in Druckschrift):

Bei Gruppenarbeiten sind die Namen aller Verfasserinnen und Verfasser erforderlich.

Name(n):

Miller

Vorname(n):

Stefanie

Ich bestätige mit meiner Unterschrift:

- Ich habe keine im Merkblatt „Zitier-Knigge“ beschriebene Form des Plagiats begangen.
- Ich habe alle Methoden, Daten und Arbeitsabläufe wahrheitsgetreu dokumentiert.
- Ich habe keine Daten manipuliert.
- Ich habe alle Personen erwähnt, welche die Arbeit wesentlich unterstützt haben.

Ich nehme zur Kenntnis, dass die Arbeit mit elektronischen Hilfsmitteln auf Plagiate überprüft werden kann.

Ort, Datum

Zürich, 02.05.2019

Unterschrift(en)

Bei Gruppenarbeiten sind die Namen aller Verfasserinnen und Verfasser erforderlich. Durch die Unterschriften bürgen sie gemeinsam für den gesamten Inhalt dieser schriftlichen Arbeit.